MOLECULAR SIMULATION STUDIES TOWARD ROBUST SUPERCAPACITORS: SCALABLE SCREENING AND MODELING OF COMPLEX SYSTEMS

By

Ray A. Matsumoto

Dissertation

Submitted to the Faculty of the

Graduate School of Vanderbilt University

in partial fulfillment of the requirements

for the degree of

DOCTOR OF PHILOSOPHY

in

CHEMICAL AND BIOMOLECULAR ENGINEERING

June 30, 2021

Nashville, TN

Approved:

Professor Peter T. Cummings

Professor Clare M^{c}Cabe

Professor G. Kane Jennings

Professor Kelsey B. Hatzell

To my friends and family, for their continued love and support

ACKNOWLEDGMENTS

I would first like to thank my advisor Peter Cummings for his mentorship, scientific discussion, and support of my academic and professional goals. Furthermore, I would like to thank him for the opportunities to meet with other scientists and present my research at various meetings and conferences. These experiences have been invaluable to my professional development.

I would also like to acknowledge the group members of Peter Cummings and Clare M^{c}Cabe. I am especially grateful to Matt Thompson, to whom I attribute much of my scientific development to. Additionally, I am thankful to Andrew Summers, Tim Moore, Christoph Klein, Yu Zhang, Justin Gilmer, Alex Yang, Co Quach, Alyssa Nelson, Chloe Frame, Duncan Stewart, Wei Zhao, and Xiaobo Lin for their support and scientific discussion over the years.

I would also like to acknowledge Ryan DeFever for his input and guidance on many aspects related to software design and molecular simulation.

I would also like to acknowledge the experimental collaborators with whom I had the pleasure of working with over the years. I was fortunate to work with an extensive network of scientists in which experiments and simulation could be simultaneously used to better understand the systems of interest. These researchers include those in the FIRST Center, Wahid Zaman, and Kelsey Hatzell.

Finally, I would like to thank those during my undergraduate studies whom introduced me to scientific research and motivated me to pursue graduate school. Junsaku Nitta and Jeongchun Ryu, who allowed me to get my first research experience at Tohoku University. Gary Lickfield and Steve Chester, who further motivated me to pursue graduate school.

TABLE OF CONTENTS

LIST OF TABLES

LIST OF FIGURES

LIST OF ABBREVIATIONS

$[BMIM^+][Tf_2N^-]$ 1-Butyl-3-methylimidazolium bis(trifluoromethanesulfonyl)imide

$[EMIM^+][Tf_2N^-]$ 1-Ethyl-3-methylimidazolium bis(trifluoromethylsulfonyl)imide

AA tetraalkylammonium

ACN acetonitrile

BASIS backscattering silicon spectrometer

C10 decyltrimethylammonium

C12 dodecyltrimethylammonium

C16 hexadecyltrimethylammonium

C4 butyltrimethylammonium

C4 butyltrimethylammonium

C6 hexyltrimethylammonium

C8 octyltrimethylammonium

CDC carbide-derived carbons

CI continuous integration

CL&P Canongia Lopes & Padua

CMD classical molecular dynamics

COM Center of mass

CV cyclic voltammetry

DCM dichloromethane

DFT Density functional theory

DFTB Density-functional tight-binding

EDLC Electric Double Layer Capacitors

EIA Energy Informtion Administration

EIS electrochemical impedance spectroscopy

FPMD First-principles molecular dynamics

GCMC Grand canonical Monte Carlo

GCPM Gaussian charge polarizable model

GEMC Gibbs Ensemble Monte Carlo

GMSO General Molecular Simulation Object

GUIs Graphical user interfaces

INS inelastic neutron scattering

ISIS Institute for Software Integrated Systems

IXS inelastic x-ray scattering

LJ Lennard-Jones

MC Monte Carlo

MD Molecular Dynamics

MeOH methanol

MoSDeF Molecular Simulation and Design Framework

MSD mean squared displacements

NCNR Center for Neutron Research

NIST National Institute of Standards and Technology

NQE nuclear quantum effects

OLC onion-like carbon

OPLS optimized potentials for liquid simulations

ORNL Oak Ridge National Laboratory

PC propylene carbonate

PDF Pair distribution function

PFG-NMR Pulsed Field Gradient Nuclear Magnetic Resonance

QM Quantum Mechanical

RTILs Room-temperature ionic liquids

SNS spallation neutron source

SSA specific surface area

THF tetrahydrofuran

TRUE transferable, extensible, usable by others, and extensible

vdW-DF Van der Waals density functional

VHF Van Hove Function

XRD X-ray diffraction

CHAPTER 1

Introduction

According to the United States Energy Information Administration (EIA), the world energy consumption is expected to increase by nearly 50%[1] by 2050. To meet growing energy demands, further development of alternative energy sources is required. Solar energy is particularly promising as the energy from sunlight striking the earth for one hour exceeds all human energy consumption from one year[2]. Due to the varying availability of sunlight throughout the day, efficient energy storage methods are a necessary component for viable solar energy[3]. One such method is through the use of electrochemical energy storage devices, such as batteries, Electric Double Layer Capacitors (EDLCs), and fuel cells. EDLCs, or supercapacitors, were first patented by Howard Becker of General Electric in 1957[4]. By 1992, significant improvements were made and Maxwell Technologies was producing supercapacitors for commercial use[5]. However, work remains to improve supercapacitor performance to a level necessary for widespread application. To achieve these improvements, a molecular-level understanding of the electrolyte and electrode behavior is required. This includes the structure, transport, and thermodynamics of electrolytes in the bulk phase, at interfaces with electrode materials, and under confinement.

The work presented here focuses on the use of molecular simulation, mainly classical molecular dynamics, to better understand supercapacitor-related systems at the molecular level. The molecular simulations have mainly been performed to provide a better understanding of results obtained by our experimental collaborators which are also presented here. In other cases, the simulations are conducted to predict behavior and trends that are later studied through experimental probes. Chapter 2 provides a background of capacitive energy storage devices as well as molecular simulation. In

Chapter 3, a scalable screening study of ionic liquid and organic solvent mixtures is reported. Chapter 4 presents a study of fluids through the Van Hove Function to better understand the microscopic dynamics of these systems. Chapter 5 explores the properties of electrolytes at interfaces, and under confinement of MXenes. Efforts to improve reproducibility in molecular simulation are described in Chapter 6. Lastly, the presented results are summarized in Chapter 7.

CHAPTER 2

Background

2.1 Capacitive Energy Storage

Electrochemical energy storage will play an important role in meeting the growing demands of energy[6] as efficient storage is required for alternative energy sources, including solar and wind[2,3]. Batteries have certainly achieved widespread use in consumer electronics due to their high energy densities[7], although they are not without limitations. These devices store energy through diffusion-controlled Faradaic reactions which result in longer charging times (low power density) and limit the lifetime of these devices to the order of a thousand cycles[8]. This is among the major reasons preventing the widespread adoption of electric vehicles. Further, batteries are currently cost-prohibitive in other applications, such as in the electricity sector[9].

The charge storage mechanisms of EDLCs, or supercapacitors, are fundamentally different, involving no Faradaic reactions. Rather, the process involves the adsorption of ions at interfaces under an applied potential[8]. Because this mechanism is absent of chemical reactions, supercapacitors often exhibit much longer cycle lifetimes and are free of reaction kinetic limitations, allowing for faster ion dynamics[8,12–14]. However, typical supercapacitors comprising of porous graphene display energy densities lower than those of batteries due to low specific capacitance and low operating voltage windows. The trade-off between energy and power density is presented in Fig. 2.1. In the context of electric vehicles, the use of a supercapacitor would allow for much shorter charging times but would have a much shorter range than any vehicle currently on the market[15]. Supercapacitors have thus been relegated to applications such as regenerative braking, memory backups in personal computers, solar arrays, and wind turbines[14].

For supercapacitors to reach more widespread use, substantial increases in energy density

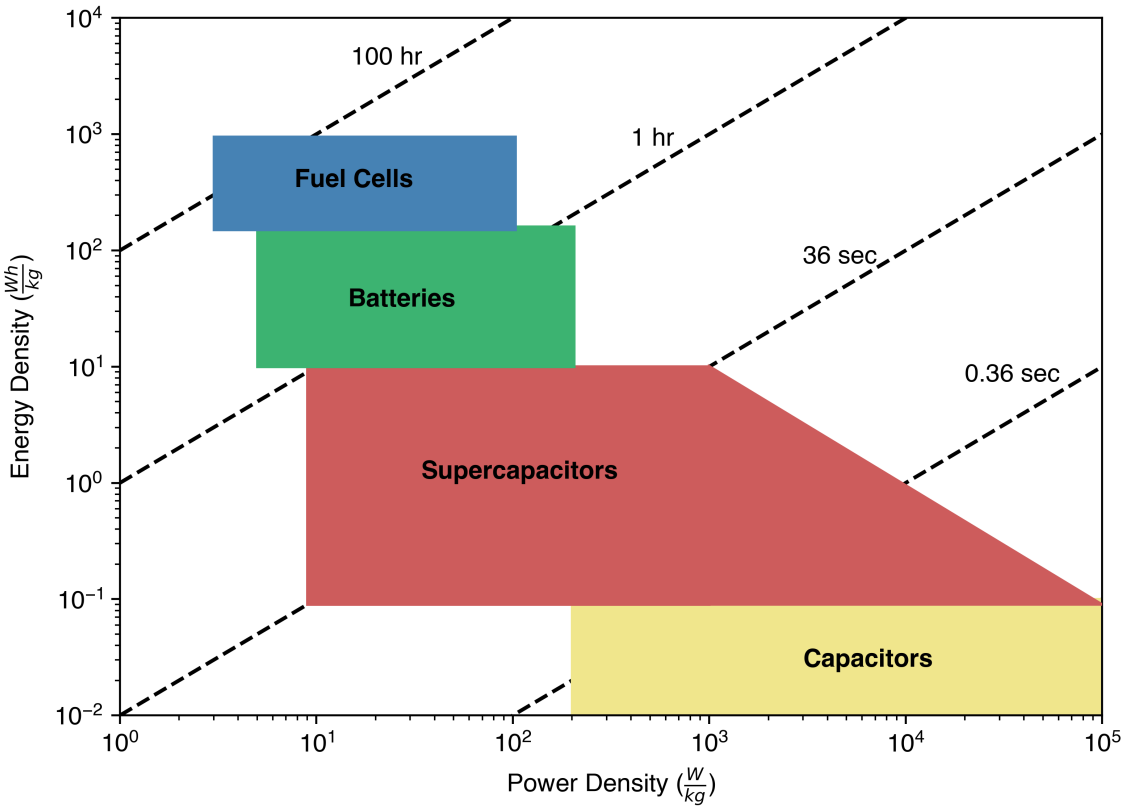

Figure 2.1: Ragone Plot displaying the trade-off between energy density and power density for common energy storage devices [10,11].

and/or power density must be achieved. Guidelines for improving these properties is given by the following equations:

$$E = \frac{1}{2}CV^2 \tag{2.1}$$

$$P = \frac{V^2}{4R} \tag{2.2}$$

where E is energy density, C is DC capacitance, V is the voltage, R is the resistance, and P is power density[16]. Further, the capacitance of an interface is defined by:

$$C = \frac{\sigma A}{4\pi t} \tag{2.3}$$

where σ is the dielectric constant, A is the effective surface area, and t is the thickness of the electrical double layer[15]. Both energy and power density can be improved with an increased operating voltage window. Energy density can be improved with increased capacitance (decreased thickness, increased surface area), while power density can be improved with lower resistance.

2.2 Solvents

Supercapacitor performance is greatly influenced by the choice of electrolyte. Guided by the equations above, an ideal electrolyte should exhibit a high operational voltage window (high energy density), low resistivity (high power density), high ionic conductivity, low toxicity, among other characteristics[17–19]. Electrolytes can be classified into three categories: aqueous, organic, and ionic liquid[18]. This thesis mainly focuses on ionic liquid electrolytes, although aqueous electrolytes are investigated as well. Aqueous electrolytes are mixtures of ions and water which display high ionic conductivities, low cost, and are relatively safe[6,20,21]. However, aqueous electrolytes display relatively low operational voltage windows (Up to 1.2 V), which limits the energy density of a device[19]. Popular organic electrolytes include acetonitrile and propylene carbonate as solvents[6,22].

These electrolytes typically display lower conductivities, higher cost, higher resistivity, and higher toxicity than aqueous electrolytes[6,23]. Nevertheless, organic electrolytes display operational voltage windows up to 2.7 V[19].

Aqueous and organic electrolytes are considered classical solutions in which ions are solvated in a molecular solvent[24]. In contrast, an ionic liquid is a salt in the liquid state at ambient conditions in the absence of a molecular solvent[24]. Ionic liquids that are liquid at room-temperature are aptly referred to as room-temperature ionic liquids (RTILs)[24]. Ionic liquids were first discovered in the early 1900s, although research interest did not become more widespread until the end of the century. By this time, ionic liquids started to become much more commercially available and the concept of ionic liquids as ”designer solvents” provided the possibility of engineering ideal fluids for specific applications[25].

Ionic liquids generally consist of bulky, asymmetrical ions which results in poor molecular packing and decreased melting points[24,26]. They exhibit strong electrostatic interactions, which results in high cohesive energy densities and low vapor pressures. Due to these unique properties, ionic liquids have shown promise in many applications, including catalysis[27], gas separation[28–30], and lubrication[31,32]. Perhaps the most promising application for ionic liquids is their use as electrolytes in electrical energy storage[19,24,33–36]. In comparison to aqueous and organic electrolytes, ionic liquids boast much higher operational voltage windows. Theoretical operational voltage windows up to 6 V[37] have been observed, while practical voltages exist between 3-3.5 V[38]. Considering the equation for energy density described above, the energy density of a device quadratically scales with the operating voltage window. As a result, the notable increase in operating voltage window for ionic liquids can result in greatly increased energy densities.

Several drawbacks exist for ionic liquids as electrolytes. Due to strong electrostatic interactions and high molecular weights, ionic liquids exhibit slower transport properties, including lower diffusion coefficients, higher shear viscosity, and lower ionic conductivity in comparison to other electrolytes[39–44]. Because conductivity is inversely related to

resistance, slower transport properties result in a drop in power density.

Ion pairing in ionic liquids is difficult to define due to their ionic makeup[45–47] and has been a topic of debate in the field[48,49]. At a macroscopic level, ion pairing can be evaluated through the concept of ionicity[50–53]:

$$I = \frac{\sigma_{imp}}{\sigma_{NMR}} \tag{2.4}$$

where σ_{imp} is the conductivity measured from experiments and σ_{NMR} is the conductivity estimated from NMR. σ_{NMR} is defined by:

$$\sigma_{NMR} = \frac{N_A e^2}{kT}(D^+ + D^-) \tag{2.5}$$

where N_A is Avogadro's Number, e is the electron charge, k is the Boltzmann constant, T is temperature, and D represents the diffusion coefficients of the ions. Watanabe *et al.*[50] found the ionicity of ionic liquids to be lower than one, indicating the measured conductivity is lower than the value estimated from the diffusion coefficients of the ions. This is attributed to correlated motions of the counterions, suggesting the presence of ion pairing negatively impacts the conductivity of ionic liquids.

An approach to mitigate the slow transport properties is to mix ionic liquids with organic solvents[54], which improves the transport properties while maintaining many of the desirable ionic liquid properties[55–57]. Solvation of ionic liquids may also reduce the ion correlations, positively impacting the ionic conductivity. The effect of solvation on ionic liquid transport properties and ion pairing is investigated both with molecular simulation and experimental methods in Chapter 3.

2.3 Electrode Materials

Supercapacitors store charge through the mechanism of ion adsorption at the surface of a charged electrode. The equation above defines the relationship in which capacitance

scales with increased surface area due to the increased adsorption sites for ions. For this reason, porous materials have traditionally been studied in supercapacitor research. Specifically, carbon-based materials are ideal for capacitive energy storage due to a high specific surface area (SSA), and a wide operational voltage window in a variety of electrolytes[6,58]. Versatility is another key benefit of carbon materials as various structures can be synthesized, and properties such as porosity can be tuned. Examples of some carbon structures include onion-like carbon (OLC), carbon nanotubes, carbide-derived carbons (CDC), and graphene[6,59]. OLCs and carbon nanotubes have SSAs on the lower end of carbon materials (up to 500-600 $\mathrm{m\,g^{-1}}$ and 1000 $\mathrm{m\,g^{-1}}$ respectively), although these areas are highly accessible to ion adsorption. Despite low capacitances, these materials exhibit high electrical conductivities and are suitable for high power density applications[6]. CDCs are synthesized through a reaction that selectively etches metals from carbides. This process allows for highly tunable pore sizes by changing synthesis conditions. These structures result in high capacitance with SSA between 1000-3000 $\mathrm{m\,g^{-1}}$. Thompson *et al.* developed an atomistic model of CDCs for use in molecular simulation[60]. Graphene has been widely studied[61–63] due to a highly accessible SSA up to 2670 $\mathrm{m\,g^{-1}}$ as well as high conductivity[6].

Carbon materials are often modeled as slit pores in contact with an electrolyte in molecular simulation[64] Chapter 6 briefly discusses the use of a Python package to programmatically construct carbon slit pores for molecular simulation.

MXenes are a family of two-dimensional metal carbide/nitride materials which were first synthesized by Naguib *et al.* in 2011[65]. Since then, scientific research on MXenes has greatly increased for numerous applications including water purification[66,67], catalysis[68,69], and energy storage[70–73]. The MXene name is derived from the chemical composition $\mathrm{M_{n+1}AX_n}$, a so-called MAX phase which they are derived from: M stands for an early transition metal such as Ti or Mo, A is an element typically from group 13 or group 14 such as Al or Si , and X is carbon, nitrogen or a combination of the two[74].

Through selective etching, due to weaker M-A bonds, the A phase is lost and the resulting product is a crystalline 2D metal carbide/nitride composed of alternating layers of metal and carbon/nitrogen[75]. MXenes have exhibited high capacitances due to pseudocapacitance from fast redox-reactions at the surface[76,77]. Simultaneously, MXenes have been shown to exhibit high power densities because of high conductivity and the ability to intercalate various ions.[72,74]. Chapter 5 focuses on molecular simulation work related to MXenes.

2.4 Molecular Simulation

Molecular Dynamics (MD) is a computational method in which atoms are handled through the classical equations of motion. The total energy of a system is dependent only on the position and momenta of the particles. Interactions between particles are handled through a set of potential functions, referred to as force fields[78]. Force fields vary in complexity and modeling interactions including, but not limited to: bonded, angle, dihedral, Van der Waals, and Coulombic interactions. More complex force fields may take into account bond order, many-body interactions, and polarizability. This thesis primarily focuses on classical molecular dynamics (CMD) which calculates the total energy of a system through pairwise interactions using the following equation:

$$\begin{aligned}\phi_{tot} = \sum_{bonds} k_b(r-r_0)^2 + \sum_{angles} k_\theta(\theta-\theta_0)^2 + \sum_{dihedrals} k_\chi[1+cos(n\chi-\delta)] \\ + \sum_{impropers} k_\omega(\omega-\omega_0)^2 + \sum_{i=1}^{N-1}\sum_{j>i}^{N}[4\varepsilon_{ij}\frac{\sigma_{ij}{}^{12}}{r_{ij}} - \frac{\sigma_{ij}{}^{6}}{r_{ij}}] + \frac{q_i q_j}{r_{ij}}\end{aligned} \tag{2.6}$$

The k terms refer to force constants, n and δ in the dihedral term refers to periodicity and phase shift, σ and ε is the distance at particle-particle interaction energy is 0 and depth of the potential well, q is the partial charge of a particle, and r_{ij} is the distance between particles. The terms in order correspond to the energies of bond rotations, angle bending, rotations around four adjacent bonded particles, improper dihedral rotations, Van der

Waals interactions, and Coulombic interactions. Bond and angle energies are widely modeled as harmonic springs, while the functional form for dihedral terms varies by force field. Van der Waals interactions are largely modeled through Lennard-Jones (LJ), although other potentials such as Buckingham[79,80] and Mie[81] are also utilized in MD. To accurately model a system through MD, a force field should reproduce a desired property/properties measured from experiments or *Ab initio* calculations. Common properties to fit include densities, energies, and torsional profiles. SPC/E[82] and TIP3P[83] are simple, 3-site water models in which bonds and angles are held rigid. Thus bonded interactions are absent in these models. Further, the Van der Waals interactions for the hydrogen are generally excluded, leaving only σ and ε parameters for the oxygen, and the partial charges to be tuned. More complex classical force fields include optimized potentials for liquid simulations (OPLS)[84] developed by Jorgensen for organic molecules. This force field includes bonded interaction terms (bonds, angles, dihedrals) in addition to the non-bonded terms which were fitted to a combination of densities, heats of vaporization, and gas-phase torsional profiles. Extensions of OPLS for ionic liquid molecules are discussed and utilized in Chapters 3 and 5. Results of various water models are discussed in Chapter 4.

Because the energetics are computed through the equations of motion, MD is particularly useful for calculating transport properties such as self-diffusion coefficients, viscosities, and conductivities[42,85–87]. However, MD simulations can be slow to equilibrate and can be susceptible to being trapped in local energy minima. Special care must be taken to ensure that the system has sufficiently reached equilibrium. In these cases, Monte Carlo (MC) methods may be more suitable. One published study showed that MC simulation was 2-2.5 times faster folding polypeptides compared to MD simulation[88].

MC simulation methods are less of a focus in this thesis, although some work from collaborators is discussed in Chapter 6. MC simulations utilize the same force fields as MD to define interactions between particles in a system. Rather than generating new

configurations through the equations of motion, this is done in MC by randomly selecting a particle to perturb[89]. A Markov chain of states is generated to sample configurations from the probability distribution associated with the statistical mechanical ensemble. To generate a new configuration in the Markov chain, a trial configuration is first attempting a random perturbation to the current configuration. Then, the trial configuration is either accepted or rejected by a defined acceptance criterion, typically Metropolis. In the Metropolis sampling algorithm, acceptance depends on the probabilities of a trial configuration and the energy difference between the current and trial configurations[90]. Because MC is not bound by the classical equations of motion, this method is not suitable for computing transport properties. However, MC is generally more efficient at reaching system equilibration[78,89] and thus not as susceptible to getting stuck in local energy minima like MD methods. MC is also the more suitable method for simulating a system without a fixed number of particles. Grand canonical Monte Carlo (GCMC) simulations[91] are run at a fixed chemical potential, temperature, and volume in which insertion/deletion moves are attempted in addition to the standard translation and rotation moves. This method is particularly useful for equilibrating a system to the correct density and calculating adsorption/desorption isotherms[92,93].

2.5 Software

Reproducibility remains a challenge in scientific research. From a 2016 survey consisting of 1,576 researchers, over 70% of those have tried and failed to reproduce another scientist's experiments[94]. Despite the lack of external variables present in experiments, reproducibility remains a challenge in molecular simulation. Molecular simulations are rather sensitive to specific details, including but not limited to: interaction parameters (also referred to as a force field), integrators, combining rules, and initial structures. For systems with complex chemistries, construction routines are often intricate and many force field parameters are required. These steps often contain a combination of tools such

as graphical user interfaces (GUIs), stand-alone scripts, and *ad hoc* edits, further adding to the complexity of system initialization. Although documentation is often provided in the supporting information, and in some cases on a public domain such as GitHub, important details are unavoidably excluded.

Another barrier to reproducibility in molecular simulation is the difficulty of producing identical results of a chemical system from different simulation engines. In theory, simulating the exact chemical system in two different simulation engines should produce the same results. In reality, this is a non-trivial task as each software package often employs unique input file formats, unit sets, and functional forms. In some instances, the simulation software is developed in-house or commercially, and thus the source code, underlying algorithms, and other details cannot be easily viewed. To provide an example, a disagreement related to phase transitions in supercooled water stemmed from differences in simulation software. The disagreement in results was only recently settled when the two sets of codes were shared with others to determine the inconsistency[95]. By opening code to the public, users can gain a greater understanding of algorithm implementation and the chance of catching bugs is increased. As a result, open-source software has a clear advantage in improving reproducibility in molecular simulation.

The Molecular Simulation and Design Framework (MoSDeF) is a Python-based open-source software library that aims to address the issues of reproducibility in molecular simulation. The library comprises of `mBuild`[96,97] for programmatic system construction, and `foyer`[98–100] for encoding and application of force field parameters. Recent integration with the `signac framework`[101,102], developed by the Glotzer group at the University of Michigan, provides data and workflow management especially necessary for large-scale computational screening. MoSDeF has been utilized in various published studies[103,104], including the work discussed in Chapter 3. In Chapter 6, the use and development of MoSDeF to develop transferable, extensible, usable by others, and extensible (TRUE) workflows for molecular simulation of systems relevant to capacitive

energy storage is discussed.

CHAPTER 3

Structure, Dynamics, and Thermodynamics of Ionic Liquid and Organic Solvent Mixtures

3.1 Introduction

Ionic liquids have shown promise as electrolytes for electrical energy storage due to their wide operational voltage windows.[19,24,33–36]. However, ionic liquids display slow transport properties (high viscosities, low conductivities, slow diffusion) due to their strong electrostatic interactions and high molecular weights which can negatively impact device performance[39–44]. One approach to improve ionic liquid dynamics is to solvate them in organic solvents. Prior research has shown that solvation of ionic liquids improves dynamics while maintaining a relatively high voltage window[55,57,105–107].

1 2 3 4 5

Inspired by work done by Osti *et al.*[54], this chapter focuses on a computational screening study of the ionic liquid, 1-Butyl-3-methylimidazolium bis(trifluoromethanesulfonyl)imide ($[BMIM^+][Tf_2N^-]$), in organic solvents at various concentrations. The dynamics, structure, and thermodynamics of the ions in these solutions are investigated in great detail through the use of MD simulations.

3.2 Background

The main disadvantage of using ionic liquids in energy-storage devices is their slow transport properties[24,52,53,112–114]. Ionic liquid dynamics can be improved through the

[1]Portions of this work reprinted with permission from the works below:

[2]M. W. Thompson, R. Matsumoto, R. L. Sacci, N. C. Sanders, and P. T. Cummings, Journal of Physical Chemistry B **123**, 1340 (2019), ISSN 15205207, Copyright 2019 American Chemical Society.

[3]R. Matsumoto, M. W. Thompson, and P. T. Cummings, Journal of Physical Chemistry B **123**, 9944 (2019), ISSN 15205207, Copyright 2019 American Chemical Society.

[4]N. C. Osti, R. A. Matsumoto, M. W. Thompson, P. T. Cummings, M. Tyagi, and E. Mamontov, J. Phys. Chem. C **123**, 19354 (2019), ISSN 1932-7447, Copyright 2019 American Chemical Society.

[5]J. Cui, T. Kobayashi, R. L. Sacci, R. A. Matsumoto, P. T. Cummings, and M. Pruski, The Journal of Physical Chemistry B **124**, 9931 (2020), Copyright 2020 American Chemical Society.

solvation in organic solvents. Pech *et al.* synthesized supercapacitor devices based on OLC and an ionic liquid solvated in propylene carbonate (PC). These devices showed significant increases in capacitance, energies per volume, and discharge rates over conventional supercapacitors. With solvation, some concern exists over decreased operational voltage windows. Numerous publications demonstrated that voltage windows remain relatively wide upon solvation of ionic liquids in solvents[55,57,106,107].

Previously, Osti *et al.*[54] investigated the effect of solvation on ionic liquid dynamics through MD simulations and QENS experiments. Specifically, the ion dynamics of $[BMIM^+][Tf_2N^-]$ in four different organic solvents were studied. Both simulation and experiment showed a positive correlation between ion diffusion and solvent dipole moment. Further, free energy calculations suggested solvents with higher dipole moments better screen ion-ion interactions, leading to better dynamics. Although an initial trend was established between ion dynamics and solvent properties, the parameter space of this study was limited to four solvents.

The self-interactions in ionic liquids are the sum of many complex interactions ranging from strong electrostatic, dispersive, and hydrogen-bonding interactions to more subtle, complex interactions such as polar and $\pi - \pi$ stacking effects. While decades of research employing rigorous and diverse experimental and simulation techniques have increased our understanding of these effects for particular ionic liquids, the picture gets increasingly complicated when also considering solvation effects. As a result, the parameter space to study ionic liquid and solvent mixtures should be increased to better understand the effects of solvation.

In this chapter, a screening study of a single ionic liquid, $[BMIM^+][Tf_2N^-]$, solvated in 23 various organic solvents at 18 different concentrations is discussed. This work has been published as four peer-reviewed journal articles[108–111].

3.3 Methods

3.3.1 Scope of Study

The original study of Osti *et al.* looked at [$BMIM^+$][Tf_2N^-] solvated in four organic solvents: acetonitrile (ACN), dichloromethane (DCM), methanol (MeOH), and tetrahydrofuran (THF). Solutions with ionic liquid concentrations of 0.25, 0.50, 0.75, and 1.0 mass fraction were considered.

For the computational screening study, 23 different organic solvents at 18 ionic liquid concentrations were studied. The solvents were grouped into five different classes and represent a range of structures and physiochemical properties. The list of organic solvents studied is shown in Table 3.1.

Table 3.1: Solvents used in this study.

Nitriles	Alcohols	Halocarbons	Carbonyls	Glymes
Acetonitrile	Methanol	Dichloromethane	Ethylene carbonate	Tetrahydrofuran
Butyronitrile	Ethanol	1,2-dichloroethane	Propylene carbonate	Glyme
Adiponitrile	Butanol	Chlorobenzene	Acetone	Diglyme
Benzonitrile	Octanol		Cyclohexanone	1,4-Dioxane
			Dimethylsulfoxide	
			NN-dimethylformamide	
			Dimethylacetamide	

3.3.2 Simulation Methods

3.3.2.1 Force Fields

In this chapter, [$BMIM^+$][Tf_2N^-] interactions are defined by the Canongia Lopes & Padua (CL&P) force field[115–118]. These force field parameters were derived from the OPLS-AA force field by Jorgensen, in which additional *Ab initio* calculations were performed to determine force constants, partial charges, torsion energy profiles, etc. The resulting parameters were validated through matching experimental liquid densities. By basing the ionic liquid parameters on the OPLS framework, the two sets of force field parameters share the same functional forms, scaling factors, and mixing rules. Therefore,

the CL&P and OPLS-AA parameters can be combined in a single simulation in which we can expect reasonable agreement with experiment. Here we take advantage of the common design choices of CL&P and OPLS-AA. The organic solvent interactions are described through the OPLS-AA force field and the ionic liquid interactions are described through the CL&P force field; the pairwise interactions between the organic solvents and ionic liquids are handled through Lorentz-Berthelot mixing rules.

3.3.2.2 Computational Screening with MoSDeF

The work in this chapter employs MoSDeF designed to automate the screening of soft matter systems. The workflow is comprised of four primary steps, detailed below, which include components of the MoSDeF software suite and extensions of it. First, systems are initialized with `mBuild`[96,97], which places ionic liquid and solvent molecules in a simulation box at random positions without overlapping. This particular `mBuild` function makes use of `PACKMOL`[119]. Force fields, including all intermolecular and intramolecular interactions, are then applied with `foyer`[98–100]. With all necessary inputs generated, all simulations are run and managed with the `signac` framework[101,102]. Lastly, analyses are done with various open-source tools, heavily relying on `MDTraj`[120] and packages in the SciPy ecosystem.

3.3.2.3 Classical Molecular Dynamics

All simulations were performed with GROMACS 5.1.4[121–125]. After systems are initialized with `mBuild` and atom-typed with `foyer`, energy minimization simulations were conducted to avoid energetic clashes arising from unfavorable initial configurations. This proceeded using 2000 steps of the steepest descent algorithm. The remaining simulations were all molecular dynamics simulations, in which, unless otherwise noted, similar parameters were used throughout. Electrostatics were treated with the Particle Mesh Ewald (PME) method[126], employing a real-space cutoff of 1.1 nm and in the inverse space a minimum grid spacing of 0.16 nm. Non-bonded van der Waals interactions were

also truncated at 1.1 nm. The Bussi thermostat[127] and, in the case of *NPT* simulations, Parrinello-Rahman barostat was used to keep systems at a reference state of 1 bar and 300 K. A timestep of 1 fs was used and all bonds were constrained using the LINCS[128] algorithm. First, to further relax systems out of unfavorable initial configurations, a 100 ps *NVT* simulation was performed. Then, to drive systems toward equilibrium liquid densities and not explode into a gaseous state, a 1 ns *NPT* simulation was performed at a reference pressure of 10 bar and followed up by a similar simulation with a reference pressure of 1 bar. Then, systems were further equilibrated in the *NVT* ensemble for 10 ns. Finally, systems were sampled for 30 ns in the *NPT* ensemble, writing configurations every 1.5 ps. In these sampling runs, the timestep was increased to 1.5 fs and long-range dispersion corrections were applied for energy and pressure.

3.3.2.4 Ionic Liquid Correlations

To evaluate the pairing and caging of ions in these systems, we wrote a Python package, `pairing`[129], and published it on GitHub under the MIT open-source license. It implements the cluster statistics algorithm developed by Sevick *et al.*[130]. This algorithm involves the calculation of a "direct correlation matrix", which determines which molecules are directly connected. Direct connection or pairing of ions was determined through the use of a distance criterion of 0.8 nm, roughly the center-to-center distance of the first valley in a typical RDF between $BMIM^+$ and Tf_2N^-. The $[BMIM^+][Tf_2N^-]$ radial distribution functions (RDFs) are shown in the Appendix. The direct connection of the ions is stored as a NxN matrix, where N is the number of ions in the system. If two ions are directly connected, the value of the corresponding index in the matrix is 1. Otherwise, the value of the index is zero. The process of calculating the direct matrices for all systems was implemented with Python's built-in `multiprocessing` module. Use of this module allowed for individual processors of our in-house computer cluster to calculate the direct matrices at various time points of a system trajectory in a parallelized

manner. Once the direct matrix was computed for each frame of a trajectory, the ratio of paired ions to the total number of ions was plotted against time. This decaying function was then fitted with a stretched exponential function to obtain the value, τ_{pair}, a measure of how long the ions stay paired in solution in units of nanoseconds.

In addition to pairing, the direct correlation matrix could also be utilized to quantify "ion caging" in each system. Ion cages are considered to be broken when a counterion leaves or enters an existing cage, and thus the direct connectivity of ions at time t was compared to the direct connectivity at time zero. To calculate the cages in each system, we compare the rows of the direct connectivity matrix at time t from the rows at time zero, as the rows indicate the pairs for an individual ion. If a row at time t differs from that at time zero, then the cage is considered to be broken. As with ion pairing, the ratio of caged ions to the total number of ions was plotted versus time and was fitted with a stretched exponential function to obtain τ_{cage}, a measure of how long ions stay caged in solution in units of nanoseconds.

3.3.2.5 Computation of Ionic Conductivity

A simple estimate of the ionic conductivity of a solution can be attained from the Nernst-Einstein (NE) equation:

$$\sigma_{NE} = \frac{N}{Vk_BT}(q_+^2 D_+ + q_-^2 D_-) \tag{3.1}$$

where N is the number of ion pairs, k_B is Boltzmann's constant, T is absolute temperature, q_+, q_- are molecular charges of and D_+, D_- the diffusivities of the positive and negative ions, respectively. This is typically a computationally inexpensive and simple calculation that can be done in one step once diffusivity values are known. However, this formula implicitly treats ions as fully dissociated and, while reasonable for aqueous electrolytes involving metal ions and strong acids, is less valid for ionic liquids.

A more rigorous method for computing the ionic conductivity is the Einstein-Helfand

(EH) equation:

$$\sigma_{EH} = \frac{1}{6Vk_BT} \lim_{t\to\infty} \frac{d}{dt} \langle [\vec{M}_J(t) - \vec{M}_J(0)]^2 \rangle \tag{3.2}$$

where translational dipole moment is defined as:

$$\vec{M}_J(t) = \sum_i q_i r_i(t) \tag{3.3}$$

and r_i is the center of mass (COM) position of ion i and q_i is the charge of ion i. Furthermore, $\langle [\vec{M}_J(t) - \vec{M}_J(0)]^2 \rangle$ is equal to $\frac{\sum_i [\vec{M}_J(t) - \vec{M}_J(0)]^2}{N}$, where N is the number of frames in the trajectory. Unlike the NE equation, the EH equation considers the effects of correlated ion motion on conductivity.[39,42,131]. It is also useful to compare conductivities measured by each equation. Others[50–53,114] have defined a ratio α as

$$\alpha = \frac{\sigma_{EH}}{\sigma_{NE}} \tag{3.4}$$

which quantifies the effects of correlated ion motions on conductivity. α is qualitatively similar to the ionicity that is reported by experimentalists. The ideal case, not typically found for ionic liquids, of unity indicates a lack of any ion correlations. This value is frequently reported to be less than unity, in the range 0.5 to 0.8.[50–53,114], indicating that the effect of τ_{pair} is relevant but not overwhelming.

3.3.2.6 Potentials of Mean Force

The accelerated weight histogram (AWH) simulations were handled similarly to the equilibrium simulations described above, utilizing the MoSDeF suite of tools and `signac` framework. Using `mBuild`, solvent molecules were placed in a box with dimensions of 5.5 nm x 5.5 nm x 8.5 nm. A single [$BMIM^+$][Tf_2N^-] molecule was then placed in the box. The CL&P and OPLS-AA force fields were once again applied with `foyer` to parametrize each system. GROMACS 2018.5 was used instead of version 5.1.4 because this version contains AWH capabilities[132]. Once systems were initialized and

atom-typed with `mBuild` and `foyer`, steepest-descent energy minimization was performed to relax any unfavorable initial configurations for 2000 time steps. Afterwards, equilibration in the *NPT* ensemble was performed for 1 ns with a 1 fs timestep. The v-rescale thermostat was used to control the temperature at 300 K, and the Berendsen barostat was to control the pressure at 1 bar. Position restraints of 1000 $\mathrm{kJ\,mol^{-1}\,nm^{-2}}$ in x,y, and z coordinates were applied to a central nitrogen of the immidazolium ring in $\mathrm{BMIM^{+}}$ and to the central nitrogen in $\mathrm{Tf_2N^{-}}$ to ensure that the ionic liquids generally remain in the specified coordinates of the simulation box. The addition of external forces from position restraints can lead to instabilities in the simulations with the use of the Parrinello-Rahman barostat, the other barostat option available in GROMACS; hence, the Berendsen barostat is chosen. Once the system was sufficiently equilibrated, the AWH sampling run was performed for 50 or 100 ns with a 1 fs time step, the time being dependent on how long it took for the PMF curves to converge. Position restraints of 1000 $\mathrm{kJ\,mol^{-1}\,nm^{-2}}$ in x,y, and z coordinates were again placed on the central nitrogen of the $\mathrm{BMIM^{+}}$ imidazolium ring to keep the molecule in the specified coordinates. Positions restraints of 1000 $\mathrm{kJ\,mol^{-1}\,nm^{-2}}$ in x and y coordinates were placed on the central nitrogen in $[Tf_2N^{-}]$ to keep the molecule in the specified coordinates in the x and y direction while allowing movement in the z-direction. The v-rescale thermostat and Berendsen barostat were once again used to control the temperature and pressure at 300 K and 1 bar respectively. The pull code was used to allow for the $\mathrm{Tf_2N^{-}}$ molecule to be sampled along the z-axis, the reaction coordinate of these MD simulations. The force constant was chosen to be 100,000 $\mathrm{kJ\,mol^{-1}\,nm^{-2}}$. To generate the PMF curves, the built-in GROMACS functions were used to extract the AWH data, with PMF curve data written for each time frame. The curves were then shifted to go to 0 as distance r goes to infinity. To do so, the PMF was plotted as a function of $1/r$ to obtain the slope. The curve fit was then obtained by plotting the slope over distance r. For each system, the PMF curves for each time frame were initially plotted to visualize the time evolution and

determine that the PMF curve has converged. Once convergence has been confirmed, the PMF curves were plotted using Matplotlib's `pyplot` [133].

3.3.3 Experimental Methods

3.3.3.1 Conductivity Measurements

Conductivity measurements were performed by Nicolette Sanders and Robert Sacci of Oak Ridge National Laboratory (ORNL). Conductivity was measured on a two-port 1/4" Teflon Swagelok cell with the electrodes spaced 1.3 mm apart at 296.35 K. The electrodes were 1.6 mm diameter Au disks embedded in PEEK as supplied by CHI Instruments. The cell constant was calculated to be 6.56 cm^{-1} and the constant as determined using a KCl standard solution was 6.54 cm^{-1}. Conductivity was taken as the real part of the 10 kHz data point in the impedance measurements recorded on a SP-200 Biologic potentiostat.

3.3.3.2 Quasielastic Neutron Scattering

QENS measurements were performed by Naresh Osti and Eugene Mamontov of ORNL. Experiments were specifically performed at National Institute of Standards and Technology (NIST), Center for Neutron Research (NCNR) and backscattering silicon spectrometer (BASIS) [134] at ORNL, spallation neutron source (SNS). At a high-level, neutron scattering involves the shooting of neutron beams at a sample. The neutron beams interact with the nuclei of the sample, and the energy transfers can be calculated from the differences of incident and final wave vectors [135]. The quasielastic scattering region is when the energy transfer is near zero, and can be utilized to measure the self-diffusion coefficients of samples. Due to the difference in neutron scattering cross-sections, deuterium can be used to focus on the dynamics of particular atoms in a sample.

3.3.3.3 Nuclear Magnetic Resonance

Pulsed Field Gradient Nuclear Magnetic Resonance (PFG-NMR) measurements were performed by Cui *et al.* at the Ames Laboratory. Briefly, PFG-NMR is performed by first

applying a gradient pulse with a specified intensity and duration. During this time, molecules of the sample are allowed to diffuse. Then, a second gradient pulse of the same intensity and duration with an opposite ”effective sign” allowing the spins to dephase. The diffusion coefficient can then be determined by fitting an exponential equation to the signal as a function of the gradient[136]. Additional details of methods are presented in Ref. 111.

3.4 Results of Computational Screening

The initial study of Osti *et al.* provided valuable insight into the properties ionic liquids when mixed with organic solvents. Both MD and QENS results showed agreement in which solvent polarity influences the dynamics of ions in these solutions. However, the scope of this study was limited to four solvents and four ionic liquid concentrations. The study of these systems in an expanded chemical space should be conducted to determine whether the established property trends remain true.

The portion of chemical space encompassed by systems containing ionic liquids is vast and largely unexplored. The number of neat ionic liquids - those with one cation, one anion, and no other components - was estimated on the order of billions almost two decades ago[137] and estimates of as high as 10^{18} have been suggested[35]. Consideration of mixtures of ionic liquids with other ionic liquids or solvents grows this figure by many orders of magnitude[35]. Unsurprisingly, most existing literature, even review papers, covers an extremely small subset of this space. For example, most cations studied in the literature are based on 1-alkyl-3-methylimidazoliums. This scale necessitates computational approaches; even modest ventures into this space are not feasible to do with experiments alone. Synthesis at high purities can be difficult for novel ionic liquids, and only a small fraction of possible ionic liquids have been synthesized. Additionally, the amount of characterization necessary to understand their structure, dynamics, and thermodynamics via experiments is virtually intractable. Computational screening can provide preliminary searches through this space, providing predictions of molecular and

macroscopic physical properties that experiments can later examine. Efforts in this direction have already begun.[138–142]

The scope of this computational screening study was much larger than the previous study of Osti *et al.*[54], and to our knowledge, greater than anything in the existing literature. Here, the same variables of solvent chemistry and ionic liquid compositions are studied, but for a greatly expanded data set. We consider compositions in the range 0.1 to 0.95 mass fraction in increments of 0.05 for a total of 18 values compared to the four originally studied. A total of 23 solvents, which includes the original four, were studied. The parameter space explored here was infeasibly large to be studied using the QENS experiments previously used. Oppositely, MD simulations are relatively inexpensive by comparison, in which it is possible to accurately sample hundreds, and even thousands of independent[103] systems through screening. The goal is to evaluate previously established trends related to ionic liquid and organic solvent mixtures through MD screening. Through a more comprehensive analysis of these systems, new insights guided by screening can then be further investigated and validated by experimental methods.

To automate each step in the process of screening (initializing a system, running simulations, and performing analysis), MoSDeF and the `signac` framework[101,102] were used.

3.4.1 Ion Diffusivities as a Function of Ionic Liquid Concentration

Bulk diffusivities were computed from mean squared displacements (MSDs) using the classical Einstein relation, which for a isotropic fluid is

$$\langle (\mathbf{r}(t) - \mathbf{r}(0))^2 \rangle \rightarrow 6Dt \text{ as } t \rightarrow \infty \tag{3.5}$$

where $\mathbf{r}(t)$ is the position of the ion at time t, $\langle ... \rangle$ indicates ensemble average, and D is diffusivity. It is useful to evaluate the individual components of each system. Therefore, in addition to the mixture as a whole, we consider the solvent, each ion, and the overall ionic

liquid as selections. The cation dynamics were previously isolated from our molecular dynamics simulations because the QENS experiments exclusively track the cations (the Tf_2N^- anion has no hydrogens but the $BMIM^+$ cation has several). For the case of $[BMIM^+][Tf_2N^-]$, which was used in both that study and this one, the cation and anion exhibit nearly identical bulk diffusivities. Therefore, the cation, anion, and overall ion dynamics can be interpreted interchangeably with each other, though this relationship should not be regarded as a general feature of ionic liquids. Here we will consider the overall ion dynamics.

Two diffusivities were computed for each selection: one from an MSD of the entire 30 ns trajectory and another when slicing it into 20 sections, every 1.5 ns slice comprising a shorter MSD, and averaging the diffusivities from each slice. This was done to gather statistics on the sampling error for each diffusivity. The two methods produce similar results and are further discussed in the Appendix.

First, one of the two major conclusions from the work of Osti *et al.* is revisited, which is a monotonic increase in cation diffusivity as the composition of solvent is increased. This result is consistent with intuition given the slow dynamics of neat ionic liquids relative to the pure organic solvents, but the structural and energetic complexity of these interactions should cast doubt on how strongly such physiochemical relationships should hold. That being said, we observe, using our larger parameter set, the same trend as before, summarized in Fig. 3.1.

It is worth noting that this trend is monotonic over the entire composition range, and no plateaus or discontinuities are observed. Given the tendency for many ionic liquids to phase separate into nanostructural domains[143–145], this observation implies that the transition from dilute ions and/or ion pairs to neat ionic liquids is smooth and lacks any discontinuous transitions, i.e. there is no critical composition at which pairs move from dense ionic liquid phases to dissociated ion pairs.

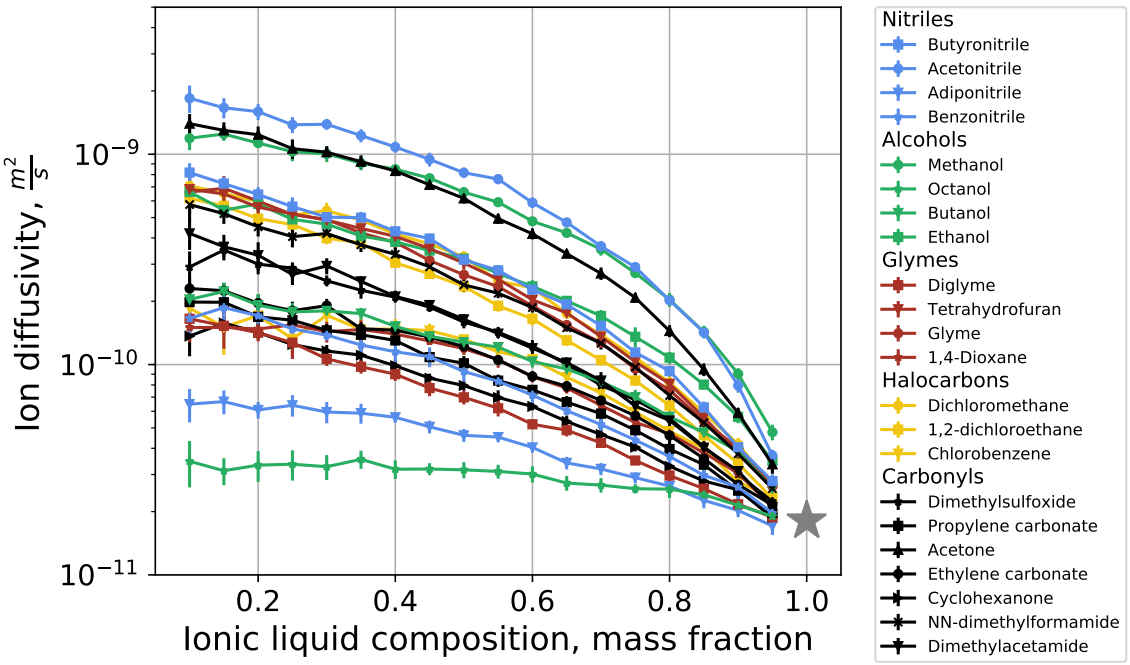

Figure 3.1: Ion diffusivity as a function of mixture composition. Error bars are included as vertical lines, though many are smaller than the width of the dots. Straight line segments are drawn connecting data points with common solvents. Grey star is shown to indicate the diffusivity of the neat ionic liquid.

3.4.2 Ion Diffusivities as a Function of Solvent Polarity

Next, the relationship between solvent polarity and ion diffusivity is revisited, which was the main focus of the prior study of Osti *et al.*[54]. Previously, acetonitrile, methanol, dichloromethane, and tetrahydrofuran were considered, in which it was found that solvents with greater solvent polarity produced mixtures that exhibited greater ion diffusivity. A more rigorous summary of our larger data, which considers 22 solvents, set is presented in Fig. 3.2.

While a general trend of increasing solvent polarity as a function of dipole moment is observed for subsets of the data, there exists no strong correlation when considering the entire data set. Mixtures with acetonitrile (D = 3.92) exhibited the largest diffusivity of all solvents, but mixtures with DMSO (D = 3.96) and propylene carbonate (D = 4.94) each exhibited slower diffusivity than acetonitrile despite their similar and higher molecular

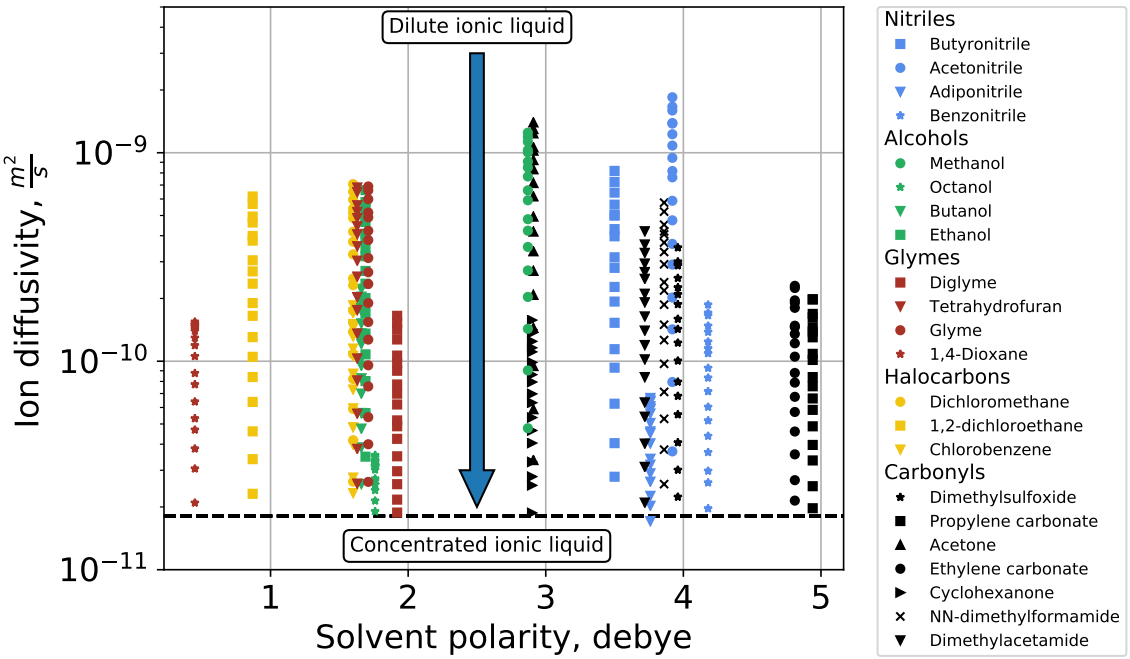

Figure 3.2: Ion diffusivity as a function of solvent polarity. Data points are arranged from top to bottom in order of increasing ionic liquid composition. The dashed line indicates the ion diffusivity of the neat ionic liquid.

dipole moments, respectively. Further, mixtures with methanol (D = 2.87 D) and acetone (D = 2.91 D) exhibited high diffusivity with lower polarity. These results imply that solvent polarity is not the only contribution to ion transport in ion liquid mixtures and to better inform the design of ionic liquid mixtures with enhanced transport properties, other solvent properties must be considered.

3.4.3 Ion Diffusivities as a Function of Solvent Molecular Weight

Note that solvent polarity is only one solvent property; others could be better predictors of the properties of the ionic liquid-solvent mixtures. We first chose to look at a simple solvent property, molecular weight, for the possibility it correlates better with ion diffusivity than polarity. As shown in Fig. 3.3, this relationship appears to be much stronger: solvents with greater molecular weight tend to produce mixtures with slower ion diffusivity.

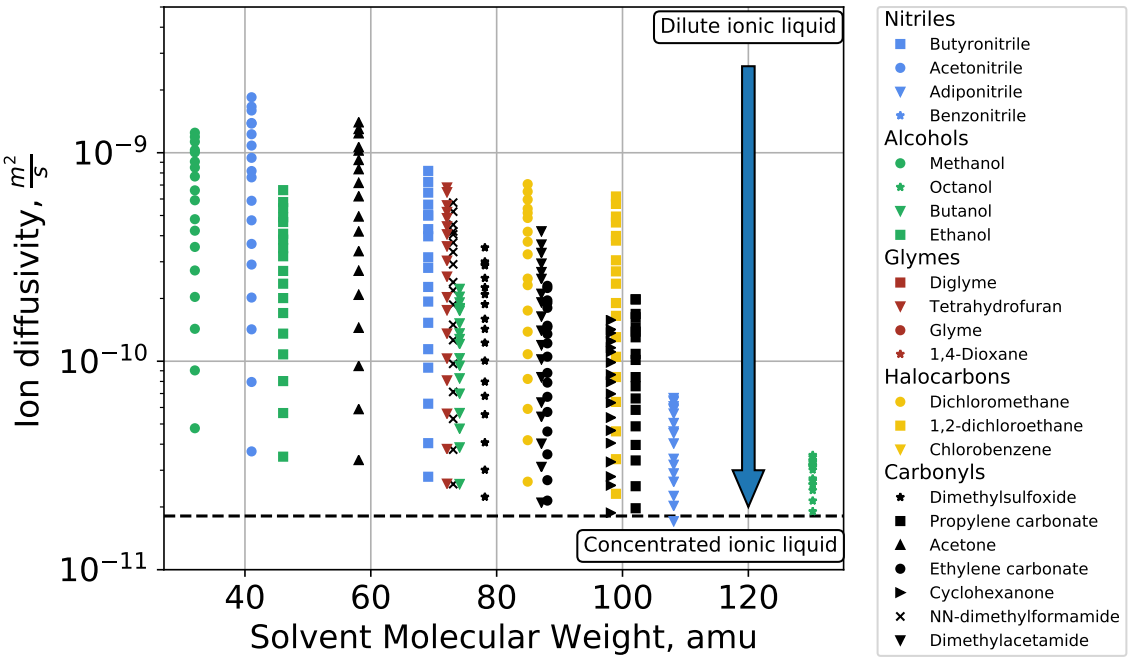

Figure 3.3: Ion diffusivity as a function of solvent molecular weight. Data points are arranged from top to bottom in order of increasing ionic liquid composition. The dashed line indicates the ion diffusivity of the neat ionic liquid.

3.4.4 Ion Diffusivities as a Function of Solvent Diffusivity

Next, we investigated the relationship between ion diffusivity and solvent diffusivity, computed from pure solvent simulations. In Fig. 3.4, we observe a more robust trend between ion diffusivity D_{ion} and pure solvent diffusivity $D_{solvent}$. Note that these solvent diffusivities are extracted from independent simulations of pure solvent, not the solvent component of the ionic liquid mixture simulations. This result is intuitively reasonable; sluggish ionic liquid molecules are more likely to exhibit increased molecular diffusivity in an environment of molecules with faster motion. The results are consistent with a Stokes-Einstein picture of ion mobility. According to Stokes-Einstein theory, D_{ion} should scale as the inverse of the solvent viscosity $\eta_{solvent}$ - i.e., $D_{ion} \sim \eta_{solvent}^{-1}$. However, liquid diffusivity generally scales inversely with viscosity, so in particular for these solvents, $D_{solvent} \sim \eta_{solvent}^{-1}$, thus leading to $D_{ion} \sim D_{solvent}$, as we observe from the simulation results.

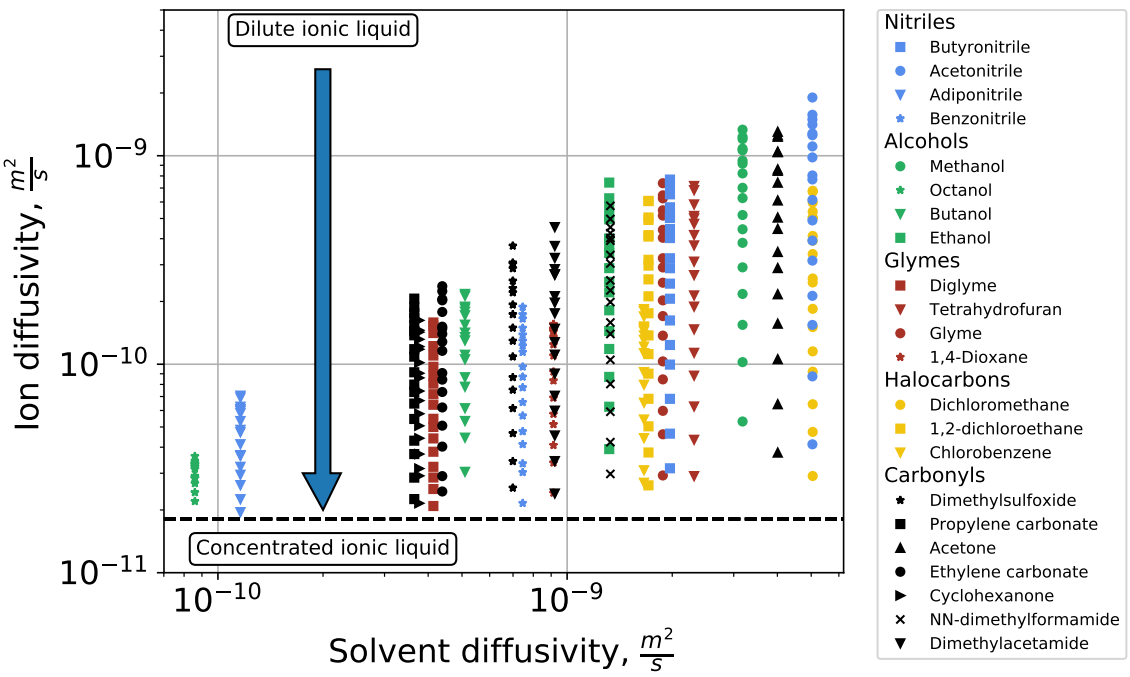

Figure 3.4: Ion diffusivity as a function of pure solvent diffusivity. Data points are arranged from top to bottom in order of increasing ionic liquid composition. The dashed line indicates the ion diffusivity of the neat ionic liquid.

3.4.5 Liquid Density

Next, the density of these ionic liquid-solvent mixtures as a function of composition. Fig. 3.5 shows that these densities change monotonically as a function of composition. They appear to roughly follow a simple mixing rule for all compositions outside of the dilute ionic liquid range. All solvents have lesser bulk densities than the ionic liquid and the densities of all mixtures fall between that of the pure solvent and ionic liquid components. After converting from liquid density to specific volume ($\hat{V} = 1/\rho$), we consider a simple mixing rule to define an ideal volume of mixing:

$$\hat{V}_{expected} = x_{IL}\hat{V}_{IL} + x_{solvent}\hat{V}_{solvent} \tag{3.6}$$

where $\hat{V}_i$ and x_i refer to the bulk liquid volume and composition of component i, respectively. x_i can be considered on a molar or mass basis. One can also define the excess

volume of mixing:

$$\hat{V}_{excess} = \hat{V}_{measured} - \hat{V}_{expected} \tag{3.7}$$

which characterizes deviations from ideal liquid behavior. Negative excess volumes can be interpreted as thermodynamically favorable interactions between species and positive values the opposite. These values are conventionally reported on a molar basis. We present excess molar volumes of mixing for our data set in Fig. 3.6. For most mixtures, the strongest deviation from ideal mixing is observed at intermediate compositions of approximately 0.1 - 0.3 mol fraction. Numerical values are on the order of $1.000\,\mathrm{cm^3\,mol^{-1}}$ and similar to reported values of mixtures of ionic liquids in molecular solvents.[146–149] All mixtures exhibit a positive excess density of mixing (equivalent to a negative excess volume of mixing) implying that their mixing is thermodynamically favored.

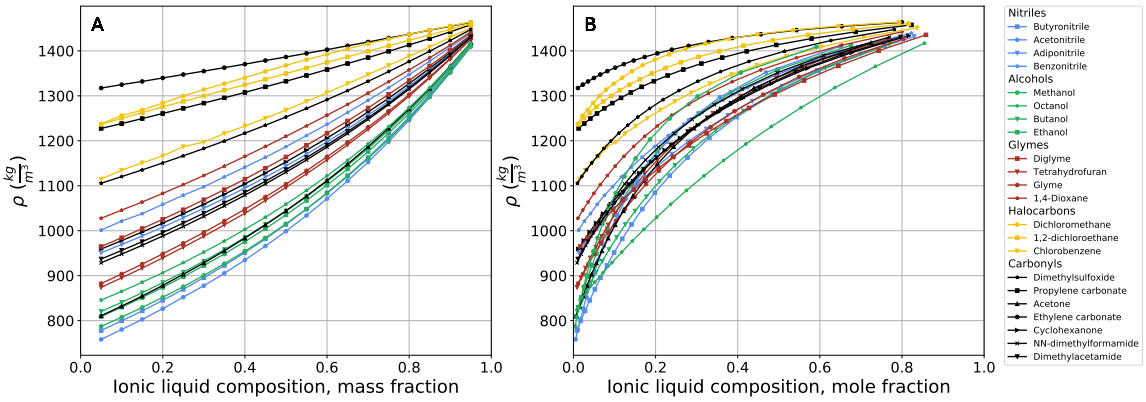

Figure 3.5: Density, ρ, as a function of [BMIM$^+$][Tf$_2$N$^-$] a) mass fraction and b) mole fraction

3.4.6 Radial Distribution Functions

Next we consider the local structure as defined by center of mass RDFs, focusing on pairs of cations and anions (i.e., $g_{+-}(r)$). In lieu of presenting hundreds of such curves, we present the location and magnitude of the first peak of $g_{+-}(r)$, r_{peak1} and $g_{max} = g_{+-}(r_{peak1})$, respectively in Fig. 3.7. These correspond to the common cation-ion

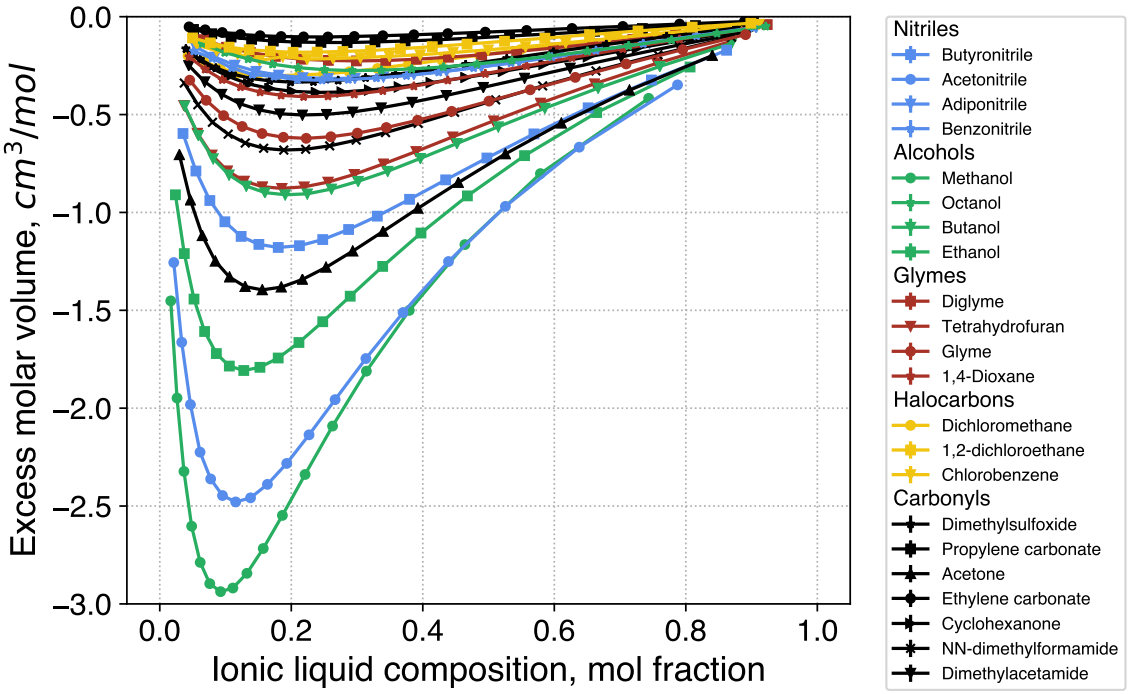

Figure 3.6: Excess molar volume, $\hat{V}_{excess}$, as a function of [BMIM$^+$][Tf$_2$N$^-$] mole fraction. Excess volume is measured as the difference between the molar volume of any given mixtures and a predicted value based on the composition and molar volumes of the pure components.

pairing structure characteristically observed in ionic liquids. The distances in r where this is observed, r_{peak1}, are largely insensitive to the properties of the solvent and appear to mostly be a function of ion properties, which were held constant in this study. In contrast, we observe that the heights of these peaks, g_{max}, depend strongly on the properties of the solvent and the composition of the mixture. Most notably, these values spike in the limit of low ionic liquid composition. While the numerical values are somewhat inflated by the nature of normalizing RDFs to dilute components, they indicate strong structuring of ionic liquid molecules. There is also considerable variance in this behavior among different solvents. Mixtures in carbonyl-containing compounds (i.e. propylene carbonate, ethylene carbonates, and dimethyl sulfoxide) display nearly identical g_{max} values overall composition ranges and do not exhibit the aforementioned spike at low concentrations. Mixtures in halocarbons and glymes together make up the most structured systems, and

mixtures in nitriles, alcohols, and other glymes have this spike but of lesser magnitude. This demonstrates that different chemical families of solvents give rise to substantially different ion structures in these mixtures. In particular, halocarbons and glymes drive ions to pair strongly whereas other solvents promote populations of free ions not bound to a neighboring counter-ion. This is an indicator of the capacity of each solvent to screen charges: halocarbons are ineffective while some carbonates robustly screen ion-ion interactions.

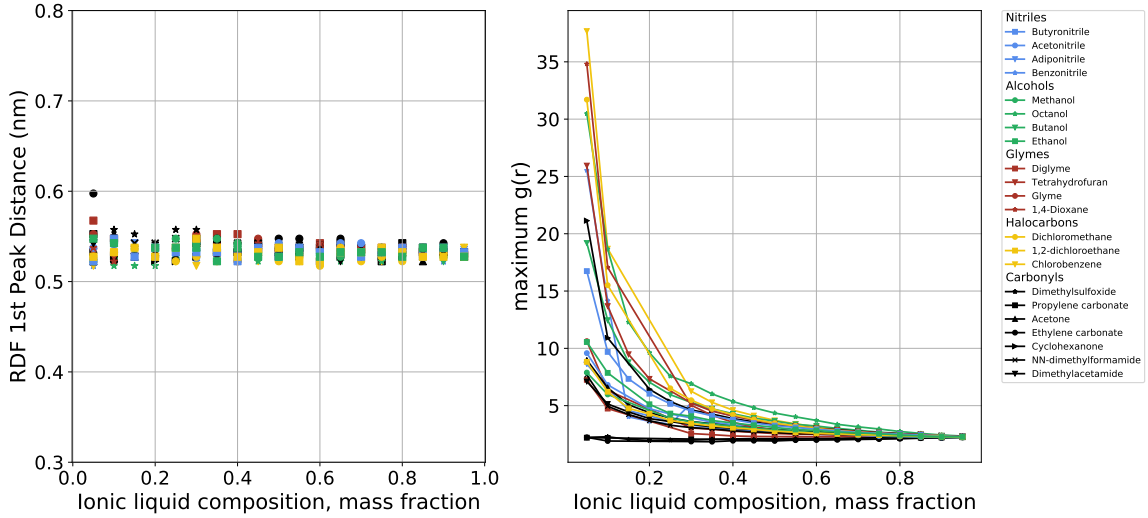

Figure 3.7: a) Location of the first peak of the RDF, $g_{max}(r_{peak1})$ as a function of ion concentration, and b) magnitude of the first peak of the RDF, $g_{max}(r_{peak1})$ as a function of ion concentration, colored by the chemical family of the solvent

3.4.7 Coordination Numbers

The coordination number (N_C) characterizes the molecular structure of a liquid by quantifying the local structure around a molecule in terms of its average number of neighbors as a function of intermolecular distance. It is defined as

$$N_C(r_C) = 4\pi\rho_{ion}\int_0^{r_C} r^2 g_{+-}(r)\rho dr \tag{3.8}$$

where N_C is the coordination number of some interatomic pair at some cutoff distance r_C, ρ_{ion} is the bulk number density of ions, $g_{+-}(r)$ is the corresponding radial distribution

function, and r is the intermolecular separation. Throughout we use $r_C = 0.8nm$, which roughly corresponds to the location of the first well in a typical RDF, to focus on the nearest-neighbor ions. We also consider only cation-anion pairs and no direct correlations with solvent molecules. A summary of the coordination numbers of these systems is presented in Fig. 3.8. In all solvents, there is a monotonic increase in N_C as a function of ionic liquid composition, which is characteristic of the nature of concentrated electrolytes. Notably, however, at low concentration, all systems exhibit non-zero coordination numbers, meaning ions are on average neighbored by 1 or 2 ions even in very dilute systems. Similar to the solvents that displayed especially large $g_{max}(r)$, N_C varies greatly among different solvents. At low concentrations, it is greater than 2 for some solvents and closer to 0.5 for others. At high concentrations, solvent effects become less relevant and these curves converge toward a bulk value near 5.

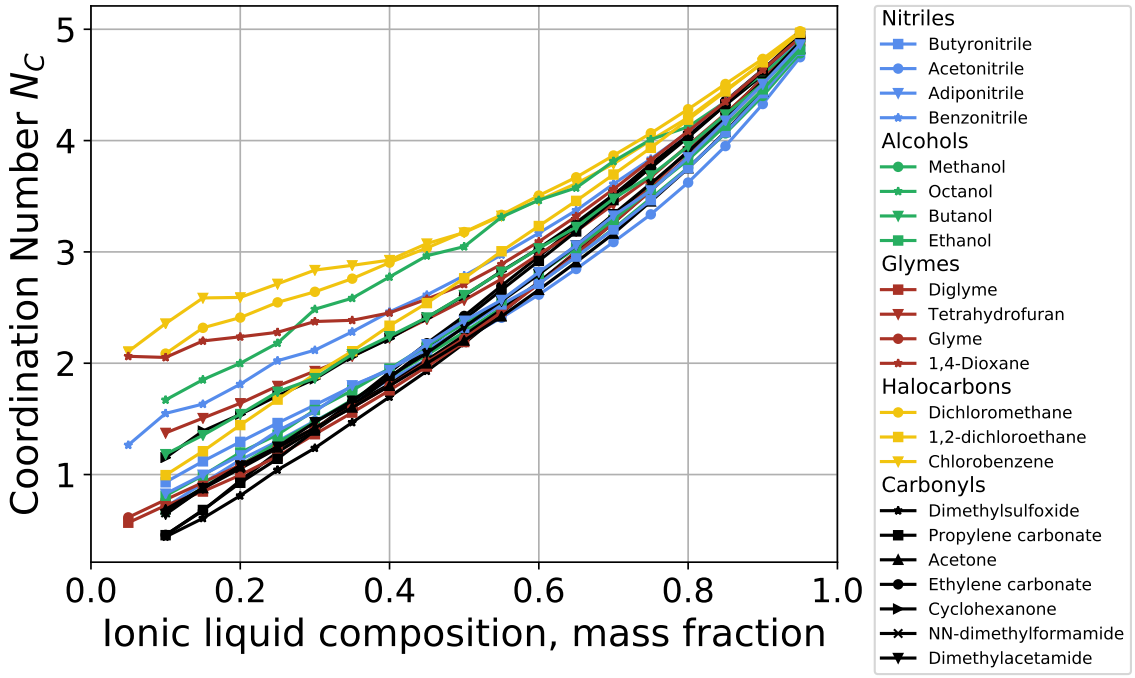

Figure 3.8: Coordination Numbers, N_C, as a function of [BMIM$^+$][Tf$_2$N$^-$] mass fraction

3.4.8 Ion Pairing as a Function of Ionic Liquid Composition

Ion correlations were computed for all state points. We first analyzed the pairing lifetimes of ions in solution as the ionic liquid composition is increased, shown in Fig. 3.9. We show ionic liquid composition in both units of mole fraction and mass fraction in order to better highlight the trends with τ_{pair}. With the exception of octanol, which is one of the most viscous solvents studied, τ_{pair} of most systems exhibit similar concentration dependence. In general, as concentration increases from intermediate compositions toward the neat regime, τ_{pair} increases. This is an intuitive result; given that ionic liquids have strong self-correlations and inherently slow dynamics, it is not surprising that an increase in ionic liquid composition results in longer pairing lifetimes. Furthermore, it should be mentioned once more that we define two ions to be paired when their distance from each other is less than a cutoff of 0.8 nm. Due to this distance criterion, we expect ions to be fully paired as we reach the neat ionic liquid limit as ions are necessarily surrounding each other. Recall that Zhang and Maginn found a strong correlation between τ_{pair} and transport properties for a set of 29 neat ionic liquids at a range of temperatures. There is, however, some degree of non-monotonic behavior at low compositions. In particular, τ_{pair} increases dramatically in the dilute limit for chlorobenzene, dichloromethane, dioxane, and cyclohexanone. These are among solvents we previously noted as promoting strongly-structured ion pairs in solution. Other commonly-studied solvents such as acetonitrile and propylene carbonate also exhibit this non-monotonic behavior, but of much lower magnitude. We attribute this largely to the interplay between strong ion-ion interactions and the ability of solvent molecules to screen them. In solvents that are less able to screen these interactions, ions exist more often in a paired state, whereas in solvents that effectively screen them, the ions are stable as free ions in solution.

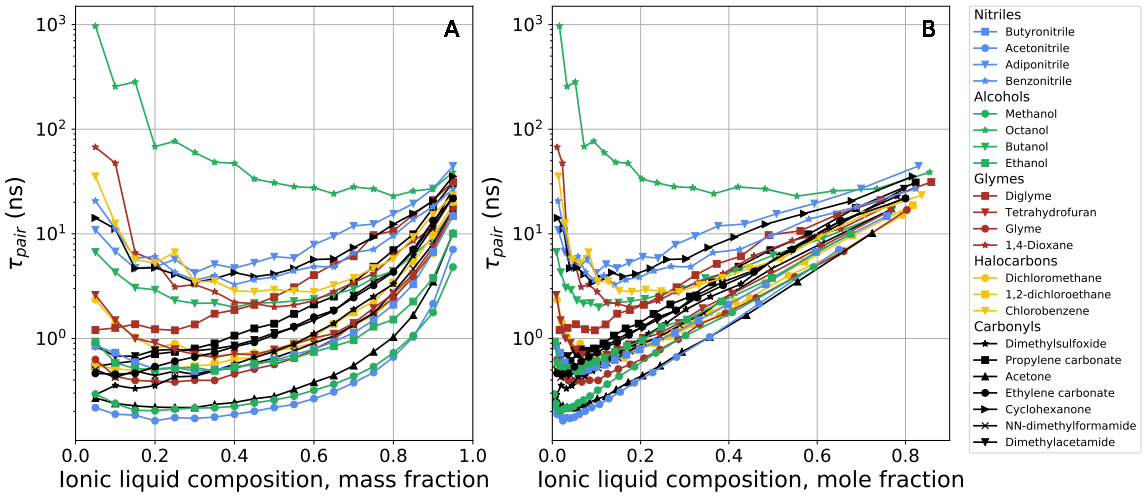

Figure 3.9: Ion pair lifetimes, τ_{pair}, as a function of a) mass fraction composition and b) mole fraction composition. Straight line segments are drawn to connect data points of common solvents

3.4.9 Ion Caging as a Function of Ionic Liquid Composition

Next, we analyze the lifetime of ion cages, τ_{cage}, over the range of ionic liquid compositions, shown in Fig. 3.10. These values are qualitatively similar to τ_{pair}, exhibiting a similar parabolic concentration-dependence. Like τ_{pair}, the majority of τ_{cage} values have a minimum at intermediate compositions and increase toward both the limit of dilute and neat ionic liquids. Their values are similar at low concentration, $\tau_{cage} \approx \tau_{pair}$, although differences between caging and pairing lifetimes are observed at other concentrations. As composition increases, τ_{cage} increases at a slower rate, resulting in $\tau_{cage} < \tau_{pair}$. Zhang and Maginn also observed this relationship for their set of neat ionic liquids. This is largely a consequence of the definition of caging in a solvated system; in the limit of infinite dilution, pairs and cages become equivalent. However, as more ions are added to a system, cages are composed of more ions and there are more chances for a cage to ”break” by losing a single ion.

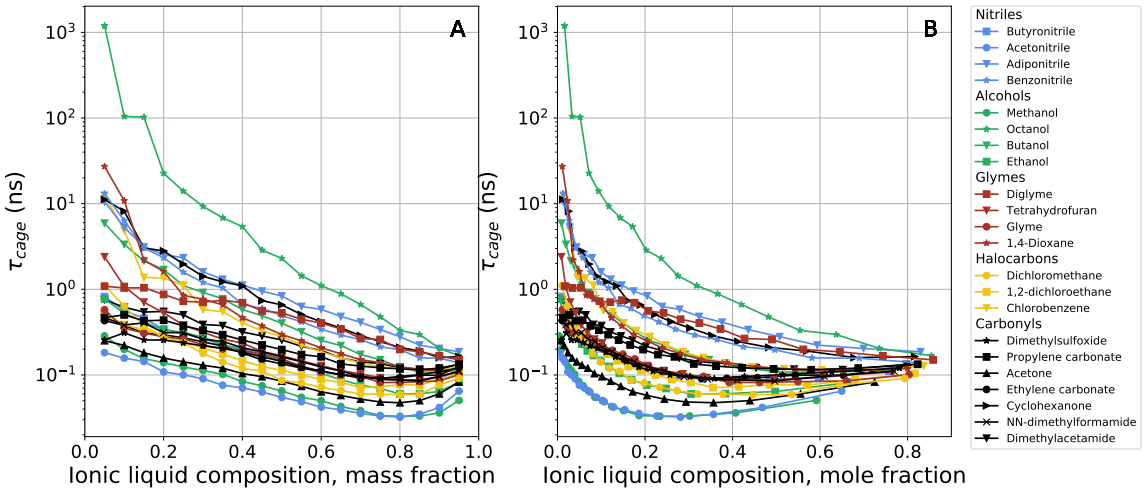

Figure 3.10: Ion cage lifetimes, τ_{cage}, as a function of a) mass fraction composition and b) mole fraction composition. Straight line segments are drawn to connect data point of common solvents

3.4.10 State of Ions in Pairs

While computing the pairing properties above, we can also extract information about the paired states of ions, if they are in pairs or free ions. This was done by computing the direct correlation matrices for each frame of the trajectory, and then calculating the ratio of free ions to the total number of ions in the system. The ratio of free ions was then averaged over all frames of the trajectory. Fig. 3.11 displays the fraction of ions that are unpaired in each solvent as a function of $[BMIM^+][Tf_2N^-]$ mass fraction. We first observe that each solvent displays a monotonic decrease in the fraction of free ions as the composition of $[BMIM^+][Tf_2N^-]$ increases. We also observe that the differences in free ions between solvents is greatest near the dilute regime of $[BMIM^+][Tf_2N^-]$. As the ionic liquid composition increases towards the neat limit, the fractions of free ions converge. In solvents including dimethylsulfoxide, propylene carbonate, methanol, and acetonitrile, most ions exist in a dissociated state at low concentrations of $[BMIM^+][Tf_2N^-]$ as indicated by the higher fraction of free ions. This result provides further evidence that these solvents are effective at screening ion-ion interactions, resulting in a lower prevalence of ion pairing. Furthermore, the ions in solvents such as chlorobenzene,

dichloromethane, 1,4-dioxane, and octanol are largely associated at low $[BMIM^+][Tf_2N^-]$ concentrations. These solvents, which display a lower fraction of free ions in solution, are suspected to be less effective at screening ion-ion interactions. Through these structural analyses, we suspect that some solvents such as dimethylsulfoxide, methanol, and acetonitrile are effective at screening ion-ion interactions, resulting in a lower prevalence of ion pairing. Consistent with this view, these solvents also exhibit a higher fraction of free ions. Furthermore, the solvents suspected to be less effective at screening ion-ion interactions such as octanol, chlorobenzene, dichloromethane, and 1,4-dioxane, display a lower fraction of free ions in solution.

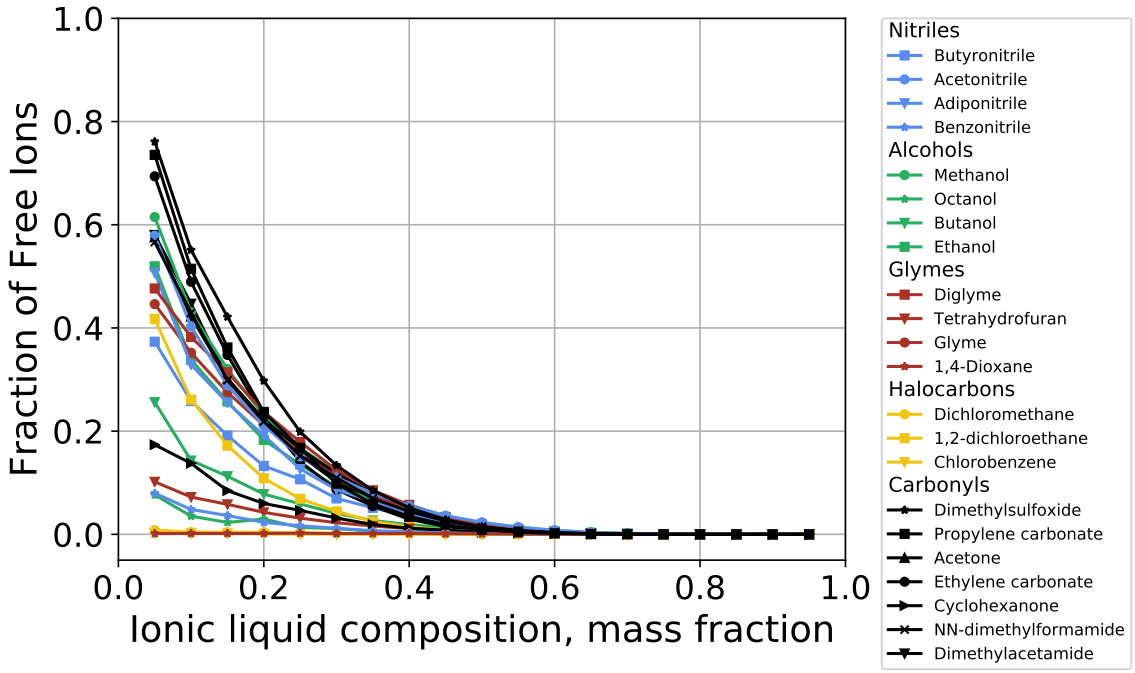

Figure 3.11: The fraction of free ions in each solvent as a function of $[BMIM^+][Tf_2N^-]$ composition.

3.4.11 Free Energy Calculations

To supplement existing transport and structural characterization of these systems, we next investigate the origins of τ_{pair} in ion-ion interactions in these solutions by computing PMFs between $BMIM^+$ and Tf_2N^-. Here, a PMF is defined as the reversible work

required to bring two molecules to separation r from infinite distance. The general formalism of a PMF is

$$\phi(\varepsilon) = -\ln \int \pi_0(x)\delta(\varepsilon - \varepsilon(x))dx,$$

where π_0 is the equilibrium distribution of the system and ε is the reaction coordinate. Here, the reaction coordinate is the intermolecular separation r. The PMFs of a single ion pair in each solvent are displayed in displayed in Fig. 3.12. The minima of these free energy curves are also summarized in Table 3.2. The free energy curve of 1,4-dioxane is the most negative free energy curve, meaning it requires more energy to separate a pair of $[BMIM^+][Tf_2N^-]$ in this solution. In other solvents (octanol, dichloromethane, tetrahydrofuran, and benzonitrile) the free energy curves also suggest that the interactions between $[BMIM^+][Tf_2N^-]$ ions are poorly screened. Recall that these solvents exhibited characteristics of strong ion pairing when looking at pair lifetimes (Fig. 3.9) and coordination numbers (Fig. 3.8), which we attributed to the inability of these solvents to screen ion-ion interactions. By comparison, the PMFs of propylene carbonate, ethylene carbonate, acetonitrile, among several other solvents, are much less negative, showing that these solvents are more effective at screening ion-ion interactions. Overall, the ion-ion PMFs in solvents at infinite dilution provides further evidence that the ability for solvents to screen ion-ion interactions significantly impacts the prevalence of ion pairing, which drives many structural and dynamical properties of these mixtures.

3.4.12 Dielectric Constants

We next compare ion pairing with the dielectric constants of the solvents. Consistent with the general picture of screening coulombic interactions, trends between the molecular polarizability of solvents and various properties of solvated ionic liquids have previously been reported. For instance, Osti *et al.* suggested solvent dipole moment as being an accurate predictor of ion dynamics for $[BMIM^+][Tf_2N^-]$ solvated in 4 various solvents[54]. From our previous study, we reported from a greatly expanded parameter space that

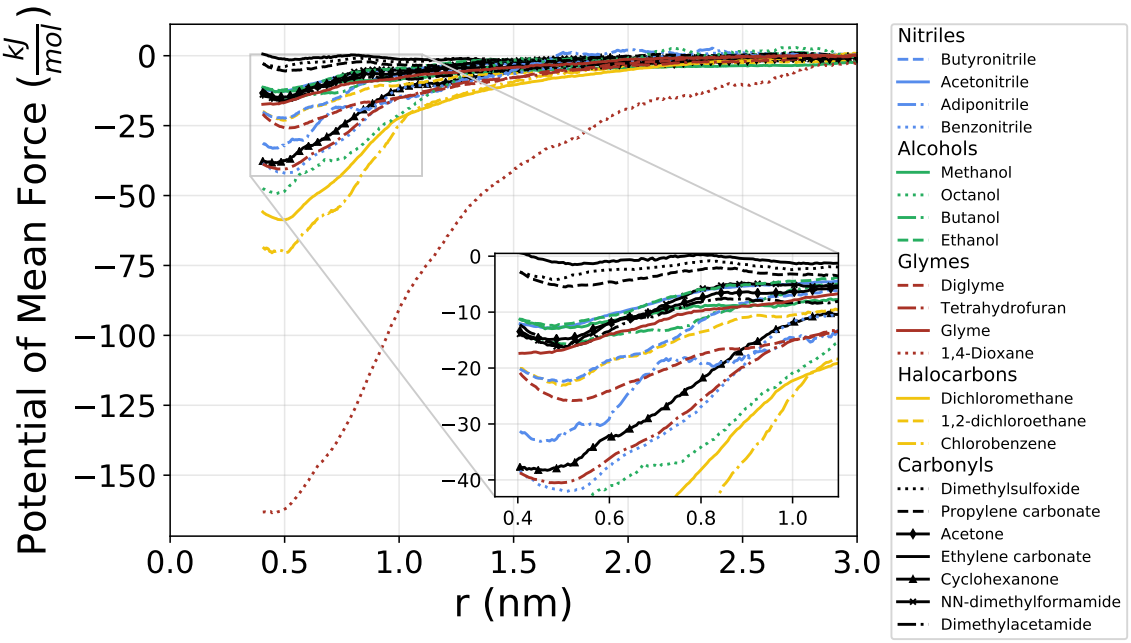

Figure 3.12: PMFs of [BMIM$^+$][Tf_2N^-] in various solvents at infinite dilution. The curves have been adjusted to decay to zero energy. A zoomed inset has been added to help visualize a subset of the PMFs.

solvent diffusivity is a more accurate predictor of ion dynamics in comparison to solvent dipole moment, which was subsequently confirmed by additional experiments[110]. McDaniel and Son similarly looked at ion pairing and the dielectric constant of solvents for solutions of [BMIM$^+$][BF_4^-] in 4 different solvents. It was reported from this study that solutions containing solvents with with lower dielectric strength exhibit longer ion pair lifetimes. To investigate the relationship between these two properties, we used the built-in tools of GROMACS[121] to estimate the dielectric constants for each of the 22 unique solvents studied. Specifically, the dielectric constants are estimated by computing the dipole-dipole correlation function which determines the total dipole moment of the system[150]. Using the total dipole moment, the dielectric constants are calculated with the following equation:

$$\frac{\varepsilon-1}{3}\frac{2\varepsilon_{rf}+1}{2\varepsilon_{rf}+\varepsilon}=\frac{\langle M^2\rangle}{9\varepsilon_0 V k_B T} \tag{3.9}$$

Table 3.2: Table of solvents and PMF peak minima values ($kJ\,mol^{-1}$). Solvents are listed from least negative minima to most negative minima.

Solvent	PMF Minimum ($kJ\,mol^{-1}$)
Ethylene carbonate	-2.35
Dimethylsulfoxide	-4.16
Propylene carbonate	-5.49
Ethanol	-12.48
Acetonitrile	-12.85
Methanol	-12.99
Acetone	-14.91
Butanol	-15.78
NN-dimethylformamide	-16.28
Dimethylacetamide	-16.31
Glyme	-17.46
Butyronitrile	-22.39
1,2-dichloroethane	-23.12
Diglyme	-25.82
Adiponitrile	-33.13
Cyclohexanone	-38.29
Tetrahydrofuran	-40.53
Benzonitrile	-42.05
Octanol	-49.32
Dichloromethane	-58.67
Chlorobenzene	-70.62
1,4-dioxane	-164.50

where ε_0 is the vacuum permittivity, V is the volume, k_B is Boltzmann's constant, T is temperature, $\langle M^2 \rangle$ is the total dipole moment, and ε_{rf} is the dielectric permittivity of the continuum, which in these summations is taken as $\varepsilon_{rf} \to \infty$ (i.e., tinfoil boundary conditions). In this case, Eq. 3.9 simplifies to:

$$\varepsilon = \frac{1 + \langle M^2 \rangle}{3\varepsilon_0 k_B T} \tag{3.10}$$

The ion pair lifetimes are plotted as a function of solvent dielectric constants in Fig. 3.13. Examining the set of solutions simulated by McDaniel and Son, the trend between ion pair lifetime and solvent dielectric constants holds well. 1,2-dichloroethane has the lowest dielectric constant out of the three solvents McDaniel and Son tested, and exhibits the

highest τ_{pair}. Following the trend, acetonitrile has the highest dielectric constant and has the lowest τ_{pair}. Additionally, there are other solvent systems with chlorobenzene and diglyme that follow this trend. The relationship between dielectric constant and τ_{pair} is less clear however when the entire chemical space of solvents is considered. Octanol has a higher dielectric constant compared to chlorobenzene, but the ions in these systems have a much higher τ_{pair}. This is similarly the case for systems containing dimethylesulfoxide, propylene carbonate, and ethylene carbonate. Overall, the monotonic decrease in τ_{pair} for systems containing 1,2-dichloroethane, acetone, and acetonitrile indicate that solvent dielectric constants play a relevant role in ion pairing. Despite this, other systems do not fit this trend, signifying there are additional solvent properties and competing interactions within these systems that influence ion pairing.

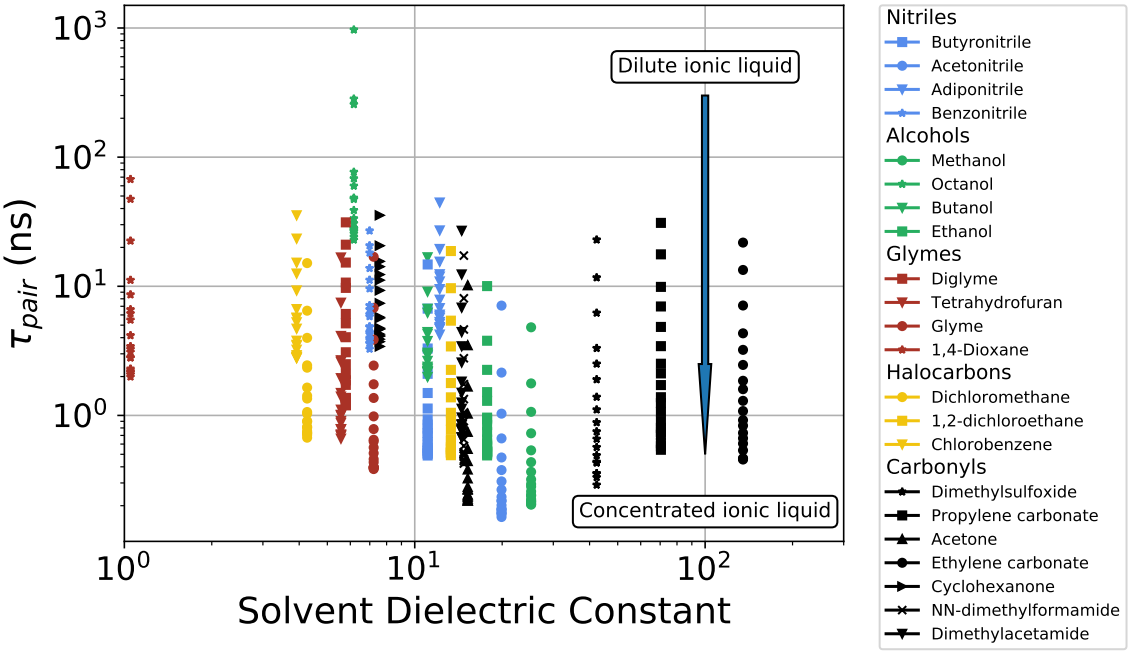

Figure 3.13: Ion pair lifetimes, τ_{pair}, of [BMIM$^+$][Tf$_2$N$^-$] solvent solutions as a function of solvent dielectric constant

3.4.13 Conductivity Measurements

We next consider the conductivities of these mixtures and investigate how they are affected by solvent properties. In accordance with previous works, we first estimated the conductivity by using the ideal ionic conductivity as a proxy. This can be computed from known values via the NE equation. Ionic conductivity is easily estimated through the NE equation due to elf-diffusivity being a single-particle property, which allows for it to be averaged over all ions in the system. A summary of the relationship between NE ionic conductivity and mixture compositions presented in Fig. 3.14. In agreement with prior works, including that of Osti *et al.*[54], the maximum conductivity is observed at intermediate compositions. This is due to the counterplay between faster ion dynamics resulting from greater solvation and, by definition, the decrease in ionic density that results in fewer charge carriers: neat ionic liquids exhibit moderate conductivity; however, in the limit of infinite dilution, ion dynamics approach bulk solvent dynamics, but the capacity to carry charge is inherently lost. In most solvents, conductivity maxima are observed near equimass compositions of ionic liquid and solvent. Notable here is that acetonitrile-based mixtures exhibit the greatest conductivity of any mixture over the entire range. This implies that acetonitrile should remain a popular solvent for electrochemical applications. However, these results indicate the existence of viable alternatives if acetonitrile is to be avoided.

Next the ionic conductivities were estimated through the EH formalism (Fig. 3.15), which better takes into account the correlated motions of ions. The EH conductivities follow the same trend, with maxima being located roughly in the range of 0.3-0.6 mass fraction $[BMIM^+][Tf_2N^-]$. The solvent mixtures with the highest ionic conductivity as calculated by EH are those containing acetonitrile, methanol, and acetone. Looking once again at Fig. 3.18, these mixtures have the shortest ion pairing lifetimes. Conversely, the mixtures containing octanol and adiponitrile display the lowest EH conductivties and the longest ion pair lifetimes. Thus it seems that the longer the ions stay paired in solution, the lower

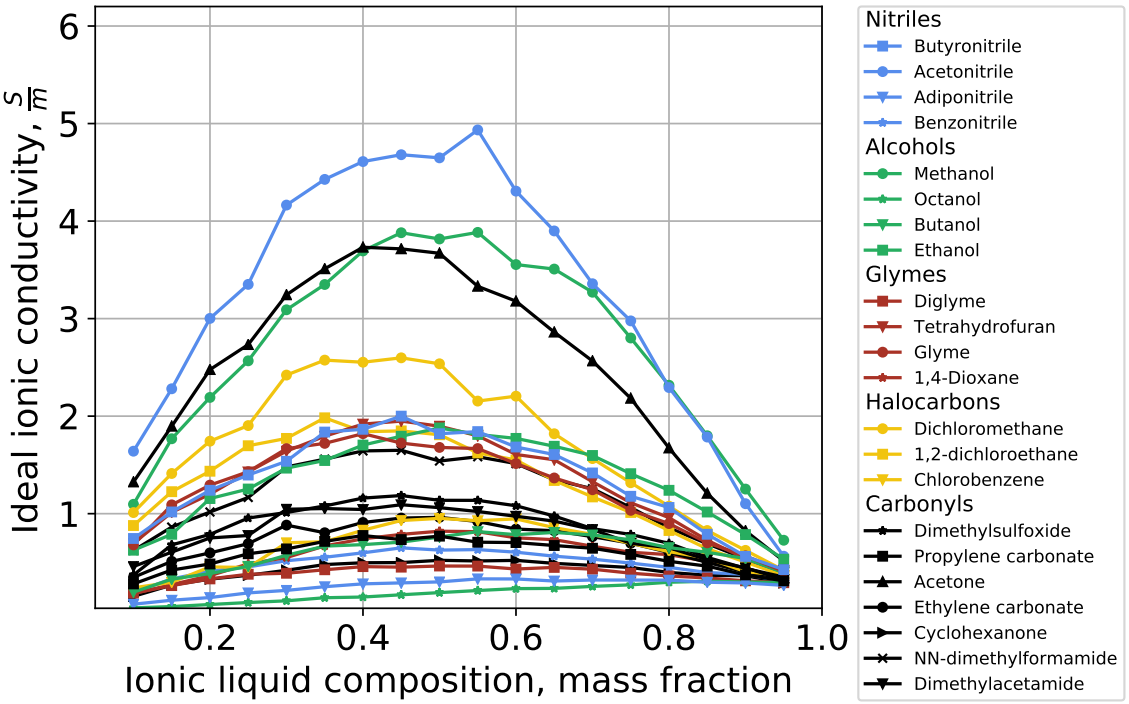

Figure 3.14: NE ionic conductivity as a function of ionic liquid composition. NE ionic conductivity is highest at intermediate ionic liquid compositions.

the conductivity estimated through EH is. This is understandable as EH conductivity accounts for correlated motions of ions.

We now compare the conductivities computed through EH and NE using the ionicity ratio. Consistent with similar studies, this ratio is less than 1.0 for most systems; equivalently, $\sigma_{NE} > \sigma_{EH}$. The Einstein-Helfand formalism is considered more rigorous and is believed to produce more accurate estimates of ionic conductivity. Therefore we conclude that the Nernst-Einstein equation overestimates the real ionic conductivity for most of these systems. This error is typically attributed to the assumption that ion motion is decorrelated; we earlier in this manuscript and elsewhere in the literature others have established this to be unreasonable for ionic liquid - solvent systems.

Beginning in the regime of dilute [BMIM$^+$][Tf$_2$N$^-$], mixtures containing solvents such as dichloromethane, 1,4-dioxane, and chlorobenzene display low α values. A low α implies the effects of ion correlations on conductivity are particularly strong. Notably, many of the

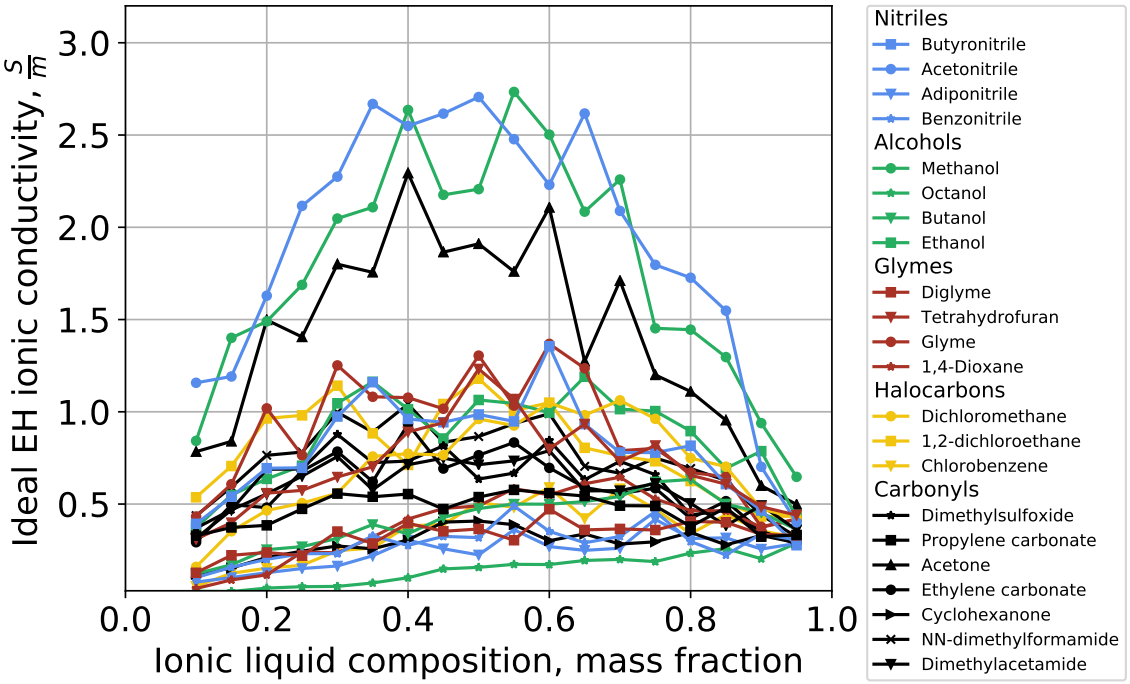

Figure 3.15: Einstein-Helfand conductivity as a function of ionic liquid composition. Like Nernst-Einstein, the Einstein-Helfand conductivity is highest at intermediate compositions

solvents with small α also have strong pairing as described in earlier sections. However there are other mixtures, such as those including octanol and cyclohexanone, that have intermediate conductivity ratios despite exhibiting generally strong pairing properties. This result suggests there are other competing effects influencing the conductivity as calculated by EH. Near the neat ionic liquid limit, the α values appear to be highest, indicating that the NE approximation for conductivity is most valid for these solutions. Once again this is broadly consistent with the structural properties evaluated previously. There are a small number of mixtures in Fig. 3.16 with $\alpha > 1$. While this is not commonly observed in ionic liquids, Salanne *et al.* found $\alpha > 1$ in viscous mixtures of the molten salts LiF and BeF_2 [39]. They attributed this observation to cooperative motion in which the ions moved in the same direction as promoted by channel-like structures formed in the solvent. Rather than hindering their motion, this view implies that the correlated nature of ions can actually improve conductivity. Although the σ_{EH} data, and therefore α values,

are somewhat noisy, it is evident that the most common cases of $\alpha > 1$ occur with two of the most viscous solvents, adiponitrile and diglyme. This is consistent with the interpretation of Salanne *et al.*, however given the inherently slow dynamics of these mixtures it is difficult to take advantage of this effect in viscous solvents compared to solvents with lesser viscosity.

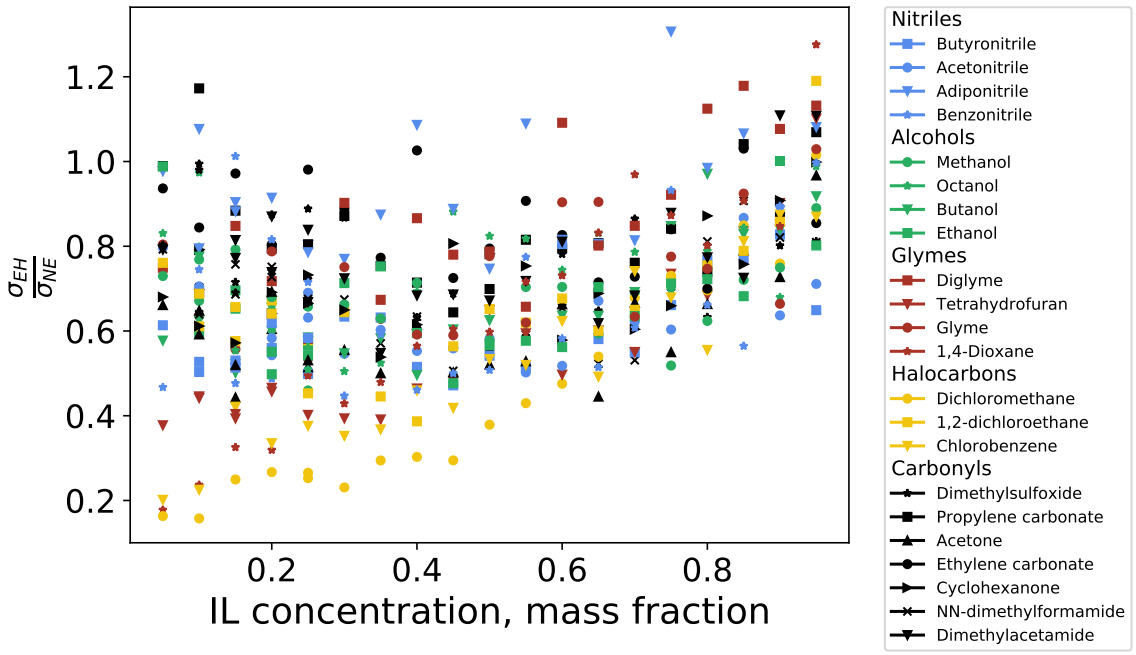

Figure 3.16: A ratio of Einstein-Helfand conductivity and Nernst-Einstein conductivity

These conclusions from computational screening were evaluated by, and supported by, experimental conductivity measurements. A comparison between simulation predictions and experimental results for a subset of the studied solvents is presented in Fig. 3.17. We selected acetone, dichloromethane, and methanol, which were among the solvents that produced mixtures with the highest conductivity. The trends observed in experiment are consistent with our simulation results: a moderate composition of approximately 0.4 to 0.6 mass fraction ionic liquid produces mixtures with the highest conductivity. In addition, the relative conductivity of [$BMIM^+$][Tf_2N^-] in acetone, dichloromethane, and methanol at low mass fractions, derived from the computational studies, ($\sigma_{inacetone} > \sigma_{inmethanol} > \sigma_{indichloromethane}$ is also seen experimentally. Interestingly, in the

simulations there is a crossover from $\sigma_{inacetone} > \sigma_{inmethanol}$ to $\sigma_{inacetone} < \sigma_{inmethanol}$ occurring at an ionic liquid mass fraction of 0.4; the experiments also suggest a similar crossover, though occurring at higher mass fraction.

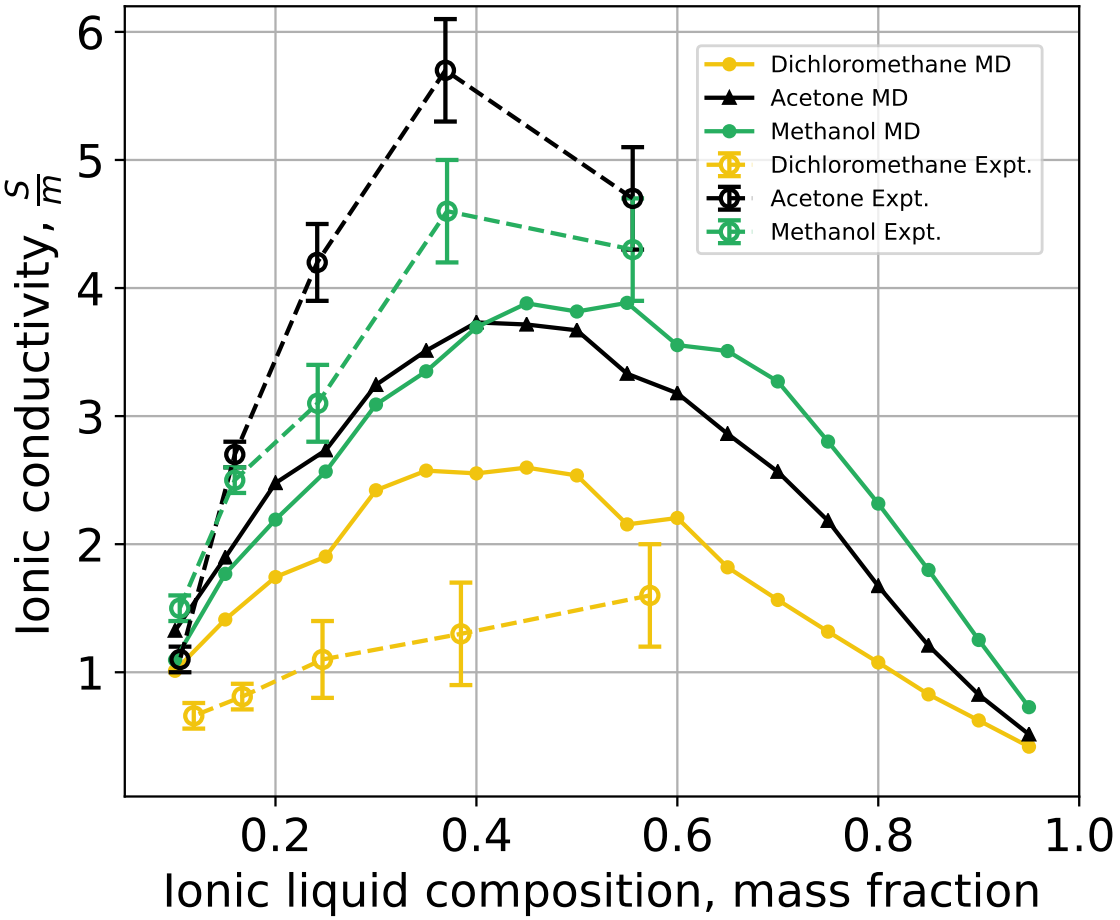

Figure 3.17: Comparison between simulation predictions (solid lines) and experimental measurements (dashed lines) of the ionic conducivity of select mixtures as a function of composition.

3.4.14 Connecting Structure and Dynamic Properties

To better understand the implications of the pairing and caging properties τ_{pair} and τ_{cage}, we attempt to connect these structural properties to transport properties.

Previously-computed ion diffusivities are plotted against τ_{pair} in Fig. 3.18. As with ionic liquid composition, two distinct trends are observed between ion diffusivity and pair

lifetimes. The same solvents that showed a more monotonic trend between τ_{pair} and ionic liquid composition, such as acetonitrile and propylene carbonate, show a roughly monotonic decrease in ion diffusivity as τ_{pair} increases. As such, it appears that ion pairing in these solutions negatively affects the ion dynamics. Similar trends have been observed by Zhang and Maginn for various ionic liquids using non-polarizable force fields[85] and by McDaniel and Son for $[BMIM^+][BF_4^-]$ in four solvents at various concentrations using the SAPT polarizable forcefield[151]. Also shown in Fig. 3.18 is that solutions with solvents that have the shortest ion pair lifetimes also exhibit the highest ion diffusivities. For example, we previously reported that acetonitrile solutions exhibited the highest diffusivites from this data set[108]; ion pairing analyses now indicate that the same acetonitrile solutions also exhibit the shortest ion pair lifetimes. Consistent with previous structural analyses, from screening over many solvents we observe that some solutions, such as those containing 1,4-dioxane and chlorobenzene, do not follow this monotonic trend in Fig. 3.18. When revisiting Fig. 3.9, the systems with strongly non-monotonic curves also experienced the highest initial decrease in τ_{pair} as a function of ionic liquid composition. The ions in these systems are paired in large quantity and for long times at low ion compositions, but this pairing does not appear to affect the diffusivity of these ions. In general, however, we would expect the longer ion pairing lifetimes of these systems to negatively impact conductivity.

3.5 Additional Insights from QENS

After completion of the computational screening study, a disagreement existed with the original work of Osti *et al.*. To resolve this, we discussed these results with our experimental collaborators at ORNL, Naresh Osti and Eugene Mamontov, who were the main authors of the initial study of ionic liquids in organic solvents. To investigate the conflict, they designed an experiment to isolate the effects of solvent diffusivity and solvent polarity[110]. Four organic solvents of nearly identical dipole moments but greatly

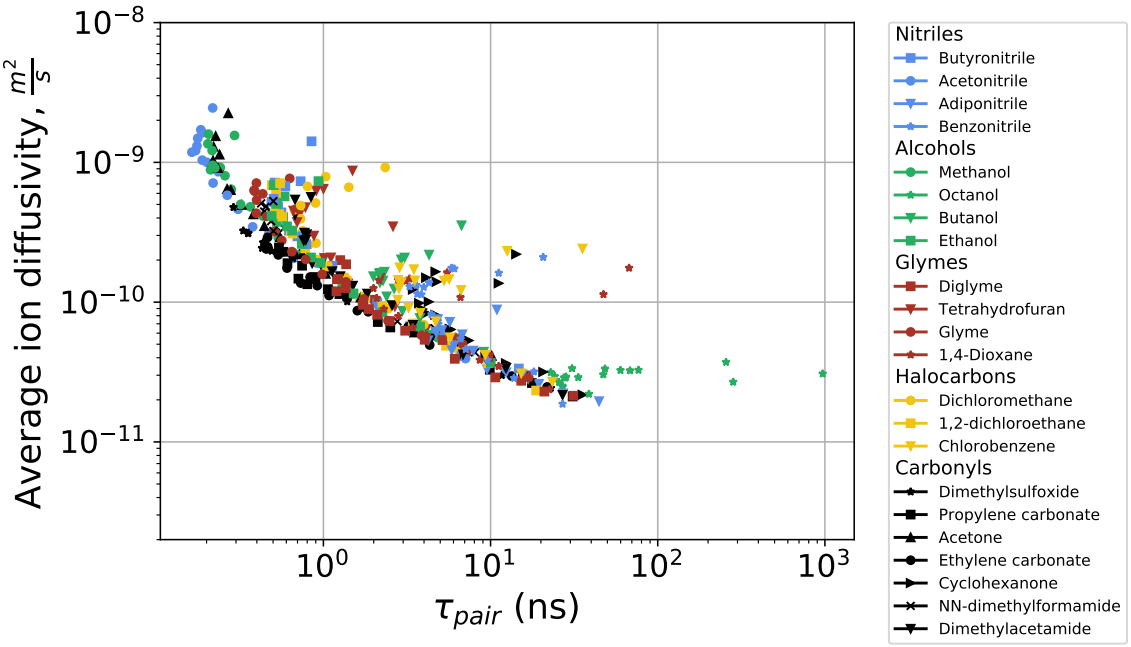

Figure 3.18: Average ion diffusivity of [BMIM$^+$][Tf_2N^-] as a function of ion pair lifetimes, τ_{pair}

Table 3.3: Solvents analyzed in QENS study.

Solvent	dipole moment (d, Debye)	diffusivity ($D, 10^{-10} m^2 s^{-1}$)
dichloromethane	1.60	15.7
octanol	1.68	0.4
butanol	1.66	2.7
tetrahydrofuran	1.75	8.5

different dynamic properties were chosen and are highlighted in Table 3.3. If the relationship with solvent diffusivity established through screening were to hold true, QENS would show a similar trend between ion diffusivity in solution and bulk solvent diffusivity for the four solvents. If solvent polarity was the dominant influence on ion dynamics however, we would see little correlation between the diffusivities. Based on Fig. 3.19, the diffusivity of the ions in solution show a monotonic relationship with the bulk diffusivity of the solvents similar to that of Fig. 3.4. This provides further evidence, and validation from experiments, that the diffusivity of bulk solvents is a strong predictor of the diffusivity of ions in ionic liquid and organic solvent mixtures.

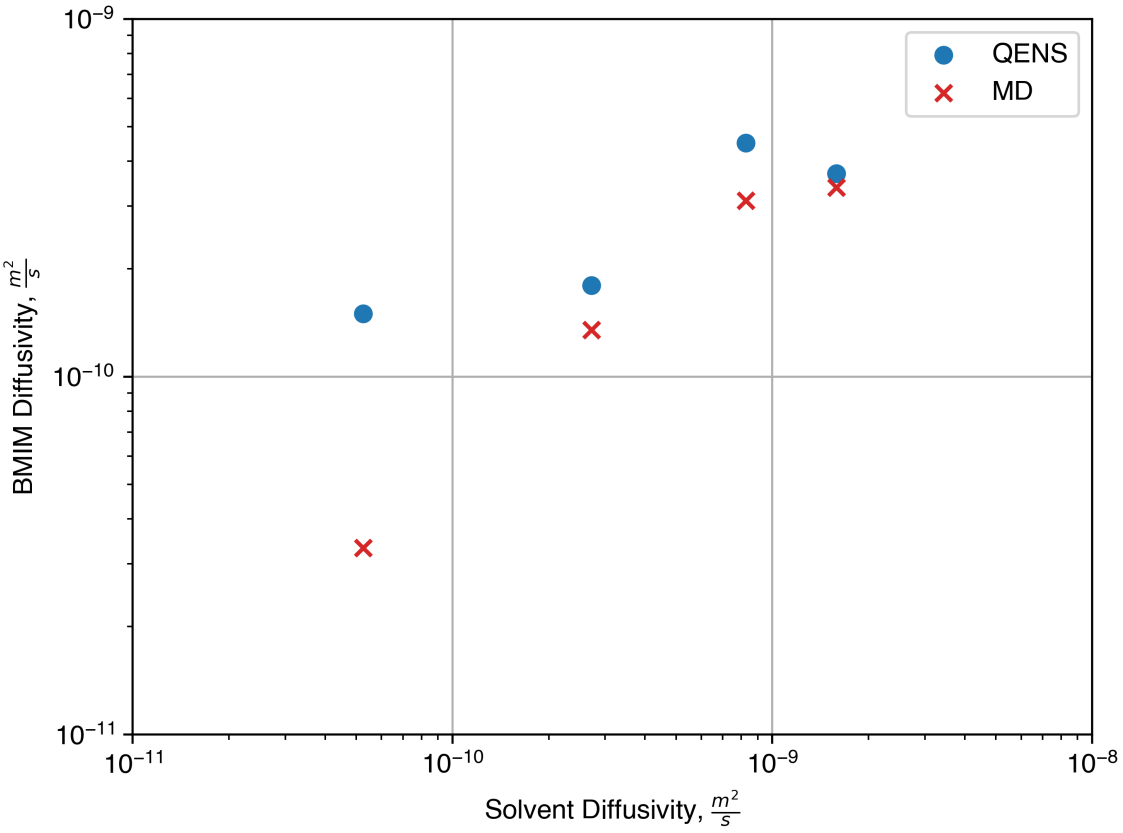

Figure 3.19: Symbols: experimentally obtained diffusivity values for $BMIM^+$ cation in 50 wtpct $[BMIM^+][Tf_2N^-]$ (IL-rich domains), plotted as a function of diffusivity of the organic solvent in the corresponding solution (as obtained from MD simulation). Data taken from Ref. 110

3.6 Insights from PFG-NMR

At this point, the trend regarding ion diffusivity and bulk diffusivity in ionic liquid and organic solvent mixtures was partially validated through additional QENS measurements. Although further insight was gained, only a fraction of the solvents studied through screening were investigated. Although it is unfeasible to measure diffusivities for a large number of systems through QENS, these values can be computed through PFG-NMR at a lower cost. Our collaborators, Jinlei Cui, Takeshi Kobayashi, and Marek Pruski of The Ames Laboratory, provided an additional follow-up to our screening study by measuring the diffusivities of ionic liquids in 10 solvents[111]. Concentrations of 10%, 30%, and 60% ionic liquid mass fraction were considered. Robert Sacci from ORNL also provided

Solvent	ξ	coordination number, n
acetonitrile	0.59	0.12
adiponitrile	0.98	0.13
methanol	0.83	0.67
octanol	0.29	2.09
1,2-dichloroethane	0.58	1.11
acetone	0.45	0.59
dimethylsulfoxide	0.54	0.23
glyme	0.35	0.42
diglyme	0.50	0.49

Table 3.4: Solvents analyzed in PFG-NMR study. Data taken from Ref. 111.

further conductivity measurements. The solvents studied are listed in Table 3.4.
Ion diffusivity as a function of neat solvent diffusivity measured by PFG-NMR is displayed in Fig. 3.20. Similar to the results of Fig. 3.4 and Fig. 3.19, a positive correlation exists between the diffusivity of $BMIM^+$ in solution and the diffusivity of the bulk solvent. This provides further validation for the trend originally predicted from the MD simulations. Additionally, it was found that the solvent diffusivity is roughly double the $BMIM^+$ diffusivity in solution, $\frac{D_{solvent}}{D_{BMIM^+}}$~2. This ratio can be analyzed along with the diffusivity defined by the Stokes-Einstein equation:

$$D = \frac{k_B T}{c\pi\eta r_s} \tag{3.11}$$

where k_b is Boltzmann's constant, T is the absolute temperature, η is the dynamic viscosity, r_s is the Stokes radius, and c is a constant equal to 4 in the case of the slipping boundary limit. In the case of the ionic liquid-solvent mixtures, c and η are consistent and thus the diffusivity ratio corresponds to the ratio of Stokes radii:

$$\frac{D_{solvent}}{D_{BMIM}} = \frac{r_{BMIM}}{r_{solvent}} \equiv \rho_{BMIM} \tag{3.12}$$

In the case of these mixtures, the Stokes radius of the diffusing particle involving $BMIM^+$

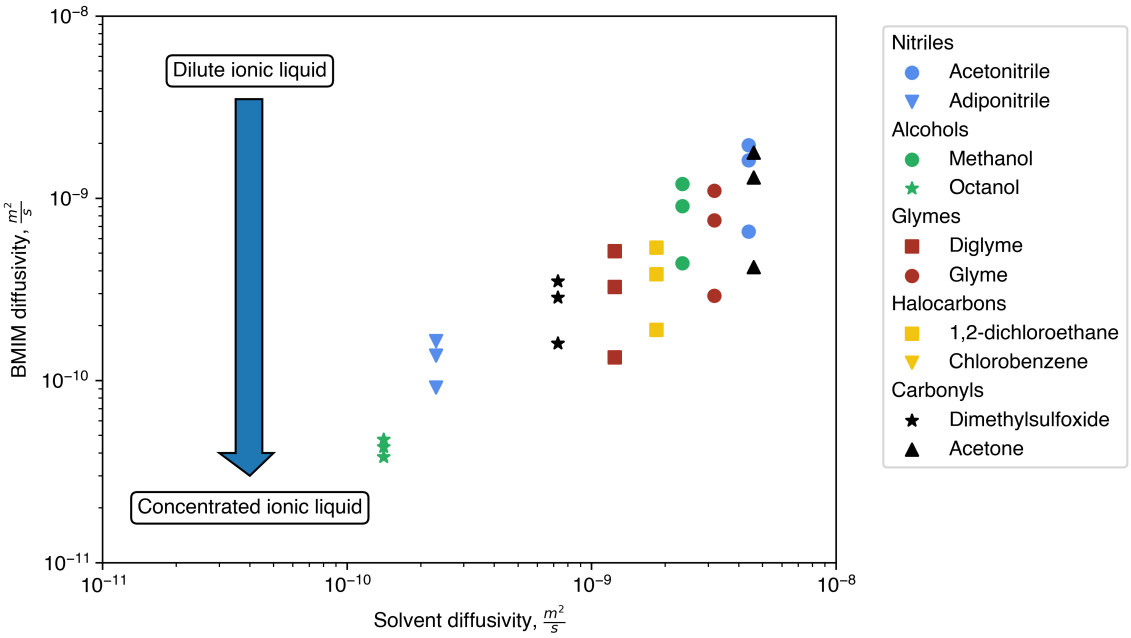

Figure 3.20: Ion diffusivity as a function of neat solvent diffusivity measured by PFG-NMR. Data taken from Ref. 111.

is roughly twice that of the solvent molecule.

Similar to the ionicities calculated from the MD simulations through the NE and EH ionic conductivities, the ionicity was calculated through the NE conductivities estimated from PFG-NMR, and the conductivities experimentally measured, σ_{obs}. The conductivities and ionicities are displayed in Fig. 3.21. Methanol and adiponitrile display high ionicities while octanol displays the lowest ionicity. The ionicities can be used to estimate the hydrodynamic size of diffusing particles and the coordination number of solvent molecules. The Stokes radius of $BMIM^+$ in solution is defined by the equation:

$$\bar{r}_{BMIM} = r^{neat}_{BMIM}\xi + (r^{neat}_{BMIM} + r^{neat}_{Tf_2N})(1-\xi) \tag{3.13}$$

where r^{neat}_{BMIM} and $r^{neat}_{Tf_2N}$ are the Stokes radii of ions in a neat ionic liquid.

The coordination number, N_C, can then be estimated from the equation:

$$\rho_{BMIM} = \frac{\bar{r}_{BMIM} + N_C r^{neat}_{solvent}}{r^{neat}_{solvent}} \tag{3.14}$$

The values of N_C suggest $BMIM^+$ contains less than one solvent molecule in its first neighbor shell. The rarity of the solvent-ion interactions may explain the significant influence of viscosity of the neat solvent on the ion diffusivities. For instance, the smaller diffusivity of neat ions versus the diffusivity of solvent in the octanol mixture may be explained by the low ionicity. Additionally, the high ionicity and low solvent coordination number in adiponitrile may explain why the ratio of diffusivity of ions to solvent is much closer to one.

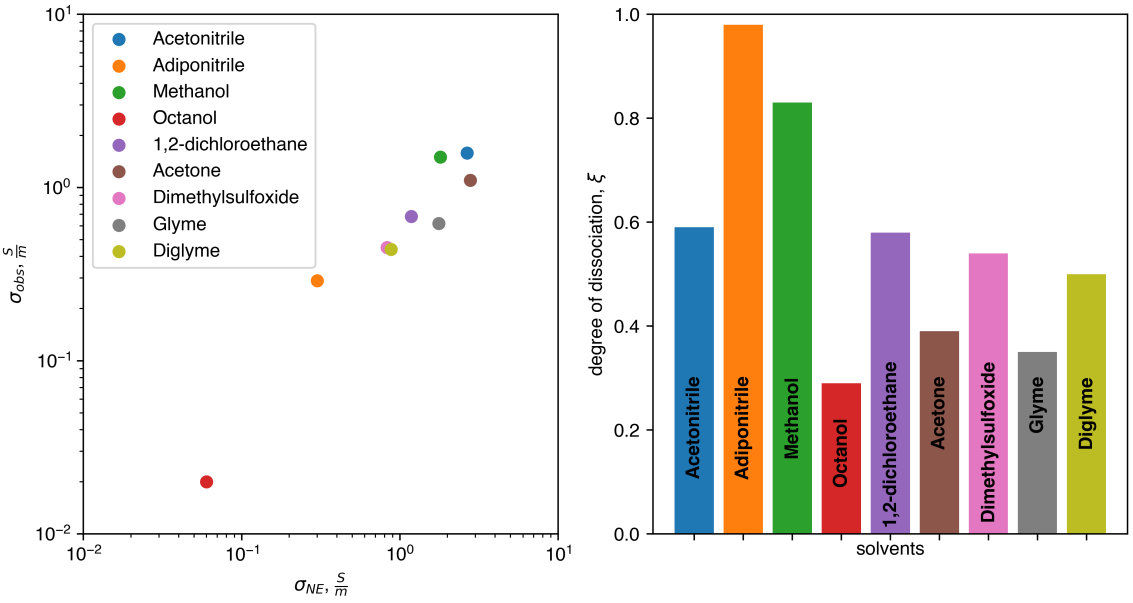

Figure 3.21: a) Comparison of ionic and molar conductivities for 0.1 IL mass fraction of $[BMIM^+][Tf_2N^-]$ and b) ionicity. Data taken from Ref. 111.

3.7 Conclusions

In this chapter, the initial study of Osti and coworkers was first introduced in which $[BMIM^+][Tf_2N^-]$ was studied in four organic solvents. Two trends in relation to ion diffusivity were established: (1) ion diffusivity decreases as a function of ionic liquid

composition and (2) ion diffusivity increases as a function of solvent polarity. To expand upon this work, a computational screening study was conducted in which the parameter space was increased to 23 organic solvents and 18 concentrations. These results predicted that bulk solvent diffusivity, not solvent polarity, is the primary solvent property that influences ion dynamics. Conductivity was found to be highest at intermediate concentrations of ionic liquids. Summaries of ion pairing and caging, RDFs, coordination numbers, and ratios of paired to free ions provide a deeper understanding of ion structure: pairing is strongest at very low composition and in solvents that poorly screen ion interactions. Conversely, pairing effects are most mitigated at intermediate compositions and in some solvents, such as acetonitrile and carbonates, that screen ion interactions. We investigated a relationship between the dielectric constant of solvents and pairing lifetimes of the corresponding ionic liquid mixtures. While a trend exists for a portion of the data space, the screening of many solvents better informs us that this trend is not applicable over the enter parameter space; dielectric screening appears to be an important factor, but the overall screening of ion-ion interactions depends on other factors as well. To this end, we obtained from free energy calculations a series of PMFs that describe the thermodynamics of pulling apart an ion pair in each solvent. We observe large variation among the solvents in accordance with the structural and dynamic properties observed. From these results, we conclude that the ability of solvents to screen ion-ion interactions, as manifested by the strength, frequency, and duration of ion pairing, is partially responsible for the enhanced transport properties of these mixtures.

To provide validation for the predictions of computational screening, ion diffusivity of $[BMIM^+][Tf_2N^-]$ in four solvents with nearly identical dipole moments but different diffusivities were measured through QENS. A similar monotonic trend between ion diffusivity in solution and bulk solvent diffusivity was observed for the four solvents studied, showing agreement with our predictions. Further validation was provided from our collaborators at the Ames Laboratory, in which ion diffusivity in 10 organic solvents

was measured through PFG-NMR. Similar to the results of MD simulation and QENS, a positive correlation was shown for ion diffusivity and bulk solvent diffusivity. Additional insights on the solvent-ion interactions were provided. The ionicity and ratio of Stokes radii between solvent molecules and ions indicated that ions are weakly solvated in these mixtures. The lack of solvent-ion interactions provides a possible explanation as to why bulk solvent diffusivity is the dominant factor on ion dynamics of these systems. Altogether, a comprehensive view of the structural, transport, and thermodynamic properties of mixtures of ionic liquids in organic solvents, over a wide range of compositions and solvents, provides unique insight into the connections of these properties. We hope these results can inform the design of new ionic liquid-based electrolytes for a range of energy applications.

3.8 Future Work

There are several possible directions in which to continue research of ionic liquid and organic solvent mixtures. First, the same ionic liquid, $[BMIM^+][Tf_2N^-]$, can be further studied with MD simulation using more recent and/or more complex force fields. The CL&P force field with scaled partial charges does a good job at predicting ion transport properties. However, Schroder *et al.*[152] showed that the local coordination of ions in scaled partial charge models deviates from more accurate polarizable models. As a result, these systems could be further studied through the force fields of Koddermann *et al.*, in which certain force field parameters of CL&P were reparameterized to avoid partial charge scaling while obtaining accurate transport properties[153]. Goloviznina, Lopes, Gomes, and Padua also published a polarizable force field for ionic liquids in 2019[154], which may also provide new insights on the interactions between ions and solvents. Special care must be taken however to select a polarizable force fields for solvents that is compatible with the polarizable ionic liquid force field.

To fulfill the name of ”designer solvents”, the properties of many more ion combinations

should be understood. An additional avenue of research is to study additional combinations of cations and anions which comprise ionic liquids.

Discussed in much more detail in Chapter 4, the Van Hove Function can be computed for a system of ionic liquids and solvents to analyze the correlated dynamics. This may allow us to further understand the local dynamics between cations and anions, and between ions and solvents.

Lastly, the properties of these solutions should be analyzed under confinement of energy-relevant materials, such as porous carbon and MXenes. Work in this area has already begun. Yu Zhang investigated the capacitance values of ionic liquid and acetonitrile electrolytes under confinement of various porous carbons[155]. Xuehang Wang *et al.* also investigated the charge storage of various organic electrolytes under confinement of MXenes[156]. From these experiments, electrolytes containing acetonitrile or dimethylsulfoxide result in lower overall charge storage capability in comparison to those with propylene carbonate. These studies show that the selection of electrode material and confinement effects play a major role in the properties of electrolytes and must be considered. A better understanding of the interplay between ions, solvents, and electrodes may allow for the design of more efficient supercapacitors.

CHAPTER 4

Understanding the Microscopic Dynamics of Fluids through the Van Hove Function

4.1 Introduction

To design more efficient supercapacitors, we must fully understand the dynamics of electrolytes at a molecular level. The behavior of electrolytes is strongly dependent on the ion and solvent selection and has been widely researched[23]. In Chapter 3, the effects of solvation on ionic liquids are discussed in great detail. While we believe solvent selection has an immense impact on on dynamics, the microscopic mechanism remains unclear. In particular, the description of collective and correlated dynamics of electrolytes is still not fully understood, which is important to understanding macroscopic properties. Experimentally, the structure of fluids have been extensively studied through the pair distribution function (PDF) through x-ray and neutron scattering techniques[157–161]. Further, the dynamics have been studied through QENS and NMR, although these techniques are limited to the self-motion of fluids. Recently our experimental collaborators have been able to measure the time-dependent PDF, known as the Van Hove Function (VHF), at a high enough resolution through inelastic x-ray scattering (IXS) to study the correlated motions of water. [1]

In this chapter, we describe the comparison of the VHF of water through various molecular simulation methods and IXS. This work is currently in preparation[163]. Then, a method at which to investigate the microscopic dynamics of electrolytes through an integrated study of experimental scattering techniques and molecular simulation is discussed[162].

[1] Aqueous Electrolyte work reprinted with permission from Y. Shinohara, R. Matsumoto, M. Thompson, C. Ryu, W. Dmowski, T. Iwashita, D. Ishikawa, A. Baron, P. Cummings, and T. Egami, Journal of Physical Chemistry Letters **10** (2019), ISSN 19487185, Copyright 2019 American Chemical Society.

4.2 Background

Electrolytes for energy storage have been well-described through many modes of analysis, including but not limited to, the calculation of self-diffusion coefficients, PDFs, and viscosity. Despite the immense progress made, there is still much to be understood regarding electrolytes and the molecular origins of their properties. This is partly due to the limitations of current analysis methods. For instance, the PDF describes the distribution of the distance between two atoms at the same time. However, it is a thermally averaged snapshot of the distribution which does not provide information on the dynamics of such correlations. MD simulations, PFG-NMR, and QENS have been utilized to measure diffusivity, as shown in Chapter 3, although these techniques are limited to the self-motion of particles. The correlated motion of particles can be analyzed through the calculation of the time-dependent PDF, also known as the VHF. The VHF was first introduced in 1954[164], which can be obtained through IXS and inelastic neutron scattering (INS) and by taking the double Fourier Transform of the dynamic structure function. It has been difficult however to measure the dynamic structure factor over a wide enough range of momentum and energy transfer until recently. In 2017, Iwashita *et al.*[165,166] reported the first VHFs of water through the use of IXS in which water molecules were found to be correlated in both space and time. Egami and coworkers have since reported subsequent studies which analyze water and aqueous electrolytes through the VHF[167,168]. The VHF can be used to study the correlated dynamics of water and various electrolytes. For several decades, molecular simulation has accompanied experiments towards advances in energy storage[169–171], biology[172–176], materials[177–179], etc., with the ability to provide a thorough description of the microscopic behavior of molecules. One limitation of the VHF obtained through x-ray scattering experiments is being a statistical average over all atoms of a system, making it difficult to determine which pairwise elemental interactions most strongly influence macroscopic behavior[162]. Molecular simulation can interrogate individual components of the overall VHF due to the knowledge of all atomic

positions at each point in time, serving as a complement to experimental techniques. Other properties of fluids including diffusivity, viscosity, and shear modulus, can additionally be calculated through molecular simulation, allowing for a more rigorous analysis. For these reasons, molecular simulation is a powerful tool alongside x-ray and neutron scattering in studying the microscopic behavior of soft-matter. To study fluids with molecular simulation through the VHF, the computational models should be validated to ensure that the experimental response is sufficiently replicated.

In this chapter, comparison and validation of various water models through the VHF is discussed. This work is in collaboration with Yuya Shinohara, Takeshi Egami, Paul Kent, Van Quon Vuong, and Stephan Irle of ORNL, and Weiwei Zhang and Adri van Duin of Pennsylvania State University.

Numerous models of varying types and complexity exist to describe the interactions of water. Classical and reactive models are empirical and are generally fitted to experimental or density functional theory (DFT) data. Perhaps the most widely used CMD models to describe water are rigid, point-charge models such as SPC/E[82] and TIP3P[83] due to their relative accuracy in reproducing experimental properties in a computationally efficient manner. Though these models are computationally cheap and relatively accurate, a common downside is a lack of accuracy at conditions in which the model was not parametrized[180]. Polarizable models such as the Gaussian charge polarizable model (GCPM)[79] and BK3[181–183], while more computationally expensive, aim to more accurately represent the interactions of water through Gaussian charge distributions instead of point charges and the inclusion of a polarizable term. In addition to classical models, reactive methods such as ReaxFF[184] include additional terms that allow for the chemical reactions of a system to be modeled. The CHON-2017_weak ReaxFF parameters, in particular, show good agreement with experimental values of bulk water[185]. Semi-empirical quantum mechanical (QM) methods are more computationally expensive than classical methods, but attempt to provide a more accurate representation of

a system with the inherent inclusion of certain phenomena such as chemical reactions[186,187].. Density-functional tight-binding (DFTB)[188,189] belongs to this class of semiempirical QM methods, as it is an approximation to DFT based on the two-center approximation and the use of a minimal basis set for construction of the valence electron Hamiltonian. Its approach to replace the computation of expensive integrals derived from DFT allows routine large-scale simulations on nanosecond time scales. Its 3obw parametrization was partially obtained by the technique of iterative Boltzmann inversion and reproduces many of the properties of bulk water, including bulk RDFs[190]. *Ab initio* MD is the most complex and computationally expensive method discussed here, in which electronic structure calculations are calculated on the fly to generate the forces for dynamics. *Ab initio* models benefit from being unbiased to a given state, a specific downside of empirical force fields[191,192]. Though this generally means these models are not fit to experimental data. Transferability is less of an issue with *Ab initio* models which proves useful in the study of novel systems with little reference data. The optB88 functional is based on the non-local Van der Waals density functional (vdW-DF) developed by Dion *et al.*[193]. Specifically, optB88 includes new exchange functionals which improve the interaction energies of the original vdW-DF formalism[194] and show reasonable structure and vibrational properties for liquid water[195]. Each class of models and methods has its own set of strengths and weaknesses which will provide valuable insight when studying the local dynamics and correlations of a system through the VHF. Up to this point, the VHF of water analyzed through molecular simulations has been limited to CMD using the widely used rigid, point-charge models. Iwashita *et al.* reported the VHF of water from the SPC/E, TIP3P_EW, TIP4P_EW, and TIP5P_EW models[165]. The VHF observed by SPC/E was later reported and further analyzed by Shinohara *et al.*[167,196] Camisasca *et al.* reported the VHF of the TIP4P water model to study the local dynamics of water in high-density and low-density environments[197]. Shinohara *et al.* additionally reported the VHF of aqueous solutions through IXS and the use of the MD

simulations and the SPC/E model, demonstrating how the pairwise components of the VHF obtained from MD aid in the understanding of separate atomic correlations [162]. Despite some quantitative differences, each of these studies reported reasonable qualitative agreement for these rigid, point-charge models. To the best of our knowledge, the VHF of water has yet to be studied through reactive, polarizable, and QM methods. Once the VHFs of water models are discussed, analysis of aqueous electrolytes through the VHF is explored. The total VHF of these electrolytes is characterized through IXS and CMD simulations. Then, the partial VHFs are calculated through CMD. The partial VHFs can be used to analyze in detail specific pairwise interactions in these systems.

4.3 Methods

Table 4.1: System Information for computational methods. N_intervals is defined as the number of 2 ps intervals averaged to obtain the final VHF result.

Model	Simulation Method	Number of Molecules	Cell Volume (nm^3)	Simulation Time (ns)	N_intervals
SPC/E	Classical MD	1000	29.98	2	3000
TIP3P_EW	Classical MD	1000	30.01	2	3000
BK3	Classical MD	1000	29.98	2	3000
CHON-2017_weak	Reactive MD	512	15.31	2	10000
3obw	DFTB MD	250	7.49	2	15000
optB88	*Ab initio* MD	128	3.83	0.1	10000

4.3.1 Water

Outlined below are the simulation parameters and steps for each computational method. To maintain consistency among the computational methods, each simulation was run in the canonical (*NVT*) ensemble of constant temperature, number of molecules, and volume. Because the methods investigated span multiple time and length scales, the system sizes and simulation times are different depending on the method. An overview of the system size and simulation times are shown in Table 4.1.

4.3.1.1 CMD

Three classical water models were employed in this study: SPC/E, TIP3P_EW, and BK3. SPC/E and TIP3P_EW are both non-polarizable, 3-site, point charge models which utilize 12-6 LJ potentials to describe non-bonded interactions. Both SPC/E and TIP3P_EW are the most widely used water models due to their relative accuracy and computational efficiency. In contrast, BK3 attempts to model polarizability through the use of drude oscillators. Like the GCPM model that precedes it, BK3 utilizes Buckingham non-bonded potentials and gaussian charge distributions instead of point charges. Both GCPM and BK3 have shown to accurately predict various properties of water over a wide range of conditions.[79,80].

The CMD simulations were set up through the use of the molecular simulation and design framework[198,199] (MoSDeF), comprised of `mBuild`[96,97] and `foyer`[98–100]. Using `mBuild`, water molecules were initialized and placed into a cubic simulation at random positions with the use of `PACKMOL`[119]. Once each box of water was initialized, parametrization was handled using two different routines. For the BK3 polarizable water model, the GROMACS parameter files written by Sega *et al.*[200] were used for defining the system's potentials. For the TIP3P_EW and SPC/E water models, the specific atom-types defining the system were automatically applied through the use of `foyer`.

The non-polarizable simulations were performed with GROMACS 2018.5[121–125]. In these simulations, electrostatics were handled with the particle mesh Ewald[126] method with a real-space cutoff of 0.9 nm, and a minimum grid spacing of 0.12 nm in the inverse space. A cutoff of 0.9 nm was also used for the non-bonded Van der Waals interactions. Temperature was controlled with the Nosé-Hoover[201,202] thermostat at 300 K, and pressure was controlled with the Parrinello-Rahman barostat at 1 bar. All angles and bonds were constrained with the LINCS algorithm[128], and a 1 fs timestep was used. Each system was first equilibrated in the *NPT* ensemble for 1 ns, equilibrated in the *NVT* ensemble for 100 ps, and then sampled in the *NVT* ensemble for 2 ns. During the sampling

run, configurations were written out every 10 fs. The BK3 polarizable simulations were performed with a modified version of GROMACS 4 by Kiss *et al.*[203], which supports gaussian charge distributions and drude oscillators. For these specific MD simulations, the electrostatics were handled with particle mesh Ewald method with a real-space cutoff of 1.1 nm and a minimum grid spacing of 0.12 nm in the inverse space. Non-bonded Van der Waals interactions were also cutoff at 1.1 nm. Temperature was controlled at 300 K with the nose-hoover thermostat, and pressure was controlled at 1 bar with the Parrinello-rahman barostat. A 1 fs timestep was used for all simulations. To equilibrate the system, a 1 ns *NPT* simulation was run, followed by 100 ps *NVT* simulation. Following, a 2 ns *NVT* sampling run was performed, writing configurations every 10 fs.

4.3.1.2 Reactive MD

The ReaxFF simulations were performed by Weiwei Zhang and Adri van Duin of Pennsylvania State University. The ReaxFF reactive force field is a bond-order-dependent force field which can describe the bond formation and breaking during chemical reactions[184]. As such, the connectivity between every pair of atoms should be updated at every MD time step. The ReaxFF potential is expressed as[204]:

$$E_{system} = E_{bond} + E_{angle} + E_{tors} + E_{over} + E_{vdw} + E_{coul} + E_{specific} \tag{4.1}$$

where E_{bond}, E_{angle}, E_{tors}, and E_{over}, are bond, angle, dihedral contributions and an energy penalty preventing the over-coordination of atoms, respectively. All four of these terms are bond-order dependent. The dispersive and electrostatic contributions between atoms, E_{vdw} and E_{coul}, are bond-order independent. $E_{specific}$ represents specific terms generally not included. In this case, a hydrogen bonding term is added for bulk water.
In this work, we used the CHON-2017_weak ReaxFF force field to simulate bulk water, which has been demonstrated to predict density, structural, and dynamical properties of water[185,205]. During our simulation, a cubic simulation box containing 512 water

molecules with a low density (i.e. 0.2 $g\,cm^{-3}$) was first built using Monte Carlo techniques. Then, the system was minimized and compressed to a density of 1.00 $g\,cm^{-3}$. Finally, a 2.5 ns NVT/MD simulation was run at room temperature using the ADF simulation package[206] with the last 1.5 ns of the trajectory data used for analysis. In our ReaxFF MD simulations, the time step was set to 0.25 fs and the Berendsen thermostat was employed with a damping constant of 100 fs.

4.3.1.3 Density-Functional Tight-Binding

DFTB simulations were performed by Van Quan Vuong of the University of Tennessee. DFTB is an approximation to DFT in which its energy is based on a Taylor expansion of DFT energy $E[\rho]$ around a reference electron density ρ^0 with respect to a difference electron density[207]. Here, the third-order DFTB3 method is used as it is the superior method for modeling covalent and noncovalent interactions[208]. The 3obw parameter set,[190] which was specifically tuned for studying water and hydration effects, was employed to simulate bulk water. The empirical γ-damping hydrogen-bond correction and D3(BJ) dispersion correction were included to improve description of noncovalent interactions. An NVT MD simulation of 250 water molecules in a a cubic simulation box with a density of 0.997 $g\,cm^{-3}$ was carried out at room temperature. The temperature was controled by the Nose-Hoover thermostat and timestep of 0.5 fs were used. The system was equilibrated for 100 ps and following a 2 ns sampling run for production, configurations were collected every 10 fs.

4.3.1.4 *Ab initio* MD

AIMD simulations were performed by Paul Kent of ORNL. Simulations were performed with the use of the optB88 vdW-DF which yields reasonable structure and vibrational properties for liquid water. In addition to a production run at a temperature of 300 K, a simulation was performed at 330 K. This is a well-known temperature correction for this model to obtain less-structured liquid water systems. Additional simulation details are

outlined in Ref. 163.

4.3.1.5 Inelastic X-ray Scattering

The experimental VHF of water was obtained by carrying out the double Fourier transformation of the dynamic structure factor $S(Q,\omega)$. $S(Q,\omega)$ was measured with inelastic x-ray scattering at BL43LXU, SPring-8 (Japan)[209]. The details of experimental and data reduction procedure are described in the previous studies[165,167,210]. The sample thickness was 1 mm and the energy resolution function was estimated by using the $S(Q,\omega)$ of borosilicate glass of 1 mm thick. The sample temperature was kept at 303 K.

4.3.2 Aqueous Electrolytes

4.3.2.1 CMD

The MD simulations were carried out with 1500 water molecules and 40 ion pairs. The simulation was initialized and atom-typed with the molecular simulation and design frame-work (MoSDeF) suite of tools. The SPC/E force field[82] and the monovalent ion parameters of Joung and Cheatham[211] were used to describe the water interactions and the ion interactions, respectively. All simulations were run with GROMACS 2018.5.[121–125] The VHFs for each system were computed as the weighted sum of individual partial VHFs. To compare these correlations with the X-ray results, these are scaled by a coefficient $c_\alpha c_\beta f_\alpha f_\beta$. Here, the x-ray form factor f_α was approximated as atomic numbers.

4.3.2.2 IXS

The experimental VHF of water was obtained by carrying out the double Fourier transformation of the dynamic structure factor $S(Q,\omega)$. $S(Q,\omega)$ was measured with inelastic x-ray scattering at BL43LXU, SPring-8 (Japan)[209]. The details of experimental and data reduction procedure are described in the previous studies[165,167,210]. The sample

thickness was 1 mm and the energy resolution function was estimated by using the $S(Q,\omega)$ of borosilicate glass of 1 mm thick. The sample temperature was kept at 303 K.

4.3.3 Analysis

The VHF[212] for a monatomic fluid is defined as

$$G(r,t) = \frac{1}{4\pi\rho N r^2} \sum_{i,j} \delta(r - |r_i(0) - r_j(t)|) \tag{4.2}$$

where ρ is the average number density of particles, N is the number of particles in the system, $r_j(t)$ is the position of the jth particle at time t, and $\delta(R)$ is Dirac's delta function. For fluids containing polyatomic molecules, the total VHF is defined as a weighted sum of the specific pairwise components of the VHF, which we will refer to as the partial VHF

$$G_{\alpha\beta}(r,t) = \frac{V}{4\pi N_\alpha N_\beta r^2} \sum_{i\in\{\alpha\}} \sum_{i\in\{\beta\}} \delta(r - |r_i(0) - r_j(t)|) \tag{4.3}$$

where α is the atoms of species $\{\alpha\}$ and N_α is the number of atoms of species $\{\alpha\}$. To measure $G(r,t)$ in a scattering experiment on a polyatomic fluid, whether pure or part of a mixture, the measured VHF is given by

$$G(r,t) = \sum_{\alpha=1}^{N_\alpha} \sum_{\beta=1}^{N_\beta} x_\alpha x_\beta \bar{b}_\alpha \bar{b}_\beta G_{\alpha\beta}(r,t) \tag{4.4}$$

In Eq. 4.4, x_α is the mole fraction of total atoms that are of type α and $\bar{b}_\alpha$ is the atomic scattering density for an atom of type α. For x-ray scattering, for example, $\bar{b}_\alpha$ is proportional to the number of electrons in atom α, so that the higher the mass of an atom the higher the $\bar{b}_\alpha$. Experimentally, $G(r,t)$ is obtained by double Fourier inversion of the directly measured dynamic structure function $S(Q,\omega)$ with respect to Q and ω, where Q is the momentum transfer and $E = \hbar\omega$ is the energy transfer in scattering. All simulation trajectories were analyzed with the use of the `scattering` package[213]. The

`scattering` package is made freely available and distributed under the MIT license on GitHub and contains a set of Python functions to perform structure analyses on molecular simulation trajectories, including the VHF. This package utilizes MDTraj[120] to calculate the distance of two atoms as a function of time. The total VHFs were calculated from oxygen-oxygen, oxygen-hydrogen, and hydrogen-hydrogen partial VHFs using the weighting factors described by Iwashita *et al.*[165]. Note that due to the weighting factors, the total VHF is dominated by the oxygen-oxygen interactions. Averaging was enhanced by calculating $G(r,t)$ in 2 ps intervals at random starting points through each trajectory using `NumPy`. The number of averaged intervals is displayed in Table 4.1. Additional details of the VHF calculations are contained in the Appendix.

4.4 Water Results

4.4.1 System Size and Duration Comparison

Before discussing $G(r,t)$, the use of simulations of varying size and length must be validated. Comparison across different system sizes and simulation lengths is necessary because of the computational limitations of more complex methods. For example, it is not reasonable with current hardware to run an AIMD simulation of 512 water molecules for 2 ns, whereas a CMD simulation of this size and duration can be completed in a matter of minutes. System size effects may be strong in smaller simulations, while sampling may be inadequate in shorter simulations. To justify this comparison, simulations of SPC/E water of varying size and duration were compared. System size effects are investigated in Fig. 4.1a which displays the height of the first peak as a function of time, $G_1(t)$, for simulations of SPC/E water of varying size. All system sizes display good agreement up to ~0.55 ps. Up to ~0.35 ps, the agreement is nearly perfect while small differences are seen beyond this time, which could partly be due to greater noise as t increases. It is concluded here that no significant system size effects are introduced in the smaller systems - 128 water molecules is sufficient for this property. Effects due to simulation lengths were then

investigated for a system of 128 water molecules shown in Fig. 4.1b. Similar to the system size comparison, the simulations run at various lengths show good agreement, albeit with greater noise at higher t. Because $G(r,t)$ is nearly identical at all simulation lengths, the validity of comparing simulations with different system sizes and durations is confirmed. This is an important finding, since it demonstrates that AIMD simulation can be used to compute $G(r,t)$ with acceptable accuracy despite the small system sizes and trajectory lengths accessible to AIMD methods compared to the computationally cheaper models.

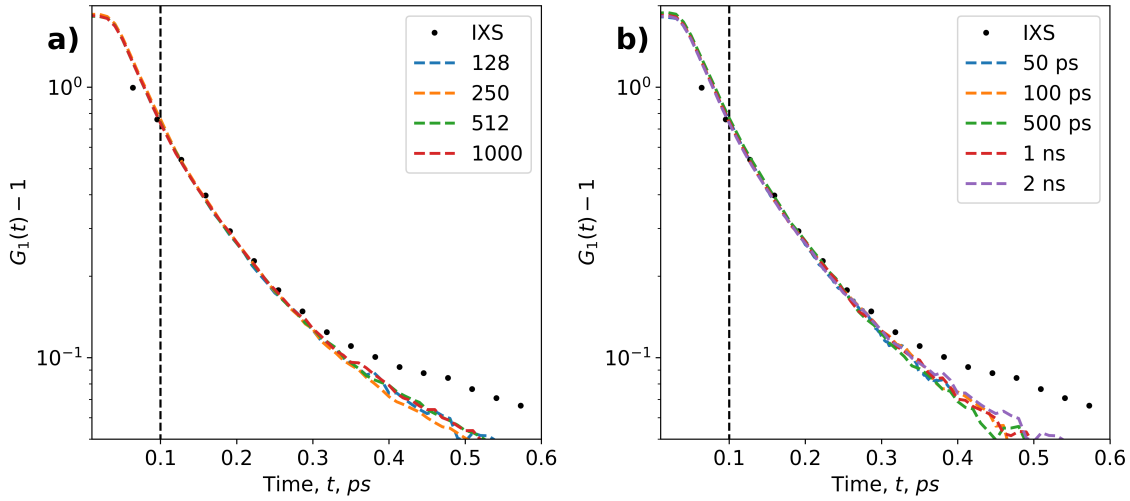

Figure 4.1: Comparison of the first peak height as a function of time, $G_1(t)$, for SPC/E water simulation of a) varying size sampled for 2 ns and b) varying lengths of time with a system size of 128 SPC/E water molecules. Each system has been averaged over 10,000 ps intervals.

4.4.2 Analysis of the Total Van Hove function

The total Van Hove functions, $G(r,t)$, for the IXS data and each molecular simulation are shown in Fig. 4.2a. The total $G(r,t)$ is defined as the weighted sum of the pairwise (partial) $G(r,t)$ for the oxygen-oxygen, oxygen-hydrogen, and hydrogen-hydrogen pairs, as described by Eq. 4.4. $G(r,t)$ comprises of a self-part that represents the correlations of a single atom at time t, and the distinct-part that represents the collective motions of distinct atom pairs. $G(r,0)$ directly corresponds to the weighted pair distribution function (PDF) of water. The first peak of $G(r,0)$ for each curve is roughly located at 0.28 nm and the

second peak is located at 0.4 - 0.5 nm, which is consistent with previous work[165]. Additionally, each curve evolves towards unity with increasing time.

$G(r,t)$ observed from the various models show qualitative agreement with the result from IXS, with the exception of the optB88 AIMD model at 300 K. While the positions of the peaks match those of IXS, the system is over structured as shown by the distinct first and second peaks that remain after 2 ps. This is further shown in the heatmap, Fig. 4.2b, where the water molecules are in distinct first and second peaks. While none of our models explicitly include nuclear quantum effects (NQE), all of the empirically fit models must compensate for the NQE present in the experimental data. Previous studies show optB88 yields better agreement for both PDFs and for self-diffusion at increased temperatures of $+30$ K[195]. With this temperature correction, the optB88 model at 330 K shows much better agreement with the IXS result. While this temperature correction can account for multiple sources of error in the DFT simulations, we expect that the majority of this error is due to the missing NQE. (Use of the path integral approach that would account for the quantum nuclear degrees of freedom[214–216] and resultant NQE is beyond the scope of the present work.).

Several quantitative differences exist across the models. The first minimum around ~0.20 ps displays a higher magnitude in the models, particularly in TIP3P_EW and 3obw. Further, the self-part of $G(r,t)$ decays at a faster rate with time in TIP3P_EW and 3obw, and decays at a slower rate in BK3 and optB88. Discrepancies between the second peak around ~0.45 nm, $G_2(t)$, are also observed in the heatmaps. $G(r,t)-1$ from IXS is roughly 0.1 up to 1 ps. In contrast, $G_2(0)$ produced from TIP3P_EW and 3obw results in lower magnitudes at all times. The magnitude of the second peak produced by SPC/E is also lower at higher t, though it is closer in agreement with IXS. BK3 and CHON-2017_weak appear to show the best agreement with IXS in regards to $G_2(t)$, mainly due to the correct magnitude of $G_2(0)$. At 330 K, the magnitude $G_2(t)$ of optB88 remains too high in comparison with the IXS response. The behavior of $G_2(t)$ is further

investigated below.

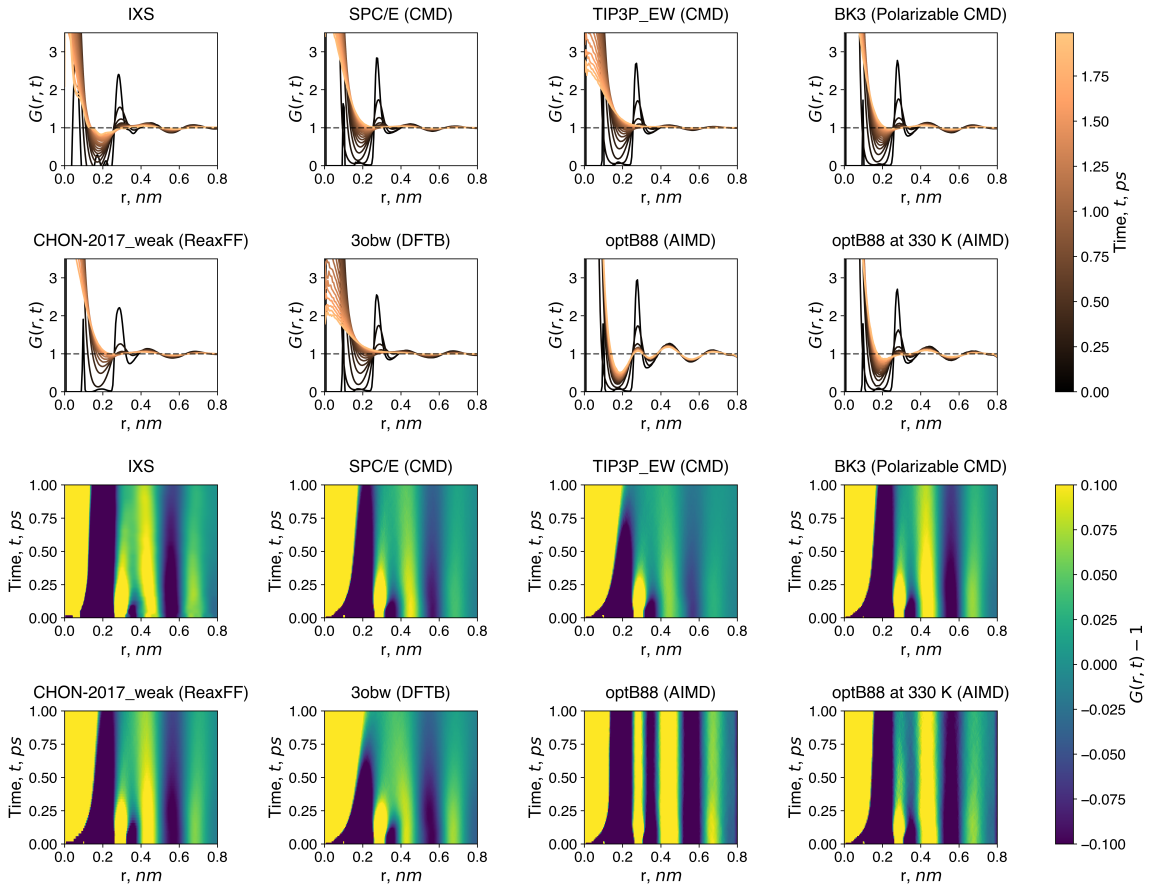

Figure 4.2: (a) Total Van Hove function, $G(r,t)$, measured from x-ray scattering and calculated from molecular simulations. Colorbar represents the time in picoseconds. (b) Heatmap of Van Hove function, $G(r,t)-1$, colorbar represents intensity from -0.1 to 0.1.

4.4.3 Decay of First Peak

The height, $G_1(t)$, and area under the curve, $A(t)$, of the first peak as a function of time are shown in Fig. 4.3a,b. A vertical line at 0.1 ps is drawn to show that the IXS data at shorter times contains termination effects and should not be meaningfully compared to the simulation data as a result[165]. The definition of the peak area is taken from Ref. 167, which is:

$$A(t) = \int_{R_1^i}^{R_1^{ii}} [G(r,t) - 1]\, dr \tag{4.5}$$

where $G(r,t) > 1$ and $R_1^i < r < R_1^{ii}$ around R_1. R_1 is defined as the distance corresponding to the first peak, $G_1(t)$, R_1^i is the local minima left of R_1, and R_1^{ii} is the local minima right of R_1. The first peak height at $t = 0$, $G_1(0)$, corresponds to the first peak of a static PDF, and slightly differs for each model. $G_1(0)$ show the following trend: optB88 > SPC/E > BK3 > 3obw > ReaxFF. These values agree with previous studies comparing static PDFs from experimental and simulation data[87,157,181,185,190]

$G_1(t)$ when $t \leq 0.2$ ps is believed to correspond to the ballistic or phononic motions of water molecules and represents the first-step decay of the first peak. The simulation data up to this time is in good agreement with IXS, suggesting that each model accurately captures the ballistic motion of water. When $t > 0.2$ ps, the CMD, ReaxFF, and DFTB methods begin to overestimate the rate of decay. In contrast, the optB88 model at 300 K decays much slower than the IXS data, consistent with the increased structuring observed in Fig. 4.2. Similar trends are observed in the calculation of $A(t)$. $A(t)$ at $t \leq 0.28$ ps can be fit to a compressed exponential function taken from Ref. 167:

$$A(t) = A_1 e^{(-t/\tau_1)^{\gamma_1}} + A_2 e^{(-t/\tau_2)^{\gamma_2}} \tag{4.6}$$

where τ_1 and τ_2 represent the relaxation times of the first-step and second-step decay. $A(0)$ is roughly consistent across all models and IXS indicating that local coordination of water molecules at $t = 0.0$ is consistent. The fitting results are displayed in Table 4.2 and the compressed exponential equations plotted as a function of time are contained in the Appendix. The values of IXS and SPC/E are in good agreement with the values originally reported in Ref. 167. τ_1 from 3obw shows the best agreement with IXS with a value of 0.153 ps. The values of τ_1 SPC/E, TIP3P_EW, BK3 and CHON-2017_weak are slightly lower than IXS, while τ_1 from optB88 at 300 K and 330 K are the lowest at 0.125 ps and 0.122 ps respectively. As a whole, each model shows sufficient agreement with IXS in regards to τ_1.

The largest differences between the methods are observed in the second-step of $A(t)$. This step describes the configurational changes in the bond network, and τ_2 corresponds to the time required to break a hydrogen bond. The fit from IXS produces a value of 0.475 ps for τ_2. SPC/E, BK3, TIP3P_EW, 3obw, and CHON-2017_weak display a faster rate of decay at these times shown by lower values of τ_2. At 300 K, optB88 displays a much slower change in $G_1(t)$ as indicated by $\tau_2 = 1.53$ ps. Interestingly, optB88 at 330 K shows the best agreement with IXS with a value of $\tau_2 = 0.449$ ps, and suggests that the DFT is potentially capturing interactions at this timescale more accurately than the empirically fit models.

An interesting characteristic of $G_1(t)$ produced from the simulations occurs at $t < 0.1$ ps. Because of termination effects in the IXS data previously mentioned, the behavior of water dynamics at $t < 0.1$ ps is relatively unknown. All simulation methods however display a shoulder in the first peak decay, which corresponds to the first neighbor shell staying intact for times less than 0.1 ps before the motion of water occurs. The shoulder can be explained by the time reversal symmetry of the VHF:

$$G(r,t) = \frac{1}{4\pi\rho N r^2} \sum_{i,j} \delta(r - |r_i(0) - r_j(t)|) \tag{4.7}$$

$$= \frac{1}{4\pi\rho N r^2} \sum_{i,j} \delta(r - |r_i(-t) - r_j(0)|) \tag{4.8}$$

$$= \frac{1}{4\pi\rho N r^2} \sum_{i,j} \delta(r - |r_i(0) - r_j(-t)|) \tag{4.9}$$

which results in:

$$\frac{dG(r,t)}{dt}\Big|_{t=0} = 0 \tag{4.10}$$

This equation produces a shoulder and can be modeled by the Debye model for phonons.

The first peak decay at these times less than 0.1 ps should be further investigated as this may allow for a better understanding of the local dynamics of water.

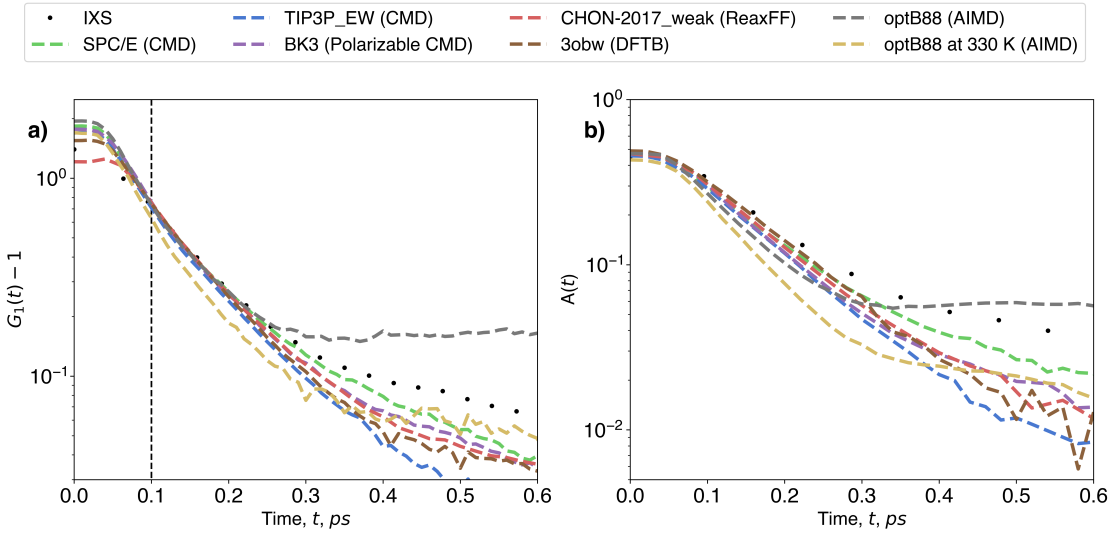

Figure 4.3: a) Height of first peak, $G_1(t)$ and b) $A(t)$ as a function of time measured from x-ray scattering and calculated from simulation methods.

Table 4.2: Fitting results of the first peak area for the first-step decay, $A(t)$, of the Van Hove function. Simulation method displayed in parentheses.

Model	A_1	τ_1	γ_1	A_2	τ_2	γ_2
IXS	0.330	0.153	2.119	0.128	0.475	1.360
SPC/E (CMD)	0.343	0.132	1.831	0.140	0.347	1.274
TIP3P_EW (CMD)	0.310	0.131	1.915	0.155	0.264	1.478
BK3 (Polarizable CMD)	0.378	0.134	1.946	0.114	0.336	1.334
CHON-2017_weak (ReaxFF)	0.343	0.138	1.960	0.136	0.314	1.451
3obw (DFTB)	0.436	0.153	1.646	0.067	0.415	1.399
optB88 (AIMD)	0.428	0.125	1.916	0.059	1.532	3.848
optB88 at 330 K (AIMD)	0.380	0.122	2.022	0.062	0.449	1.401

4.4.4 Decay of Second Peak

The height of the second peak, $G_2(t)$ is compared and shown in Fig. 4.4a. $G_2(0)$ produced from the simulations display different heights of the second peak, which has been documented by previous studies[83,87,180]. As reported originally by Shinohara *et al.*[167], $G_2(t)$ for all methods show a more gradual decay compared to $G_1(t)$, suggesting a

prominent role of the second neighbor shell on water dynamics. To account for the differences at $t = 0$, the height of the second peak as a function of time has also been normalized through min-max scaling, displayed in Fig. 4.4b. The simulation methods produce a qualitative agreement with IXS in regards to $G_2(t)$, which decreases as a function of time. However, $G_2(t)$ computed from the simulations decays at a faster rate than the result computed from IXS, similar to the first peak. Revisiting the heatmaps shown in Fig. 4.2b, TIP3P_EW and 3obw initially appeared to show poor agreement with IXS in regards to $G_2(t)$. Looking at the normalized result, however, this largely results from lower values of $G_2(0)$ as the decay of $G_2(t)$ is comparable to SPC/E, TIP3P, CHON-2017_weak, and BK3. Similarly, BK3 and CHON-2017_weak originally appeared to show the highest agreement with $G_2(t)$ produced from IXS, although this is mainly due to the agreement at $t = 0.0$. The optB88 model at 300 K displays the greatest differences from the IXS result, where $G_2(t)$ decays rapidly up to ~0.5 ps and stays constant afterwards.

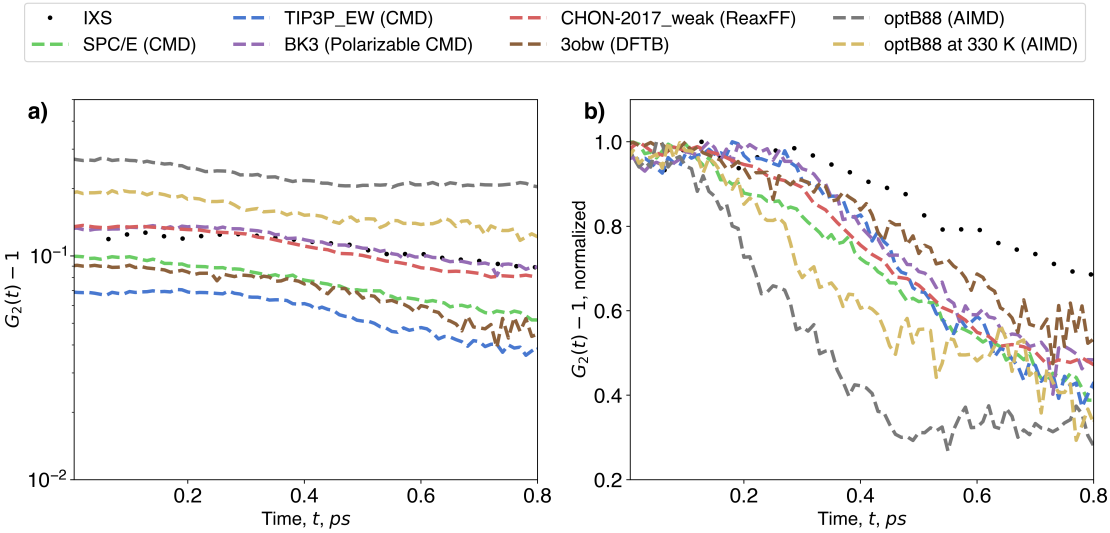

Figure 4.4: a) Height of second peak, $G_2(t)$ and b) normalized height of second peak as a function of time measured from x-ray scattering and calculted from simulation methods.

4.4.5 Analysis of the Partial Van Hove functions

Our simulations allow for the analysis of pairwise elemental components of the total Van Hove function, which we refer to as the partial Van Hove function. In the case of pure water, the oxygen-oxygen correlations are dominant in the total Van Hove function. Regardless, it is worth investigating the oxygen-hydrogen and hydrogen-hydrogen correlations for each model. The oxygen-oxygen, oxygen-hydrogen, and hydrogen-hydrogen Van Hove functions are presented in Fig. 4.5, Fig. 4.7, and Fig. 4.6 respectively. Additionally, $G_{\mathrm{OH}}(r,t)$ focusing on the first hydrogen bond peak ($G_{\mathrm{OH_1}}(t)$) is shown in Fig. 4.8. The decay of the first hydrogen bond peak, $G_{\mathrm{OH_1}}(t)$ is shown in Fig. 4.9a. Due to the different heights at $t = 0$, the normalized decay is also shown in Fig. 4.9b. Generally, the models are in good agreement regarding the decay of this peak as shown by normalization. CHON-2017_weak shows the slowest decay of the hydrogen bond peak which could possibly be attributed to the inclusion of the hydrogen bonding term in the energetic interactions. The decay of the first hydrogen-hydrogen peaks, $G_{\mathrm{HH_1}}(t)$ is shown in Fig. 4.9c,d. The normalization of $G_{\mathrm{HH_1}}(t) - 1$ indicates the correlated dynamics of the hydrogen atoms is similar for all models studied. As a result, discrepancies of $G(r,t)$ between the models seem to largely originate from the oxygen-oxygen correlations. This may provide further justification for models that do not define non-bonded interactions for the hydrogen atoms, at least in the context of pure, bulk water. AIMD models that explicitly account for NQE, as well as path-integral methods, should be pursued to investigate the differences of the oxygen-hydrogen correlations with the models studied here.

4.4.6 Comparison of Simulation Models

The results of $G(r,t)$ and how they relate to the details of each model will be discussed. The SPC/E model was parametrized to experimental values of density and potential energy, resulting in a reasonable static structure and self-diffusion coefficient. Despite

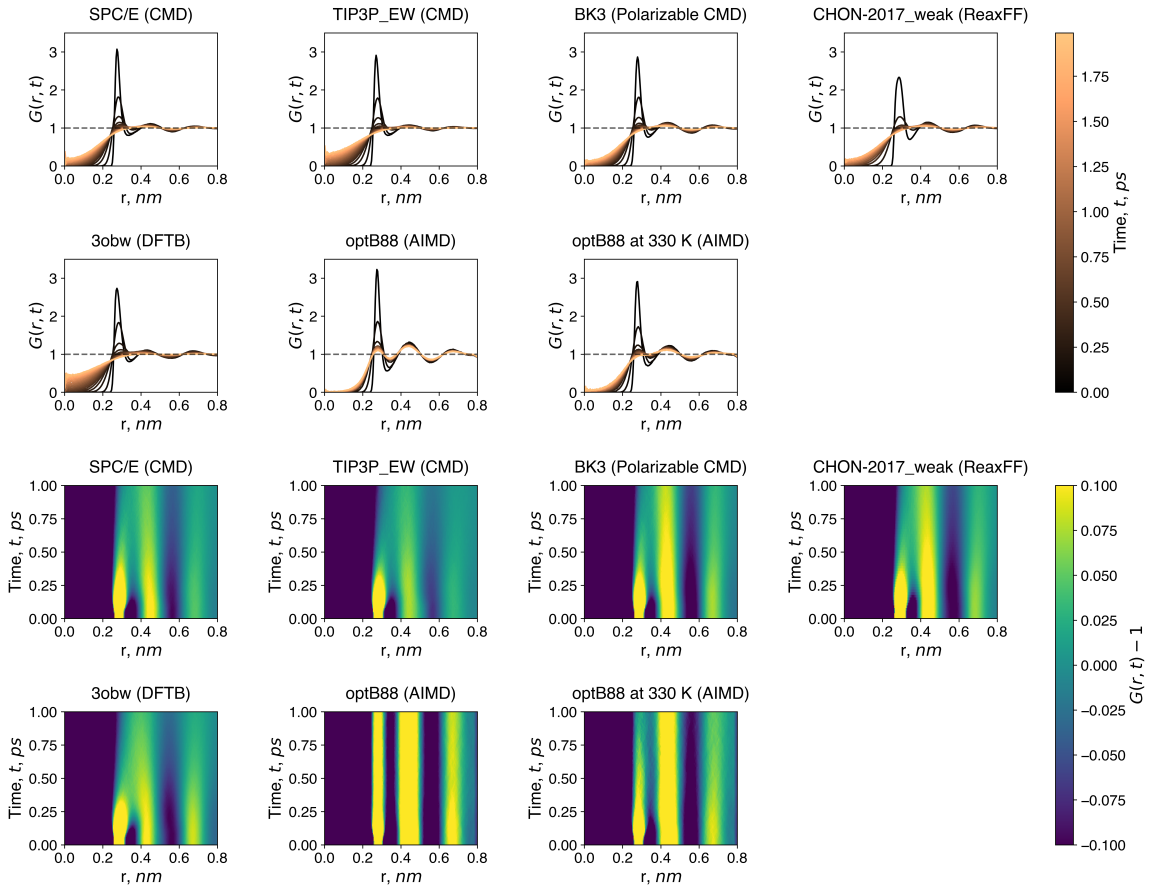

Figure 4.5: Oxygen-oxygen partial Van Hove function, $G_{OO}(r,t)$, for all simulation methods. The top panels shows the one-dimensional slice at $0 < t < 2$ ps, the bottom panels show the heat map of $G_{OO}(r,t) - 1$.

being a classical, three-site model, SPC/E shows relatively good agreement of $G_1(t)$ with IXS in regards to τ_1 and τ_2. TIP3P_EW is a modified version of the original The non-bonded parameters were chosen to reproduce the density and heats of vaporization from experiments. The self-diffusion coefficient is overestimated, which could explain why the value of τ_2 and decaying rate of the self-part of $G(r,t)$ show large deviations from IXS. Though 3obw includes additional parameters that account for QM effects, this model suffers from similar issues to TIP3P_EW. The potential interaction between the oxygen and hydrogen of water have been tuned to the experimental oxygen-hydrogen $G(r)$ through iterative Boltzmann inversion. This leads to remarkable agreement with $G(r,0)$ with IXS, but overestimated dynamics at longer times and in the self-part. The

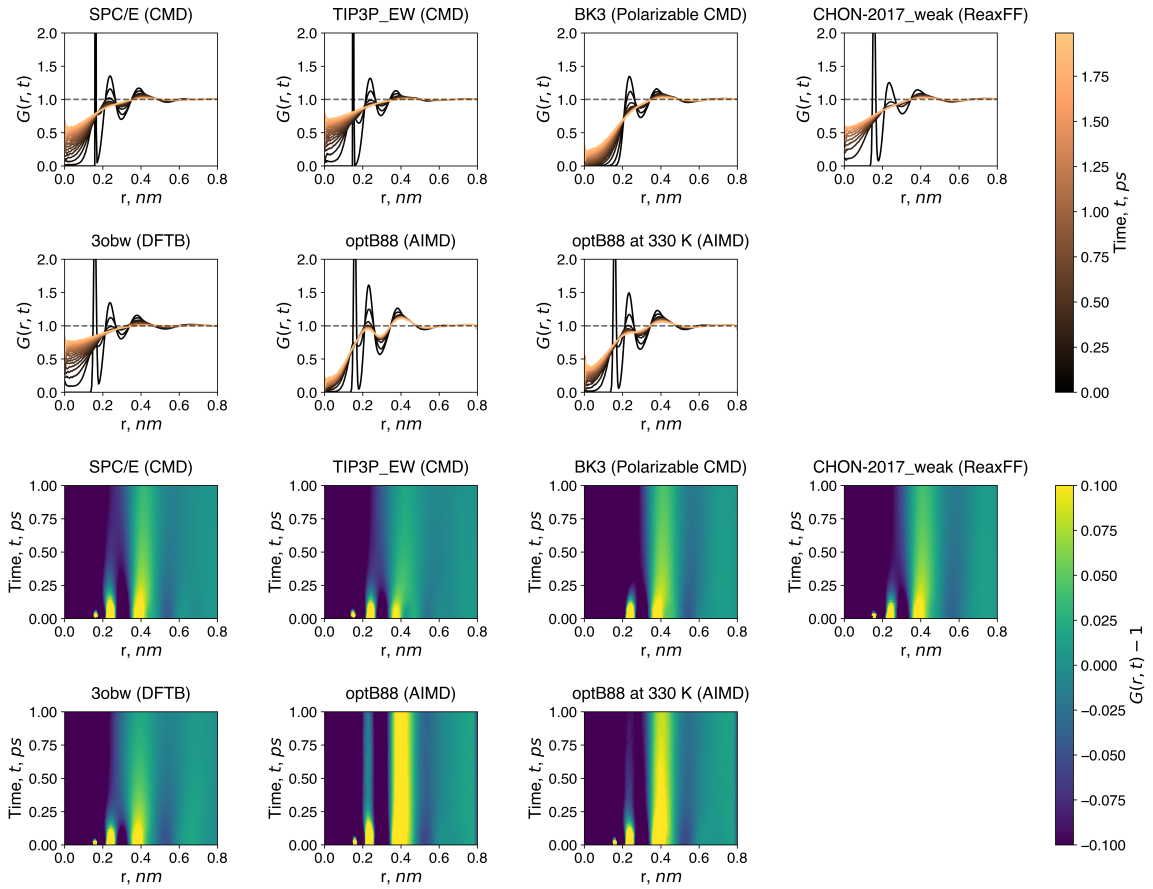

Figure 4.6: Hydrogen-hydrogen partial Van Hove function, $G_{\mathrm{HH}}(r,t)$, for all simulation methods. The top panels shows the one-dimensional slice at $0 < t < 2$ ps, the bottom panels show the heat map of $G_{\mathrm{HH}}(r,t) - 1$.

GCPM-derived BK3 model includes additional terms over SPC/E and TIP3P_EW as Drude-oscillators are used to model polarizability, a Buckingham repulsive potential is used in place of a Lennard-Jones repulsive potential, a fourth site is added, and Gaussian charges are used instead of point charges. At 300 K and 1 bar, these additional terms don't appear to have a significant effect on the agreement with IXS, as the decay of $G_1(t)$ and $G_2(t)$ is similar to the classical methods. The CHON-2017_weak ReaxFF model includes additional terms over the classical models that account for hydrogen bonding and coordination with other atoms. This model produces remarkable agreement of $G(r,0)$ to IXS but also overestimates the rate of decay similar to the classical models. The optB88 *ab initio* model is unique as it is the only non-empirical model studied here, allowing these

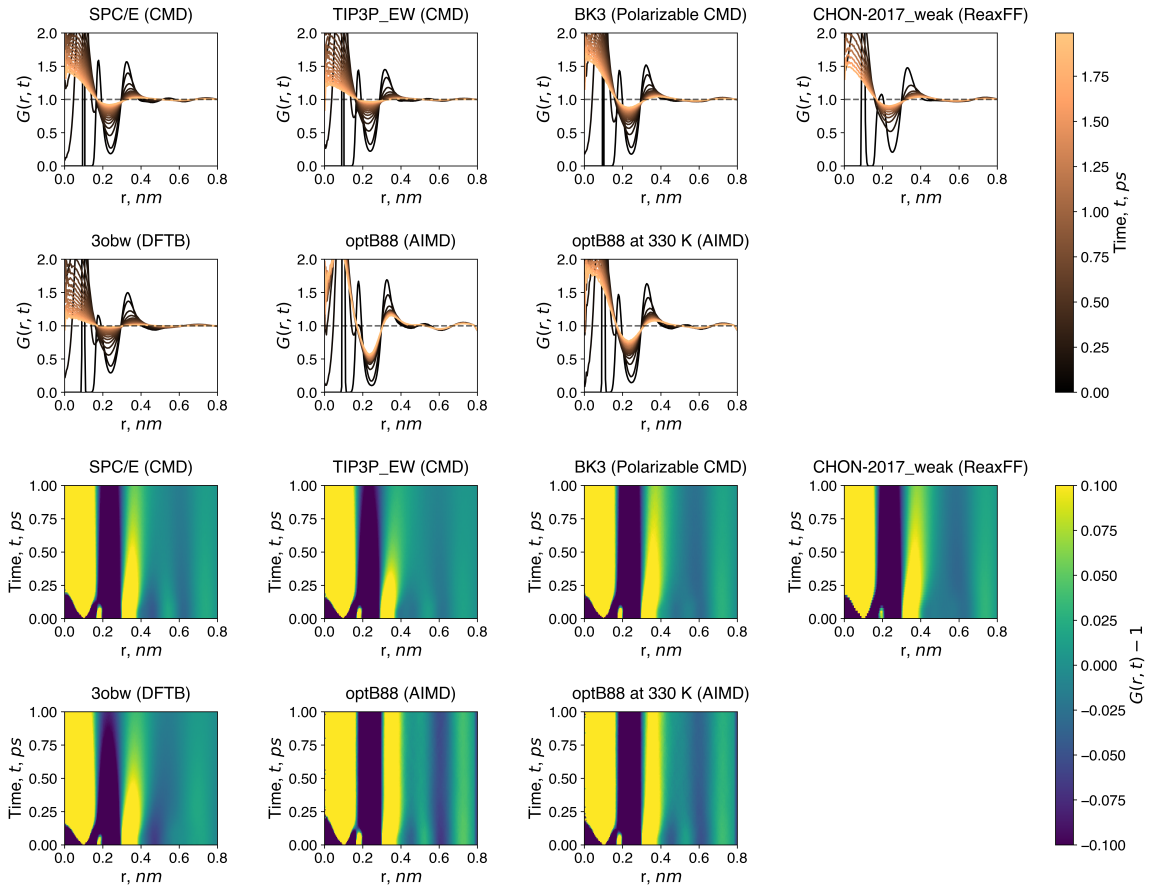

Figure 4.7: Oxygen-hydrogen partial Van Hove function, $G_{\mathrm{OH}}(r,t)$, for all simulation methods. The top panels shows the one-dimensional slice at $0 < t < 2$ ps, the bottom panels show the heat map of $G_{\mathrm{OH}}(r,t) - 1$.

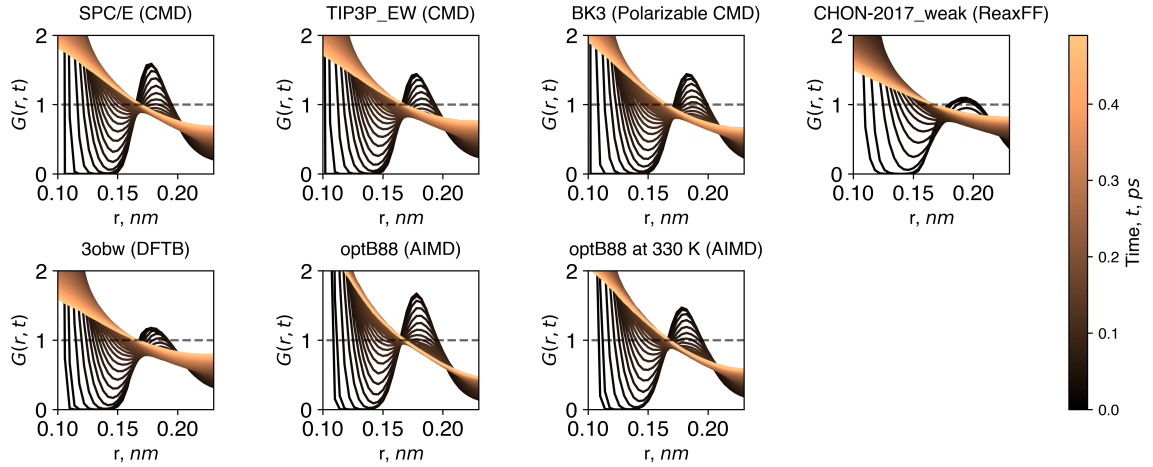

Figure 4.8: Oxygen-hydrogen partial Van Hove function, $G_{\mathrm{OH}}(r,t)$, highlighting the first hydrogen bond peak around 0.18 nm.

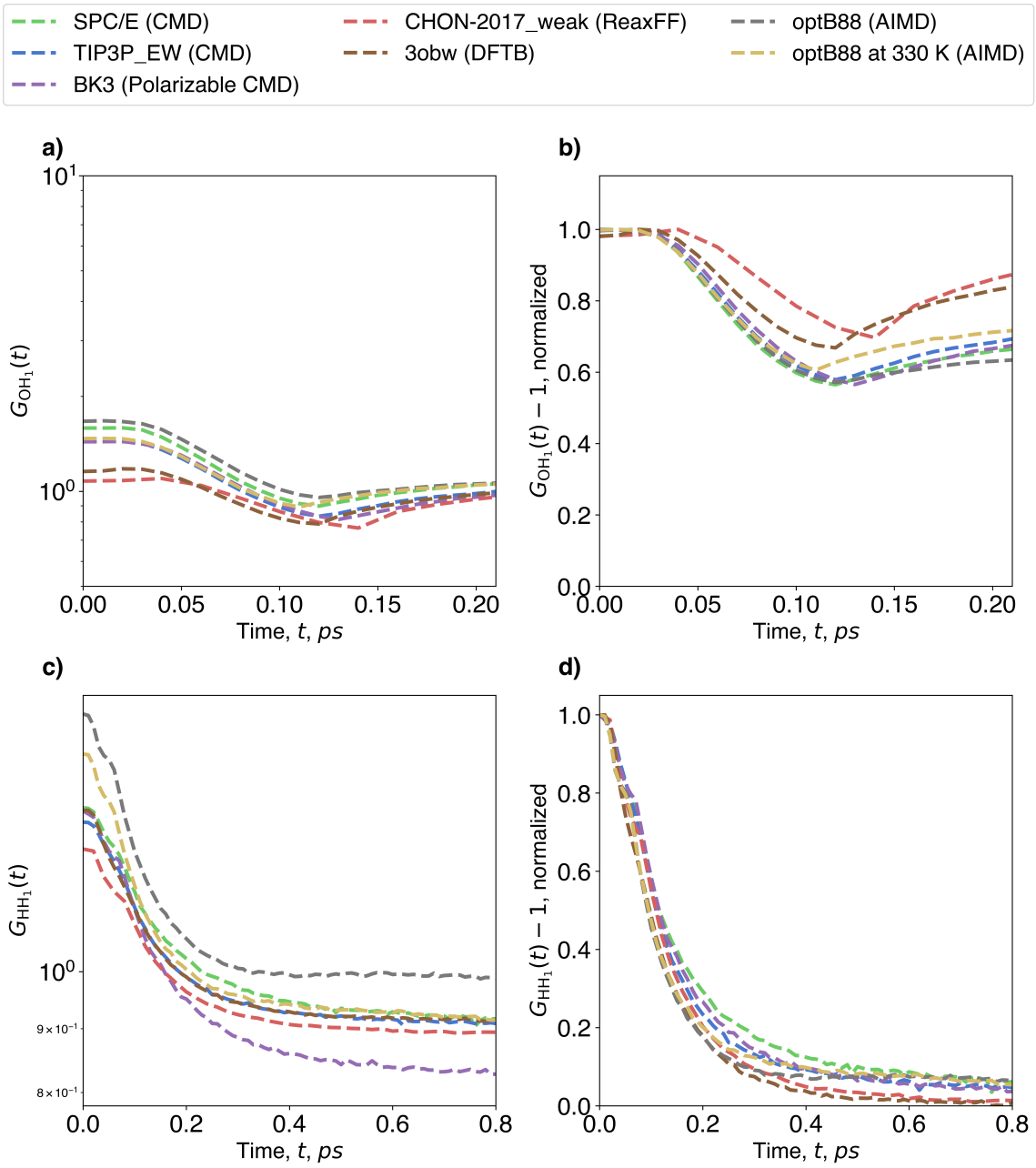

Figure 4.9: a) Height of first hydrogen bond peak of oxygen-hydrogen Van Hove function $G_{\mathrm{OH}_1}(t)$, b) Normalized height of first hydrogen bond peak of oxygen-hydrogen Van Hove function, $G_{\mathrm{OH}_1}(t) - 1$ c) height of first peak of hydrogen-hydrogen Van Hove function $G_{\mathrm{HH}_1}(t)$ and d) normalized height of first peak of hydrogen-hydrogen Van Hove function $G_{\mathrm{HH}_1}(t) - 1$ for all simulation methods. Normalization is performed through min-max scaling.

systems to be unbiased to a given state. Most notably, the second-step decay of $G_1(t)$ is much slower in comparison with IXS as indicated by $\tau_2 = 1.36$ ps. Running at an elevated

temperature of 330 K improves the agreement, as τ_2 is much closer to the value of IXS. Shinohara *et al.* previously discussed the shortcomings of CMD models, namely the lack of QM calculations to accurately describe the intermolecular fluctuations and hydrogen bond lifetimes. Specifically, the degree of freedom for the tunneling action of protons has to be treated at the same level as the electronic degree of freedom. This is because a hydrogen bond is characterized by proton tunneling strongly coupled to electronic fluctuation. Because density functional theory assumes electrons are in the ground state, DFTB and *ab initio* models are expected to be insufficient at describing this behavior. The results of $G(r,t)$ from 3obw and optB88 corroborate this idea based on the quantitative differences from IXS. Morrone and Car previously demonstrated how incorporation of NQE through path-integral AIMD simulations improves the structure of water over AIMD simulations with classical nuclei[217]. New *ab initio* models that explicitly incorporate NQE, as well as path-integral MD simulations, should be investigated to determine if these methods improve the agreement to IXS.

It is worth nothing that the improved accuracy of $G(r,t)$ through added complexity is not fully investigated in this study. SPC/E and TIP3P_EW perform well at room temperature but we expect deviation from the experimental response at different conditions. More complex models, such as BK3 and optB88 may show improved agreement with experiment over these models over a wider range of conditions. Further, the inert systems of bulk water do not fully take advantage of the bond order terms included in ReaxFF to model chemical reactions. QM methods may be more appropriate in modeling complex systems containing water, as additional effects are intrinsically modeled[186,187]. Moreover, QM methods are more suitable for systems in which atomic interaction parameters do not yet exist[187]. Overall, improved performance should be expected over the classical, 3-site models when studying water at different conditions, and more complex systems such as confined water.

4.5 Aqueous Electrolytes Results

In this section, the VHF results of aqueous electrolytes are discussed. The VHFs have been measured through IXS and calcaluted from CMD. While the intrinsic broad width of correlation functions of liquids makes it difficult to separate each individual water-ion correlation *a priori*, the water-ion correlations can be identified when the partial VHFs show a peak at a distance that is different from the water-water correlation as clearly seen in the aqueous solutions of NaBr and NaI. Similar to the previous section looking at pure water, the use of MD simulation allows us to identify the element-specific correlated motions through the VHF. This work demonstrates the capability of the VHF to study aqueous electrolytes, which will be effective for determining the molecular-level mechanisms of water dynamics in the presence of salts.

4.5.1 Total VHFs of Aqueous Electrolytes

The VHFs of pure water and aqueous electrolytes (NaCl, NaBr, NaI) with the molality m = 1.5 $\mathrm{mol\,kg^{-1}}$ determined from IXS (upper two panels) and MD (lower two panels) are shown in Fig. 4.10. Regardless of the salt, the first peak is found at 0.28 nm which corresponds to the nearest oxygen-oxygen correlations. With the addition of salt, that first peak decreases at $t = 0$. Another peak appears at larger R for the NaBr and NaI electrolytes, and a shoulder appears for NaCl. The positions of these peaks and shoulder, 0.321 nm, 0.336 nm, and 0.360 nm for the NaCl, NaBr, and NaI electrolytes, respectively, correspond to the sum of the ionic radii of individual particles such as Cl^-, Br^-, and I^- and O^{2-}. When $t > 0.5$ ps, the addition of salt induces a qualitative change in the first and second neighbor peaks. At these times, the peak intensity from the water-anion peak is much higher than that of the water-water peak. These results demonstrate that the correlations between various pairwise components can be clearly identified based on the ionic radii and distance R of the corresponding peak.

The third-neighbor peak around 0.68 nm shows little change with the addition of salt,

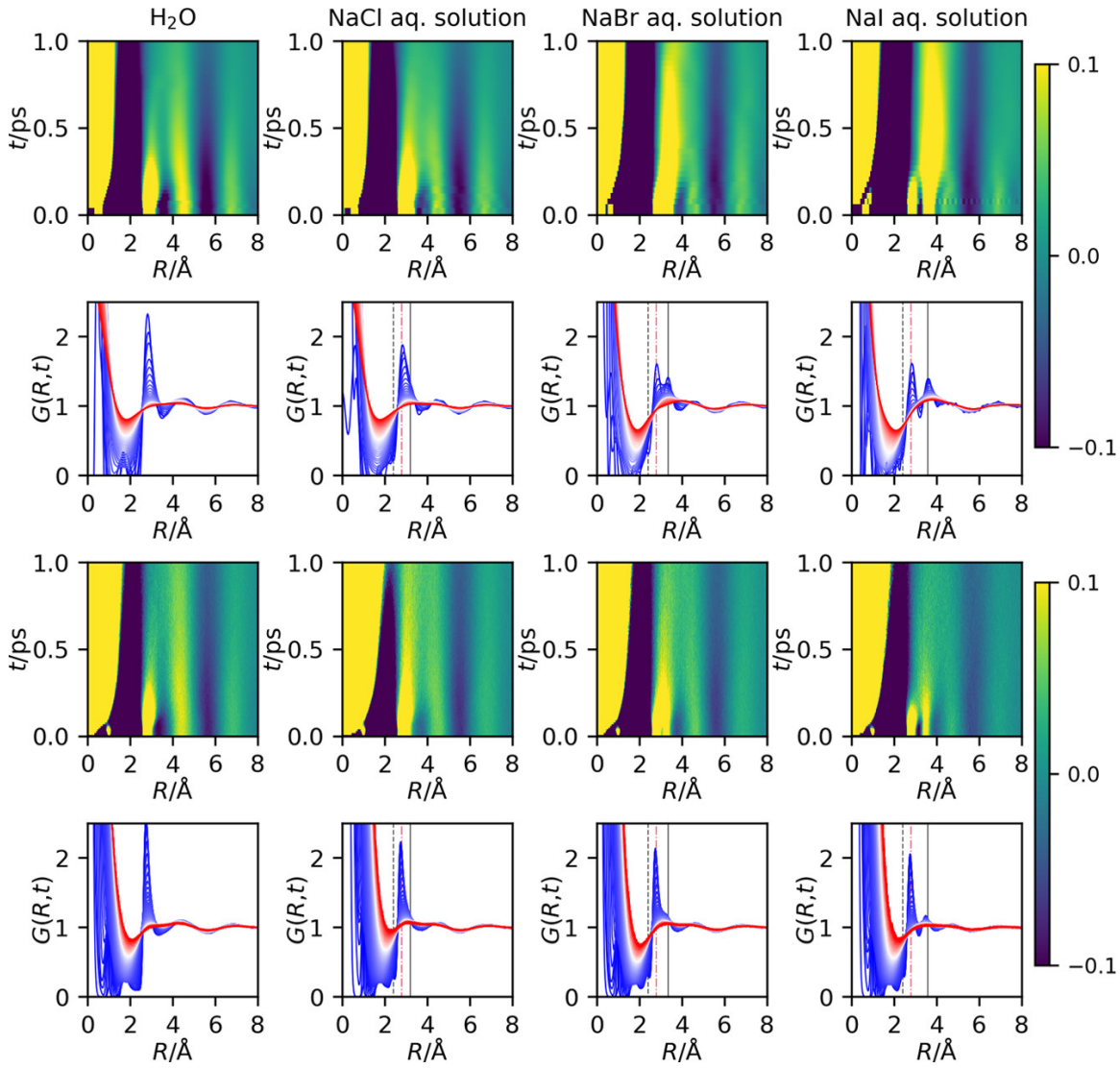

Figure 4.10: VHFs, $G(r,t)$, of pure water and aqueous electrolytes of NaCl, NaBr, and NaI with m = 1.5 mol kg^{-1}, measured from IXS measurements (first and second rows) and calculated from MD simulations (third and fourth rows). From left to right: pure water, aqueous NaCl solution, aqueous NaBr solution, aqueous NaI solution. The panels in the first and third rows show the intensity map of $G(r,t)-1$, the color scales of which are shown on the right. The narrow color scales are used to highlight the small changes and the temporal evolution at a longer time scale. The panels in the second and fourth rows show their one-dimensional slice at $0 < t < 1$ ps (from blue to red). The solid lines, dashed lines, and dashed-dotted lines in the figures in the second and fourth rows represent $R = R_{O^{2-}} + R_A$, $R = R_{O^{2-}} + R_C$, and $R = 2R_{O^{2-}}$, respectively, where $R_{O^{2-}}$, R_C, and R_A are the effective ionic radii of oxygen, the cation, and anion, respectively. Figure taken from Ref. 162.

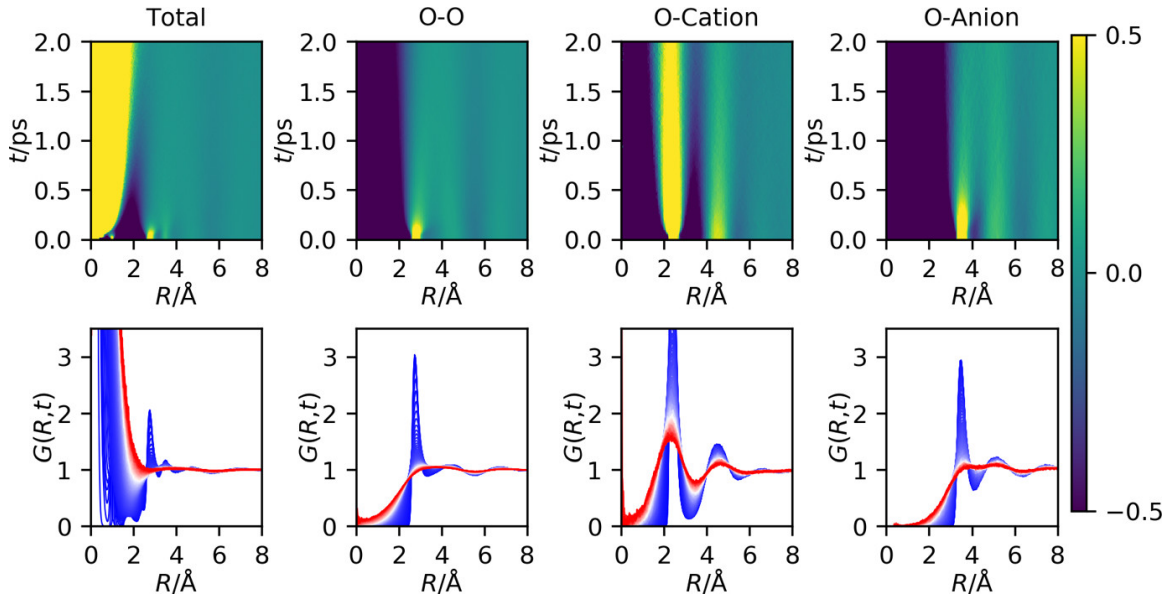

Figure 4.11: Partial VHFs, $G_{\alpha\beta}(R,t)$, of aqueous NaI with m = 1.5 mol kg^{-1}, calculated from the molecular trajectories obtained by the MD simulation. From left to right: total VHF including the self-correlations, oxygenoxygen correlation, oxygencation (Na^+) correlation, and oxygen anion (I) correlation. The top panels show the intensity map of $G(r,t)1$, the color scale of which is shown on the right. The bottom panels $\alpha\beta$ show their one-dimensional slice at $0 < t < 2$ps (from blue to red). Figure taken from Ref. 162.

indicating that the dynamics of these solutions is similar at longer distances. It should be noted that the higher-order peaks of the VHF correspond to multiple molecule-molecule correlations[218], and as a result, the decay time of the higher-order peaks is not directly comparable to the first-neighbor peak.

the VHFs calculated from CMD are shown in the lower two panels of Fig. 4.10. Though quantitative differences exist with the IXS result, the overall qualitative features are reproduced. That is, the additional peaks (NaBr and NaI) or shoulder (NaCl) exist at the distance corresponding to the sum of ionic radii of O^{2-} and the anion. Mentioned in the previous section, the static PDF, $G(r)$, is a common benchmark for molecular simulations of soft matter, but does not account for correlated dynamics. The VHF results of aqueous electrolytes again demonstrate that the VHF is a more rigorous method of analysis over the static PDF.

4.5.2 Partial VHFs of Aqueous Electrolytes

Similar to what was done for pure water, the element-specific analyses for the aqueous electrolytes are provided via the partial VHFs, shown in Fig. 4.11. It should be noted that the contributions of the oxygen-ion is small due to the small number of oxygen-ion pairs compared to the number of oxygen-oxygen pairs. Regardless, the oxygen-Na^+ VHF shows that the first-neighbor peak at 0.24 nm is of higher magnitude and exists at a longer timescale compared to the other peaks.

4.5.3 Decaying Behavior of Aqueous Electrolytes

The decaying behaviors of the peaks corresponding to ion correlations, $I_{OA}(t)$ are calculated, similar to the analysis performed for bulk water. The peak decays were calculated in the range of $0 < t < 0.75$ ps by using a two-step relaxation similar to what was used for pure water:

$$I_{\mathrm{OA}}(t) = \alpha_1 exp(-(t/\tau_{A1})^2) + \alpha_2 exp(-t/\tau_{A2}) \tag{4.11}$$

where $\tau_{A1} < \tau_{A2}$. The results are shown in Fig. 4.12. The first term represents the ballistic motion of the anions caged by surrounding water molecules. The differences of this term across the three solutions is attributed to the differences in interactions between the anion and water molecules. The second term is attributed to the decay of correlation between the water molecules and anions. The decaying behavior of the second term is similar regardless of anion selection, which suggests the molecular connectivity between water and anions is independent of anion type. Fig. 4.12D displays a relationship between τ_{A1} and the square root of the atomic weight of the anion, $\sqrt{M_{anion}}$.

The second term represents the anion translating away from the first-neighbor shell of water, which dominates the decaying behavior of the oxygen-anion peak. The differences of this term are much smaller between the various aqueous electrolytes, suggesting this motion is less dependent on the type of anion.

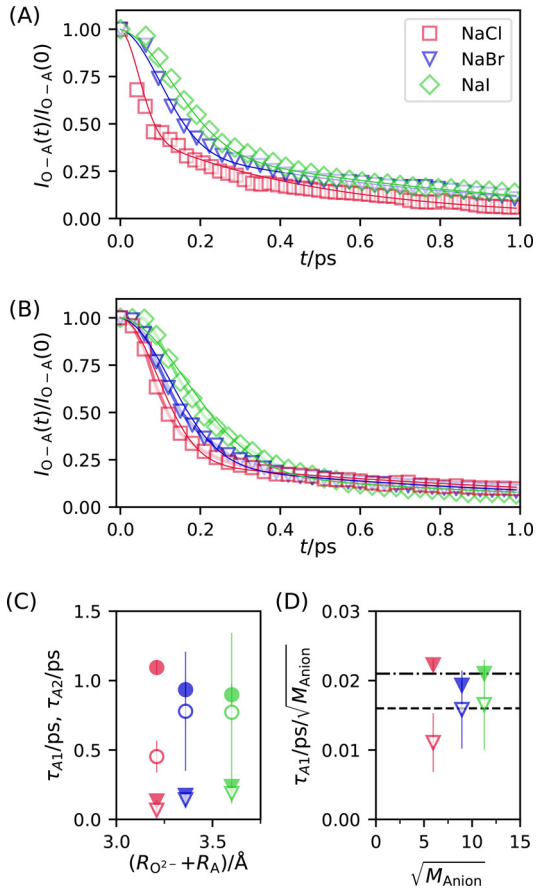

Figure 4.12: (a,b) Normalized decaying behavior of the peak height at around the water-anion peak, $I_{OA}(t)/I_{OA}(0)$, determined from a) the IXS and b) the MD simulation: aqueous solutions of (squares) NaCl, (triangles) NaBr, and (diamonds) NaI. The solid lines show the results of fitting (see main text). c) Results of fitting: (triangles) τ_{A1} and (circles) τ_{A2}. Closed symbols correspond to the MD results and open symbols to the IXS results. d) Relationship between τ_{A1} and $\sqrt{M_{anion}}$. The error bars correspond to two standard errors of the mean. Figure taken from Ref. 162.

4.6 Conclusion

In this chapter, various water models were analyzed through the calculation of the VHF. While applying a well-known temperature correction for optB88, each model showed qualitative agreement with $G(r,t)$ computed from IXS, displaying a two-step decay of the first peak and similar behavior of the second peak. Quantitative differences with IXS were identified, namely in the second-step decay of the first peak, $G_1(t)$, and $A(t)$, as well as in the overestimation of the decay of the second peak, $G_2(t)$. In general, all models show good agreement with IXS at $t = 0$, but deviate at longer times. optB88 was the only non-empirical model studied here and showed the most quantitative differences from the results of the other models and IXS data as a result. Overall, each of these models studied reproduces the experimental response well enough to further investigate the local correlations of aqueous systems in future studies.

Next, the correlated dynamics of aqueous electrolytes were studied through both IXS and CMD simulations. Through the calculation of the total VHF, specific correlations could be identified based on the distance of the peaks and ionic radii. Further, calculation of the partial VHFs through CMD allows for confirmation and further analysis of the individual pairwise correlations of these electrolytes. The methods outlined allow for further study of various electrolytes.

Overall, the VHF is a powerful method to analyze the correlated dynamics of electrolytes for energy storage applications. By gaining a deeper understanding of the connection between particle dynamics and macroscopic properties, we hope to design more optimal electrolytes.

4.7 Future Work

There are many possible avenues for research regarding the VHF. The next step in terms of bulk systems is to study more complex electrolytes. Water is a relatively simple fluid to study through the VHF as there are only three pairwise correlations to consider:

oxygen-oxygen, oxygen-hydrogen, and hydrogen-hydrogen. Aqueous electrolytes are slightly more complex, with the consideration of cation and anion correlations. However, consideration of a different solvent, such as acetonitrile, adds a great amount of complexity to the interpretation of the VHF. Not only are there additional atoms, but there are duplicate elements (carbon atoms) on a single acetonitrile molecule to consider. These complications are exponentially increased when considering ionic liquids. Our collaborators at ORNL have recently performed IXS experiments on mixtures of $[EMIM^+][Tf_2N^-]$ and acetonitrile. Perhaps more so than in the case of aqueous electrolytes, molecular simulation will be a useful technique alongside IXS in analyzing these systems. For example, if we were to analyze the correlations between the terminal carbon of the $EMIM^+$ cation and the nitrogen on acetonitrile, the terminal carbon could be uniquely named in the input files to separate it from the other carbon atoms in the system with relative ease.

The VHF analysis should also be extended to confined fluids. Our collaborators, Yuya Shinohara and Takeshi Egami, are beginning to calculate the VHF of water and MXenes. Using a flexible MXene model, the correlations between the MXene atoms and water can be investigated through CMD. To investigate the confinement effects on water alone, a simpler approach may also be to calculate the 2-D VHF of water while keeping the MXene atoms rigid. Here, the area of a circle is considered rather than the volume of a sphere. There is still much to be understood regarding the properties of fluids used for energy storage applications. The analysis of the VHF provides an exciting avenue of research to better understand these properties and ultimately design more efficient electrolytes for energy storage.

CHAPTER 5

Properties of Electrolytes Under MXene Confinement

5.1 Introduction

MXenes are a class of 2D transitional metal carbides and/or carbonitrides[65,71,75]. The name originates from the MAX phases[65,71], in which M refers to an early transition metal (such as Ti or Mo), A is a group 13 or 14 element, and X is carbon and/or nitrogen. To synthesize MXenes, the A phase can be selectively etched away due to the weaker M-A bonds through a chemical etchant such as hydrofluoric acid. The resulting product is a crystalline 2D metal carbide with alternating layers of metal and carbon/nitrogen. Strong covalent bonds exist between the M and X atoms while hydrogen bonding or van der Waals interactions exist between the sheets[219,220].

Over the past decade, our group and collaborators have primarily studied porous carbons as electrode materials for supercapacitors[64,169]. These materials generally induce charge storage through the formation of an EDLC, which exhibit volumetric capacitances up to 300 $\mathrm{F\,cm^{-3}}$[221,222]. Ghidiu *et al.* reported MXene supercapacitor electrodes in H_2SO_4 reporting up to 900 $\mathrm{F\,cm^{-3}}$[73]. Due to a flexible interlayer, many ions of differing size and chemistry can be inserted into MXenes, resulting in vastly different behavior between the electrolyte and MXene surface chemistries[220]. As a result, MXenes have exhibited various charge storage mechanisms which must be understood to design more efficient energy storage devices. Lukatskaya *et al.* reported the intercalation of several cations in Ti_3C_2 MXene layers in which the resulting cyclic voltammetry (CV) curves were mostly rectangular, indicating capacitive behavior[74]. Hu *et al.* studied the charge storage mechanisms of Ti_3C_2 MXenes in H_2SO_4, $(NH_4)_2SO_4$, $MgSO_4$[223]. Through CV curves and Raman spectroscopy, it was demonstrated that the system containing H_2SO_4 exhibited pseudocapacitive behavior while the other two electrolytes formed EDLCs.

Since the first report of MXenes in 2011, research on these materials has significantly increased[224]. Not only is vast research being conducted to understand their charge storage mechanisms, but new classes of MXenes are still being discovered and synthesized[69,225]. Simulation is being utilized alongside experiments to better understand the properties of these materials[226,227]. Due to the novelty of MXenes, they are well-suited to be studied with *Ab initio* MD simulations as no empirical interaction parameters are required. However, simulations through CMD do require interaction parameters fitted to experimental data or DFT, which has been a challenge for studying MXenes. In this chapter, the process of implementing MXene force field parameters from Lukas Vlceck into MoSDeF is described[156]. Then, CMD simulations of tetraalkylammonium (AA), and 1-Ethyl-3-methylimidazolium bis(trifluoromethylsulfonyl)imide ($[EMIM^+][Tf_2N^-]$) in $Ti_3C_2OH_2$ MXenes are discussed. This work is currently under preparation for submission.

5.2 Background

Because MXenes are a relatively new material, a limited number of CMD studies involving MXenes have been published to date. The mechanical properties of MXenes have been studied with MD[228], and the effect of metal ion intercalation on the structure of MXenes have been studied with ReaxFF[54]. Ghidiu *et al.* studied the intercalation of AA ions in $Ti_3C_2OH_2$ MXenes with DFT and CMD using the universal force field[229]. Although the universal force field yields acceptable properties of MXenes, the next step is the development of force field parameters tailored for the material.

Our collaborator, Lukas Vlceck at ORNL, recently developed a MXene force field based on target data from *Ab initio* MD performed by Yu Xie of ORNL. This force field was first used in the work of Wang *et al.* in which the intercalation of organic electrolytes in MXenes was studied[156]. We implemented this model into MoSDeF as a package named `MXenes`. Using `mBuild` and the `Lattice` class, Ti_3C_2 MXenes with varying

functional groups can be constructed in just a few lines of code. The force field parameters and specific pairwise interactions have been implemented into `XML` and `TXT` files and are applied with `foyer`. The resulting chemical systems initialized from `MXenes` have been validated previously in the dissertation of Matthew Thompson[230].
In this chapter, a study of MXene and ionic liquid systems are discussed. As previously discussed in Chapter 3, aqueous electrolytes display high conductivities but limited operational voltage windows. Microporous Ti_3C_2 MXene films with sulfuric acid aqueous electrolytes have shown to deliver up to 210 $F\,g^{-1}$ capacitance at a 10 $V\,s^{-1}$ scan rate[77], but the narrow voltage window limits the energy density. Ionic liquids display much wider voltage windows, although the size of cations is generally much larger than those used in aqueous electrolytes. Thus, the larger size limits the accessibility and dynamics of ions under confinement of MXenes Studies investigating systems of ionic liquids and MXenes show that capacitances are generally lower than those of aqueous electrolytes for this reason[231–233]. Our collaborators, Michael Naguib and Kun Liang of Tulane University, hypothesize that the d-spacing of MXenes can be optimized for specific ions. They tested this hypothesis by studying the effect of d-spacing on the electrochemical performance of MXene electrodes in ionic liquids. To support their findings, MD simulations of systems relevant to the experiments are performed and discussed here. This work is currently submitted and under review[234].

5.3 Methods

The ionic liquid [$EMIM^+$][Tf_2N^-] is studied in the interlayer spacings of Ti_3C_2 MXenes. The MXenes are first intercalated with AA ions to widen the interlayer spacings. In the CMD simulations, dodecyltrimethylammonium (C12) and hexadecyltrimethylammonium (C16) AA cations are studied. Hexyltrimethylammonium (C6), octyltrimethylammonium (C8), decyltrimethylammonium (C10) are also studied in the experiments. Experimental methods are briefly outlined, although further details are discussed in 234.

5.3.1 Classical MD

MD simulations were performed in an attempt to provide a molecular perspective on the experimental findings. All simulated systems were initialized with `mBuild` and were parametrized with `foyer`, a set of Python packages that belong to MoSDeF. $Ti_3C_2OH_2$ MXenes with repeat units of 20x20x1 were constructed with 20 AA cations in each pore. A bulk region of [$EMIM^+$][Tf_2N^-] extending 10 nm away from the MXene sheets was initialized. 65 $EMIM^+$ and Tf_2N^- ions were placed in each pore and 625 $EMIM^+$ and Tf_2N^- ions were placed in the bulk region of the Ti_3C_2-C12 system. 75 $EMIM^+$ and Tf_2N^- ions were placed in each pore and 737 $EMIM^+$ and Tf_2N^- ions were placed in the bulk region of the Ti_3C_2-C16 system. Spacings between the MXene sheets of 1.31 nm and 1.63 nm were used for the Ti_3C_2-C12 and Ti_3C_2-C16 systems, respectively, to match the Δd determined from the XRD data. Details of the interlayer spacing calculation are provided in the Appendix. To account for the net-positive charge due to the alkylammonium cations, the partial charges of the carbon atoms on the MXenes were adjusted to make the overall system electrically neutral. The set of parameters derived by Vlceck[156] were used to parametrize the MXene atoms. The [$EMIM^+$][Tf_2N^-] atoms were modeled by a force field reported by Koddermann *et al.*[153], and the AA atoms were modeled by a force field reported by Tsuzuki *et al.*[235]. Both sets of parameters originate from the OPLS-AA force field, and have been further refined to better reproduce various properties of ionic liquid ions. Thus, all parameters utilize the same functional form for non-bonded and bonded interactions and 1-4 scaling factors. Pair interactions were handled through geometric mixing rules as these are applied for the ion parameters. Simulations were run with GROMACS 2020[121–125]. The MXene atoms were frozen in place, and bonds containing hydrogen atoms were constrained to have fixed bond lengths through the use of the LINCS[128] algorithm. Van der Waals and Coulomb interactions were cutoff at 1.2 nm, and long-range Coulomb interactions were computed with the Fast Smooth Particle-Mesh Ewald method[126]. Additionally, the number of k-space vectors to

compute the long-range Coulomb interactions was set by a Fourier spacing of 0.12 nm. The temperature was controlled with the Bussi thermostat[127] with separate groups for the MXene atoms and ion atoms. Steepest descent energy minimization was first run for 5000 steps to remove any unfavorable interactions due to initial packing. Equilibration was performed in the canonical ensemble (fixed molecule number N, volume V and temperature T) using a 1 fs timestep. During equilibration, the system was first run at a temperature of 303 K for 1 ns. The temperature was then slowly increased to 700 K over the course of 2 ns, in which the system was further equilibrated for 18 ns. The temperature was then slowly cooled to 393 K over 4 ns, and then was further equilibrated at 393 K for 25 ns. Each system was then sampled in the canonical ensemble for 50 ns using a 1 fs timestep. All files to run the simulations are contained within the `mxene_polymer_emim`[236] repository contained on GitHub.

5.3.2 Electrochemical Tests

Electrochemical measurements were performed by Kun Liang of Tulane University. All tests were performed in Swagelok three-electrode T-cells with AA-Ti_3C_2 as the working electrode, activated carbon as the counter electrode, and Ag wire as the reference electrode. Glassy carbon electrodes were used as the current collectors, and glassy fibers were used as separators between the working and counter electrodes. [$EMIM^+$][TF_2N^-] and 1 M [$EMIM^+$][TF_2N^-] in ACN were chosen as electrolytes.

CVs and electrochemical impedance spectroscopy (EIS) tests were performed by Kun Liang of Tulane University. EIS was performed to study the kinetics of the TI_3C_2 electrodes.

5.3.3 X-ray Diffraction

Ex-situ x-ray diffraction (XRD) measurements were conducted by Kun Liang of Tulane University using pristine Ti_3C_2 and Ti_3C_2-C12 free-standing electrodes after fully discharging to -1.8 V vs. the Ag wire and recharging back to 1.0 V vs. the Ag wire. These

measurements were performed to estimate the d-spacing of the MXenes.

5.4 Results

The experimental results are first presented as motivation for the CMD simulations. Afterwards, the results of the CMD simulations are presented.

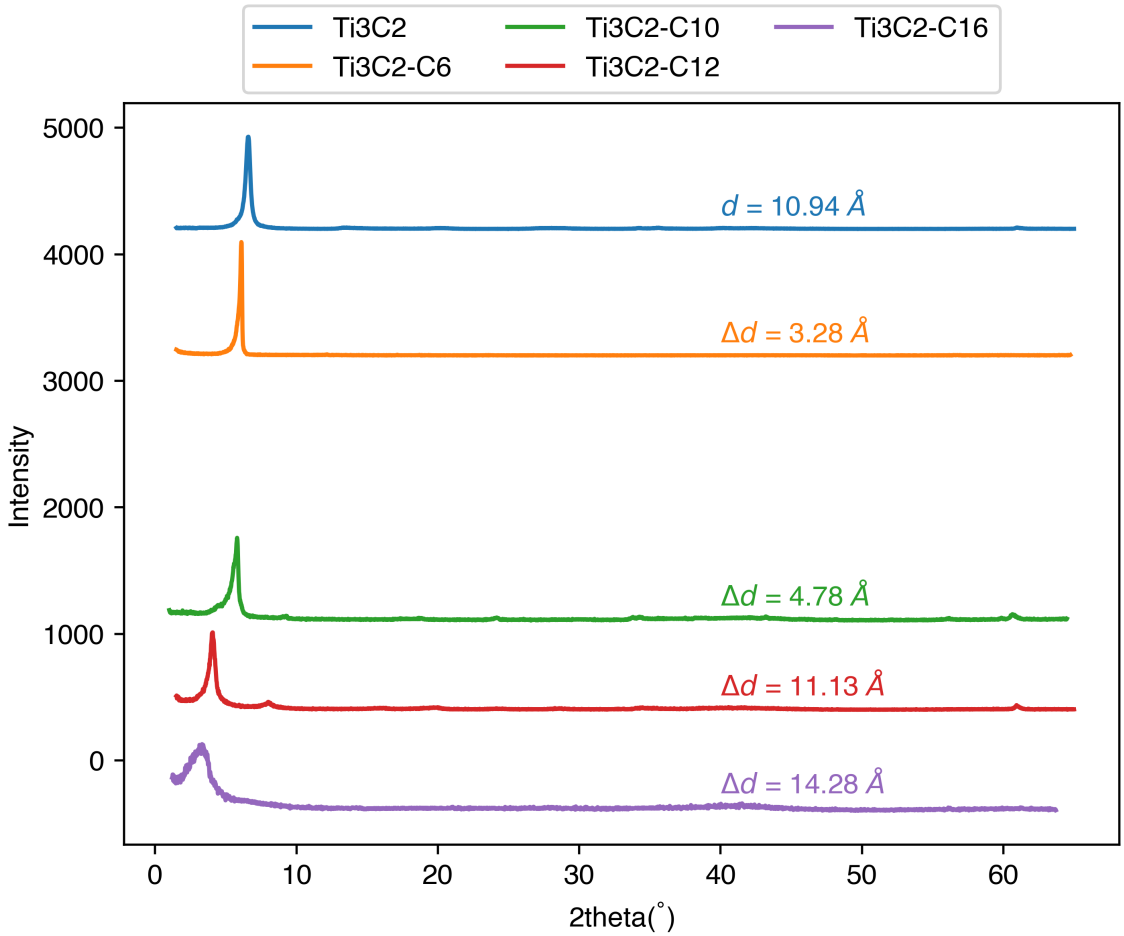

Figure 5.1: XRD curves for systems of AA cations intercalated in Ti_3C_2 electrodes with 1 M $[EMIM^+][TF_2N^-]$ in ACN. Data taken from Ref. 234.

5.4.1 Experimental Results

Fig. 5.1 shows the XRD curves of the Ti_3C_2 MXenes in various electrolytes. As the length of the alkyl chain of the AA cations increase, the 002 peaks shift to lower angles which indicates a larger interlayer spacing. Therefore, addition of AA cations with longer alkyl

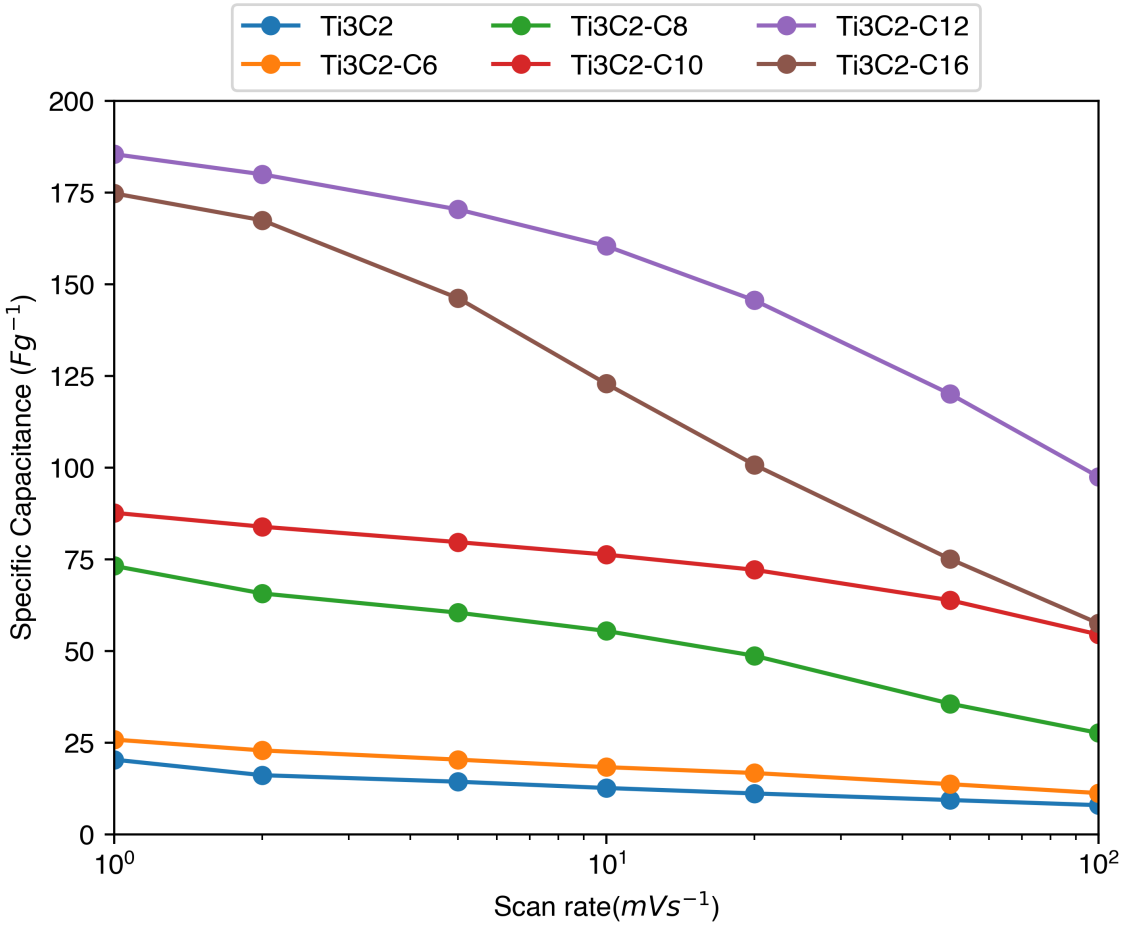

Figure 5.2: Specific Capacitance at different scan rates for systems of AA cations intercalated in Ti_3C_2 electrodes with 1 M [$EMIM^+$][TF_2N^-] in ACN. Data taken from Ref. 234.

chains increase the interlayer spacing.

To investigate the effect of increase interlayer spacing on electrochemical performance, CV curves were conducted with pristine and AA-Ti_3C_2 MXene electrodes. The specific capacitance as a function of scan rate is shown in Fig. 5.2. The Ti_3C_2-C6 MXene only shows a marginal increase in capacitance over the pristine MXene electrode, suggesting the increased interlayer spacing of 0.328 nm is not sufficient to allow for the ions to intercalate. As the alkyl chain length of the AA cation is increased from C8 to C10 to C12, the capacitance dramatically increases. This trend could be explained by wider interlayers for the $EMIM^+$ ions to intercalate. However, when increasing the alkyl chain

length from C12 to C16, a drop in capacitance is observed. The C16 cation could affect the capacitance through longer diffusion pathways, charge-transfer resistances, etc. The explanation for this drop in capacitance from C12 to C16 is the fundamental question to be explored through CMD.

5.4.2 Classical MD Results

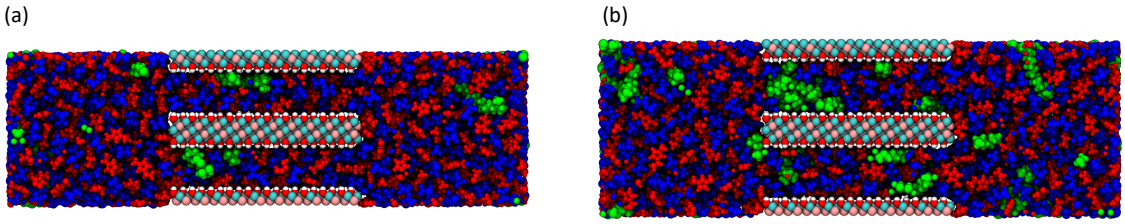

Figure 5.3: Snapshots from MD simulations of (a) Ti3C_2OH_2-C12 (spacing between the sheets of 1.31 nm) and (b) $Ti_3C_2OH_2$-C16 (spacing between the sheets of 1.63 nm) systems displaying AA (green), $EMIM^+$ (red), and Tf_2N^- (blue). MXene atoms include oxygen (red), hydrogen (white), titanium (cyan), and carbon (pink). The simulation is replicated in all three directions via periodic boundary conditions.

To investigate the structure of ions within the MXene interlayers, orientation distribution profiles were calculated through the use of MDAnalysis[237]. Number density profiles of the ions were calculated with MDTraj[120]. Additional details of these calculations are contained in the appendix. Snapshots of the $Ti_3C_2OH_2$-C12 and $Ti_3C_2OH_2$-C16 systems are shown in Fig. 5.3. Note that although the AA ions were initially placed within the interlayer spacing of the MXenes, several AA ions exited during equilibration. Orientation distribution profiles between the normal vector of the MXene walls and vectors drawn for the following groups of atoms are shown in Fig. 5.4a and b: the ring on $EMIM^+$, the ethyl chain on $EMIM^+$, and the alkyl chain on the AA cation (Schematics shown in the appendix). In the interlayers of $Ti_3C_2OH_2$-C12, the rings of $EMIM^+$ display a wide distribution of angles with the surface normal from 30° to 150°. The broad distribution of angles suggests a non-specific orientation of the rings within the interlayers. The alkyl tails of $EMIM^+$ form a distribution of angles with the surface

normal around 0, 90, and 180°, suggesting the tails are both parallel and perpendicular to the walls. The C12 vectors primarily display angles at 90°, with much smaller distributions of angles around 45 and 135°. These angles indicate the C12 ions are mostly parallel with the wall, while sometimes also existing in kinked conformations relative to the walls. The orientation of ions within the $Ti_3C_2OH_2$-C16 interlayers shows clear differences from $Ti_3C_2OH_2$-C12. While the $EMIM^+$ rings show a broad distribution of angles from 30 to 150°, a distribution of angles also exists at 0 and 180° corresponding to the rings laying flat relative to the surface. The alkyl tails of $EMIM^+$ show a similar distribution of angles around 0 and 180°, corresponding to the alkyl chains laying perpendicular to the surface normal. The C16 ions are arranged in three main orientations at 70, 90, and 110°. The broader orientation profiles within $Ti_3C_2OH_2$-C16 are likely due to the wider interlayer spacing.

Number density profiles of the ions inside the pores are shown in Fig. 5.4c and d. In $Ti_3C_2OH_2$-C12, $EMIM^+$ and C12 ions are almost exclusively positioned near the walls, while Tf_2N^- is positioned in two layers in the middle of the pore. Due to the wider interlayer spacing, the structure of ions inside $Ti_3C_2OH_2$-C16 differs from that of $Ti_3C_2OH_2$-C16. While $EMIM^+$ is located near the walls, an additional layer of cations also exists in the middle of the pore. As a result, alternating layers of $EMIM^+$ and Tf_2N^- exist, suggesting increased ordering of the ions in this system. To further investigate the structure of the AA ions inside the pores, the number density profiles of the nitrogen, terminal carbon, and branch carbon atoms of the AA ions are shown in Fig. 5.4g and h. In $Ti_3C_2OH_2$-C12, two distinct layers of branch carbons exist near each pore wall. In the middle of these two layers of branch carbons are peaks corresponding to nitrogen and terminal carbon atoms. This result suggests the C12 ions are mostly arranged in two layers parallel with the wall, with the d-spacing large enough to allow for the alkyl chains to move somewhat freely as indicated by the broader peaks of the terminal carbon atoms. While a similar structure exists near the walls in $Ti_3C_2OH_2$-C16, the C16 atoms also exist

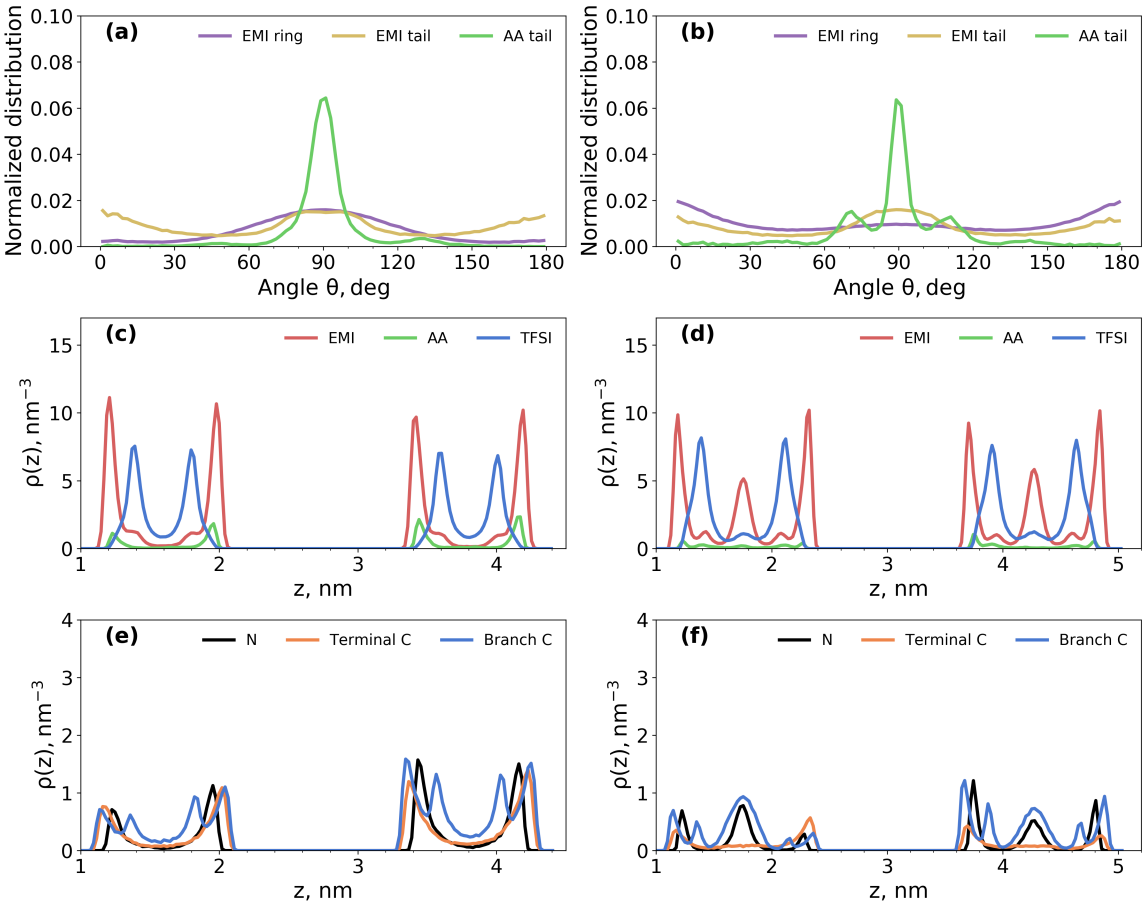

Figure 5.4: Normalized orientation profiles of (a) Ti3C_2OH_2-C12 and (b) $Ti_3C_2OH_2$-C16, number density profiles of $EMIM^+$, AA, and Tf_2N^- in (c) $Ti_3C_2OH_2$-C12 and (d) $Ti_3C_2OH_2$-C16, number density profiles of specific atoms of (e) $Ti_3C_2OH_2$-C12 and (f) $Ti_3C_2OH_2$-C16.

in the middle of the pores. These distributions in the middle of the pore are broader than those near the wall, suggesting more disorder of the C16 ions in this region due to a wider d-spacing and longer alkyl chain length. Because the C16 ions have a higher affinity to stretch across the length of the pore, this may increase the length of the diffusion pathway for $EMIM^+$ ions resulting in slower diffusivity.

In $Ti_3C_2OH_2$-C12, the densities of $EMIM^+$ and Tf_2N^- are 323.2 kg/m^3 and 731.9 kg/m^3, while the densities of $EMIM^+$ and Tf_2N^- in $Ti_3C_2OH_2$-C16 are 360.3 kg/m^3 and 840.5 kg/m^3. This corresponds to 51.1 $EMIM^+$ ions and 45.9 Tf_2N^- ions in each $Ti_3C_2OH_2$-C12 pore and 70.7 $EMIM^+$ ions and 65.4 Tf_2N^- ions in each $Ti_3C_2OH_2$-C16

pore over the course of the sampling simulation. The higher densities in $Ti_3C_2OH_2$-C16 may result in slower dynamics in comparison to the $Ti_3C_2OH_2$-C12 system. However, we cannot make any conclusions about the capacitive performance between the two systems. Nonetheless, there are clear, striking structural differences whose relationship to capacitance and dynamics should be investigated in a subsequent study. Here we speculate based on the structural results. In particular, the density profiles of $EMIM^+$ in $Ti_3C_2OH_2$-C12 (Fig. 5.4e) and $Ti_3C_2OH_2$-C16 (Fig. 5.4f) suggest that the $EMIM^+$ is more structured/ordered in the larger pore, due to the presence of oscillations in the density of $EMIM^+$. By contrast, in the smaller pore, the $EMIM^+$ are present only at the wall, and not in the middle of the pore. This difference in structure provides another possible explanation for the unexpectedly lower diffusivity of $EMIM^+$ in the larger pore.

5.5 Conclusions

In this chapter, the use of force field parameters derived by Vlceck was used to investigate the structure of ions within the interlayer spacings of Ti_3C_2 MXenes. Experimentally, pristine Ti_3C_2 MXenes and Ti_3C_2 MXenes intercalated with AA cations in solutions of 1 M $[EMIM^+][Tf_2N^-]$ in ACN were studied. XRD results revealed that the interlayer spacings increased as the alkyl chain length of the AA cations was increased. From C6 to C12, the increase in interlayer spacing resulted in a greater capacitance. Despite a further increase in interlayer spacing, the C16 cation resulted in a drop in capacitance. This phenomenon was further investigated through CMD simulations. Orientation profiles and number density profiles suggest that increased ordering and density may influence the capacitance of the Ti_3C_2-C16 systems. Further work should be done to better understand the dynamics of the ions within the MXene interlayers. Nevertheless, this work investigates the promising hypothesis that MXene electrodes can be tuned to specific ions for increased performance. Further pursuit of this idea may lead to the development of improved supercapacitors.

5.6 Future Work

Due to the novelty of MXenes and recent research interest, it is safe to say that the work on MXenes has just begun. The research described in this chapter looked at the structural properties of the ions within the MXene interlayers, and the next step is to investigate the dynamic and electrochemical properties. Using the current simulation step in which $Ti_3C_2OH_2$ sheets are exposed to a bulk region of ions, an algorithm should be developed to selectively measure the MSDs of only the ions within the interlayer spacings. With a better understanding of the density of ions within the interlayer, diffusivity measurements could perhaps be simplified by constructing a system in which only the Ti_3C_2 sheets and ions within the interlayer are considered.

Another logical next step is to study these systems with applied external potentials, in order to gain a better understanding of the electrochemical properties. The simplest method in which to model applied potentials in CMD is to apply a fixed uniform charge to an electrode, known as the constant charge method. The limitation of this approach is the failure to take into account local charge fluctuations.[64,238,239]. An alternative approach is to explicitly account for these charge fluctuations through the constant potential method[240]. In the constant potential method, the external potential is fixed by constraining the electric potential on each electrode atom every time step[238] Wang *et al.* conducted a comparison of both methods through simulations of $LiClO_4$ and acetonitrile electrolytes under the confinement of graphite forming an EDLC. The results showed the constant charge method displays good agreement with the constant potential method in regards to number density profiles when the potential difference was less than 2 V. Although the constant potential method should provide more accurate results[241,242], the method is only publicly available through an external library for LAMMPS[243] to the best of our knowledge. Other implementations of the constant potential method are developed in-house and are unavailable to the public. Further, the constant charge method still yields relatively accurate results and is more computationally efficient than the constant potential

method. As a result, it would be beneficial to model MXenes under an applied potential through both methods.

Modeling an applied potential through constant charges for porous carbon is relatively simple, as partial charges can be uniformly applied to the surface atoms. However, MXene surfaces are not homogeneous making it difficult to determine how to apply fixed charges. Because this procedure for MXenes is unclear, it is necessary to develop a process in which to model MXenes through constant charges that yields similar results to the constant potential method.

As previously mentioned in this chapter, aqueous electrolytes have been well-studied with MXene electrodes and have shown to exhibit intercalation capacitance[74], a fundamental understanding of the fluid behavior in the MXene interlayers should be pursued. One aspect is to determine the density of pure water within the MXene layers under a variety of conditions, including surface group functionalization, temperature, and presence of ions. This can be achieved through GCMC simulations in which insertion/deletion moves, alongside the standard MC moves, would equilibrate water within the MXene interlayer to the correct density.

While $Ti_3C_2T_x$ MXenes have been most commonly studied to this point[224], new variants are continuing to be discovered[69,225]. `mBuild` and the `MXenes` package have been designed with modularity in mind, and should allow for other MXenes to be constructed without too much additional effort. Without a dedicated force field for newer MXenes, a logical starting point is likely the Universal Force Field. Close collaboration with experiments and/or DFT should be done to ensure these ”off-the-shelf” force field parameters are sufficient to describe these systems.

CHAPTER 6

Improving Reproducibility of Molecular Simulation

6.1 Introduction

The field of molecular simulation is not immune to the challenge of reproducibility in science. The workflows of initialization for molecular simulations, from system construction to force field application, are often complex and involve methods utilizing GUIs, in-house code, and *ad hoc* edits. The instructions for these workflows are often documented in the methods or supplementary information of a paper. Often, important details are omitted making it difficult for other researchers to reproduce and ultimately extend the original work. Further, each molecular simulation engine uses a unique combination of units, functional forms, input files, and algorithm implementation. As a result, it is a non-trivial task to achieve agreement of results between different simulation engines. [1] [2] [3]

MoSDeF began development almost a decade ago to address the problems outlined above. In this chapter, the development of a Python package, `Pore-Builder`, to initialize systems of carbon slit pores is discussed. This work is featured in two journal articles[244,246] that demonstrate how TRUE workflows can be implemented with MoSDeF. The development of a package that acts as a MoSDeF interface for the Cassandra MC package[247], named MoSDeF-Cassandra, is also discussed. This work is currently submitted and also utilizes `Pore-Builder` to demonstrate the functionality of the package.

[1] Portions of this work reprinted with permission from the works below:

[2] P. T. Cummings, C. McCabe, C. R. Iacovella, A. Ledeczi, E. Jankowski, A. Jayaraman, J. C. Palmer, E. J. Maginn, S. C. Glotzer, J. A. Anderson, et al., AIChE Journal (2021), ISSN 0001-1541, Copyright 2021 American Institute of Chemical Engineers.

[3] R. S. DeFever, R. A. Matsumoto, A. W. Dowling, P. T. Cummings, and E. J. Maginn, Journal of Computational Chemistry (2021), Copyright 2021 Wiley Periodicals LLC.

6.2 Background

MoSDeF was originally developed at Vanderbilt University in collaboration with the Institute for Software Integrated Systems (ISIS) to aid in thecomputational screening of monolayer lubrication. The software library consists of `mBuild` for programmatic system construction and `foyer` for automatic force field parametrization. MoSDeF is open-source and has been developed with software best practices in mind. As such, all code is hosted and version-controlled on GitHub. On GitHub a pull request model is used to make modifications to the code which allows for code review and continuous integration (CI) to ensure the software works as intended and standards are enforced. Microsoft's Azure Pipelines is the specific service used for automated builds and testing, whereas `Codecov` is used to ensure additions to the codebase are covered by testing. New versions of `mBuild` and `foyer` are periodically released on the `conda-forge` channel of Anaconda Cloud.

`mBuild` contains a set of functions that can be used, extended, and/or combined to construct various chemical systems[96,246]. Systems are designed to be constructed hierarchically from smaller, interchangeable pieces. To achieve this, the main data structure of `mBuild` is the `Compound`, a general purpose 'container' to describe any object within a given system such as an atom, a molecule, a collection of `Compound` objects, etc. `Compound` objects can include `Ports` to define the locations and orientations at which connections with other `Compound` objects can occur. Two `Compound` objects can then be connected through functions within `mBuild` which creates a new composite `Compound`. This allows users to programmatically construct their chemical systems from scratch. Alternatively, `Compound` objects can be constructed through common structure file formats (`mol2`, `pdb`, etc.) and SMARTS language strings. `mBuild` uses a recipe architecture to construct specific chemistries and systems. Contained within the library are a set of base `recipes`, such as the `Polymer` class to construct alkane `Compound` objects. We encourage users to construct more complex or

specific systems as `recipes` as standalone Python packages. Others can then download and install these `recipes` to call them directly through `mBuild`. In this chapter, the development and usage of the `Pore-Builder`[248] package are discussed.

The `foyer`[98–100] library within MoSDeF is designed to apply force field parameters to chemical systems. To do so, force field parameters and rules are defined in an `XML` format which is an extension of the file format designed by `OpenMM`[249]. Force field rules are defined by the SMARTS language and `overrides` that determine rule precedence. DOIs can also be encoded into the force field `XML` further allowing for reproducibility. The force field `XML` files are designed to be loaded as a `Forcefield` object. `Forcefields` can easily be applied to `mBuild.Compound` objects to define the interaction parameters of a system.

A main goal of MoSDeF[198,199] is to integrate with numerous open-source molecular simulation engines to provide more seamless interconversion between the different input formats required by each. The GROMACS[121–125] MD software has been tightly integrated with MoSDeF since the early development of the project, leveraging `ParmEd`[250,251] to write the necessary input files to disk. MoSDeF has since enabled screening studies of diverse soft matter systems[103,108] that would have been otherwise difficult. LAMMPS[252], another open-source MD simulation engine, has also been supported since early development with custom readers and writers implemented in `mBuild`. Recently efforts have yielded tight integration with Cassandra[253], an open-source MC code developed by the Maginn Group of Notre Dame. `MoSDeF-Cassandra`[254] is a python wrapper for Cassandra that utilizes `MoSDeF` for system setup and force field application and calls Cassandra to run MC simulations. Cassandra is developed by the Maginn Group at the University of Notre Dame and is released under the GNU General Public License. The general workflow of running a MC simulation in Cassandra can be viewed in Fig. 3.1 of its user manual, Ref. 255. As discussed in the following section, the use of `MoSDeF-Cassandra` greatly simplifies the process of initializing and running a

simulation with Cassandra. Ongoing development efforts also include the integration of GPU-Optimized Monte Carlo (GOMC)[256] and the CP2K quantum chemistry package[257]. Integrating numerous simulation engines with `MoSDeF` enables comparisons of simulation results from different codes in a reproducible fashion. In the first section of this chapter, we replicate portions of the calculations of water in carbon slit pores performed by Keith Gubbins and colleagues[92] with five modern simulation software packages[244]. Using in-house code, Striolo *et al.* reported grand canonical Monte Carlo (GCMC) simulations of SPC/E water in carbon slit pores of various widths and reported water adsorption isotherms and the water structure within the pores. In this section, we first describe the development of the `Pore-Builder` `mBuild` recipe to construct systems of carbon slit pores for simulation. Then, we calculate the water adsorption isotherms with GCMC in GOMC and Cassandra. Once we determined the equilibrium number of water molecules in the pores at prescribed external pressures, the structure of water inside the pores was calculated using the following: MC simulations in the canonical (*NVT*) ensemble with GOMC and Cassandra, force-field-based *NVT* MD simulations with GROMACS and LAMMPS, and first-principles *NVT* MD simulations with CP2K.
In the following section, the development of `MoSDeF-Cassandra` is described in more detail[245]. Further, an example of a MC-MD workflow of an aqueous solution in a carbon slit pore is demonstrated.

6.3 Replicating work of Striolo *et al.*

6.3.1 Methods

The `Pore-Builder` recipe package[248] was developed through the use of `mBuild` and `foyer`. Specifically, the carbon crystal structure is initialized through the `mbuild.Lattice` class. The lattice vectors are a =0.2456 nm, b =0.2456 nm, and c =0.335 nm, and the Bravais angles are 90°, 90°, and 120°. These parameters produce carbon slit pores identical to those simulated by Striolo *et al.*[92]. The layers of graphene

have interlayer spacings of 0.335 nm with a carbon-carbon distance of 0.142 nm. The carbon atoms of these systems are designed to be fixed during the simulations. The details of each system are provided in Table 6.1 and snapshots of each system are provided in Fig. 6.1. Periodic boundary conditions were applied in all three spatial dimensions. Vacuum space was added in the direction normal to the pore. Simulation details specific to each simulation package are given below. The methods performed by collaborators are briefly summarized here, although a more detailed outline is presented in Ref. 244.

6.3.1.1 Force-field-based simulation details

Water was described by the SPC/E[82] model. The carbon-carbon LJ parameters were taken from Table 1 of Striolo *et al.*, and Lorentz-Berthelot[258,259] combining rules were used to define the carbon-water LJ interactions. LJ and Coulomb interactions were truncated at 0.9 nm (unless otherwise noted in Table 1), with long-range Coulomb interactions computed via an Ewald summation or grid-based counterpart. [4] No analytical tail corrections were applied to the LJ potential. There are technical details that differ between the original simulations of Striolo *et al.* and the work repeated here. Thus, our goal is less to reproduce the original work of Striolo *et al.*, and instead demonstrate the power of MoSDeF to show consistency between different simulation engines (GROMACS and LAMMPS for MD, Cassandra and GOMC for MC) and different simulation approaches (MD vs. MC).

6.3.1.2 GOMC

GOMC simulations were performed by Brad Crawford at Wayne State University. GOMC was first used for adsorption and desorption simulations in which the equilibrium density of water was determined as a function of chemical potential. GOMC was also used to perform Gibbs Ensemble Monte Carlo (GEMC), in which the water saturation pressure

[4] Striolo *et al.* appears to have used no long-range electrostatics solver, likely in conjunction with a group-based cutoff scheme. We have chosen to proceed with long-range electrostatics since this is now the de-facto standard and many modern codes do not support group-based cutoff schemes.

Table 6.1: Systems evaluated in this study. Dimensions are provided in nm.

System	Pore width	Box dimensions	Cutoff	$N_{Graphene}$	N_{water} *NVT*
large-1.0	1.0	$2.947 \times 2.978 \times 6.0$[a]	0.9	6	-
large-1.6	1.6	$2.947 \times 2.978 \times 6.0$[a]	0.9	6	-
large-2.0	2.0	$2.947 \times 2.978 \times 6.0$[a]	0.9	6	485
small-1.0	1.0	$0.982 \times 1.063 \times 2.0$	0.49	2	24
small-1.0	1.0	$0.982 \times 1.063 \times 2.0$	0.49	2	1

[a] GOMC dimensions differed in z-direction. See section 6.3.1.2 for details.

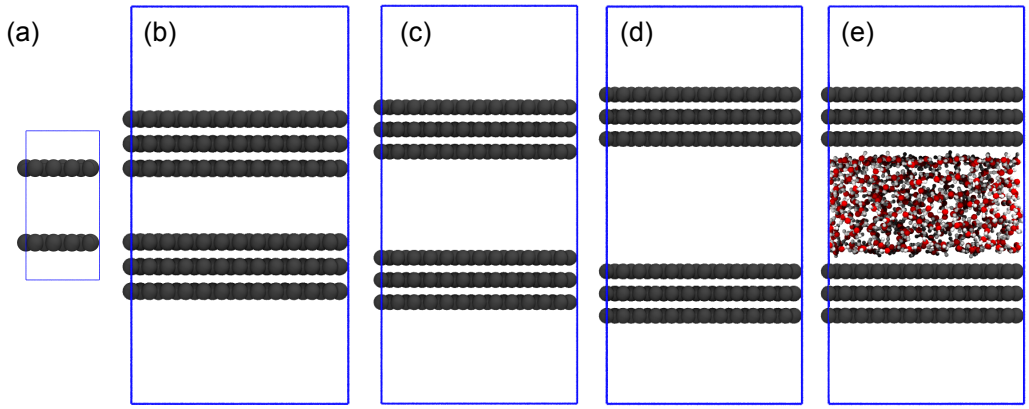

Figure 6.1: Snapshots of systems simulated in this work (the numbers refer to the pore width in nm): (a) small-1.0, (b) large-1.0, (c) large-1.6, (d) large-2.0, and (e) large-2.0 after pore filling. Carbon, oxygen, and hydrogen are shown as gray, red, and white spheres. Periodic boundaries are indicated by the blue lines. Figure taken from Ref. 244.

was determined. Finally, GOMC simulations were performed in the *NVT* ensemble to calculate structure properties of water inside the carbon pores.

6.3.1.3 Cassandra

Cassandra simulations were performed by Ryan DeFever of Notre Dame University. Similar to GOMC, GCMC simulations were performed in Cassandra to determine the equilibrium density of water as a function of chemical potential. Once these densities

were determined, simulations in the *NVT* ensemble were performed to calculate structure properties of water. Simulations were performed with `MoSDeF Cassandra` version 0.2.2 and Cassandra version 1.2.5.

6.3.1.4 GROMACS

The equations of motion were integrated with the leap-frog algorithm for 50 ns (200 ns for the small-1.0 nm/1 water system) using a time step of 1 fs. Water bonds and angles were constrained via LINCS[128] and the carbons atoms were held in place with `freezegrps`. Long range electrostatics were handled through the Fast Smooth Particle-Mesh Ewald method[126], with the `ewald-rtol` parameter set to 10^{-5}. Note that long-range electrostatics were turned off for the small-1.0 nm slit pore containing 1 water molecule. The number of k-space vectors in the large-2.0 system was set by a Fourier spacing of 0.12 nm, and was directly set to 16, 27, and 18 in Cartesian coordinates for the small-1.0 nm systems. The water molecules were thermostatted to 298 K with the Bussi thermostat[127] and a time constant of 1 ps. Simulations were performed with the 2020 version of GROMACS. Other than the small-1.0 nm/1 water molecule system, analysis is performed on the last 45 ns of each simulation trajectory.

6.3.1.5 LAMMPS

The equations of motion were solved with the equations of Shinoda *et al.* for 20 ns using a 1 fs time step.[260] The carbon atoms were excluded from the MD integration, rendering them fixed. Water bonds and angles were constrained with SHAKE[261]. Long range electrostatics were handled through the particle-particle-particle-mesh solver[262] with the relative force tolerance set to 10^{-5}. Temperature was controlled with the Nosé-Hoover chain thermostat at 298 K with the time constant set to 1 ps and chain length set to 3. Simulations were performed with the June 5, 2019 version of LAMMPS. Analysis is performed on the last 18 ns of the simulation trajectories for the small-1.0 nm system and the last 15 ns for the large-2.0 nm system.

6.3.1.6 CP2K

CP2K simulations were performed by Ramanish Singh of University of Minnesota. The simulations performed by CP2K are unique as its the only non-classical method studied here. More specifically, *NVT* ensemble first-principles molecular dynamics (FPMD) simulations were performed in the CP2K software version 7.0. Due to the added computational cost of FPMD, the small-1.0 nm and small-2.0 nm were simulated specifically for comparison with CP2K. Additionally, a system containing a single water molecule is simulated to further investigate the QM effects. Each system was equilibrated for 30 ps, and then sampled for 120 ps using a 0.5 fs timestep.

6.3.2 Results

6.3.2.1 Water Adsorption

Adsorption and desorption isotherms were computed for 1.0 nm and 1.6 nm slit pores with GCMC (large-1.0 nm and large-1.6 nm slit pore systems run with both GOMC and Cassandra, small-1.0 nm system run with Cassandra to determine number of water molecules for Section 3.2 below). Adsorption simulations were initialized with an empty pore. Desorption simulations were initialized with a pre-filled pore, where the number of water molecules in the pore at the start of the simulation corresponded to the pore loading at high pressure as determined from the GCMC adsorption simulations.

6.3.2.2 Relating μ to P/P^{sat}

Prior to completing the adsorption and desorption calculations a series of gas-phase simulations of SPC/E water were performed to establish a mapping between chemical potential and pressure. The ideal gas law was used to select the simulation box sizes such that there were a minimum $\sim$ 30-60 water molecules present. A comparison of GOMC and Cassandra results is shown in Fig. 6.2. Note that the two software packages employ a different definition of the chemical potential. In the case of SPC/E water the conversion from GOMC to Cassandra is $\mu' = \mu^{\mathrm{GOMC}} + 3k_BT\ln(\Lambda)$, where μ' is the Cassandra

chemical potential, k_B is the Boltzmann constant, T is the temperature, and Λ is the thermal de Broglie wavelength in units of angstroms.

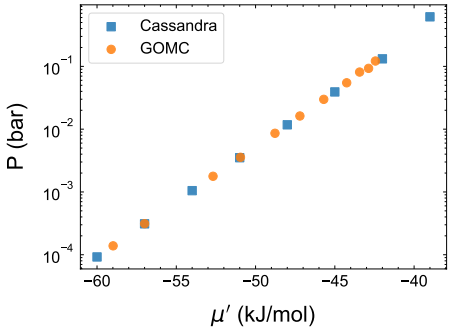

Figure 6.2: Computed pressure as a function of chemical potential (μ') for SPC/E water with Cassandra and GOMC. Data taken from Ref. 244.

The saturation pressure (P^{sat}) of water using the PC/E water model was computed at 298 K with Gibbs ensemble Monte Carlo (GEMC-*NVT*) in GOMC. Water's saturation pressure was employed to create a baseline in many of the analyses in this study (i.e., pressure divided by the saturation pressure or P/P^{sat}). This type of baseline, (P/P^{sat}), allows the simulation data to estimate the real-world pressure by merely plugging in the experimental saturation pressure. Grand Canonical Monte Carlo (GCMC-*NVT*) simulations are transferable to experimental conditions via the chemical potential (μ') and simulation pressure (P), which can be easily be determined in these simulations. The relationship between μ' and $\log(P)$ is approximately linear up to $P/P^{\text{sat}} = 10$, a linear fit between μ' and $\log(P)$ was used to relate a given chemical potential, μ' to P/P^{sat}.

6.3.2.3 Comparison with Striolo *et al.*

An equation of state method was used to relate the activity ($\zeta = \Lambda^{-3}\exp(\mu/k_BT)$) to P/P^{sat} in Ref. 92. P/P^{sat} was given by:

$$\frac{P}{P_0} = \frac{2\zeta\zeta_0^2 + (\rho_0 - \zeta_0)\zeta^2}{(\rho_0 + \zeta_0)\zeta_0^2} \tag{6.1}$$

The method[263] requires the activity at saturation (ζ_0) and vapor density at saturation (ρ_0).

Neither the values themselves nor method used to compute them were explicitly provided in Ref. 92, and the resulting P/P_0 is extremely sensitive to these values. A future publication[264] from the same authors indicate that their procedure was most likely as follows: perform GCMC of water vapor in a box with a 3.0 nm side length and gradually increase the chemical potential until the system condenses to the liquid phase, then take ρ_0 and ζ_0 as the values just prior to condensation. In order to compare our results to Ref. 92, we repeated this same procedure to estimate the values used for ρ_0 and ζ_0. Our calculations yielded $\zeta_0 = 2.15 \times 10^{-6}$ Å^{-3} and $\rho_0 = 2.58 \times 10^{-6}$ Å^{-3}. The figures from Ref. 92 were digitized and equation 6.1 was used to estimate the activities at which the original simulations were performed. We caution the reader that our comparison of the adsorption/desorption isotherms are imperfect and that a rigorous quantitative comparison between our results and Ref. 92 is not our objective. As already noted we chose to proceed with long range electrostatics solvers that were absent in the original work, and our simulations contain other small differences (e.g., carbon-carbon distances, 2D vs. 3D periodic boundary conditions, etc). Nevertheless, as shown below, it appears that we are able to achieve semi-quantitative agreement between the results of Ref. 92 and the simulations performed here.

6.3.2.4 Adsorption and desorption isotherms

Adsorption and desorption simulations were performed at a range of μ' that corresponded to $10^{-3} < P/P^{\text{sat}} < 10^{1}$. The results are reported in Fig. 6.3, where the amount of water in the pore is reported as the number of water molecules per unit of pore surface area. The results from Cassandra and GOMC show good agreement with regards to the loading of the pore at different pressures. There is satisfactory agreement for the adsorption and desorption pressure. We suspect the slight discrepancies between Cassandra and GOMC may have two possible causes: (1) the use of the MEMC-2 move and surrogate water molecules in GOMC (see section 6.3.1.2) and (2) the use of restricted insertion volume in

Cassandra (see section 6.3.1.3).

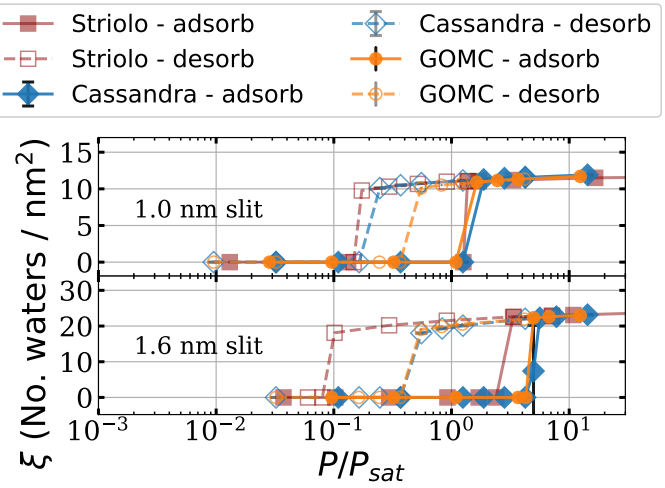

Figure 6.3: Adsorption and desorption isotherms for Cassandra, GOMC and the Striolo *et al.* data.[92] The P_{sat} value was obtained from GEMC-*NVT* water simulations. The Striolo *et al.* data was re-scaled as described in the text to match the P/P^{sat} definition in this work.[92] Data taken from Ref. 244.

6.3.2.5 Structure of Water

6.3.2.6 Calculation of Number Density and Order Parameter S

The number of water molecules inside of the pores were selected based upon the water adsorption results calculated from GCMC. All simulations used to compute the water structure in the pores were performed in the *NVT* ensemble. Fig. 6.4a and Fig. 6.4b report the number density profiles in the large-2.0 nm slit pore with 485 water molecules ($P/P^{\text{sat}} = 1.6$). The results from Cassandra, GOMC, GROMACS, and LAMMPS show nearly perfect agreement in terms of both oxygen and hydrogen number density inside of the slit pore, showing two fluid layers near each graphene wall. Additionally, all number density profiles are in good agreement with Fig. 9b from Ref. 92.

The orientational S order parameter used in Ref. 92 is defined as:

$$S = \frac{3\langle \cos^2\theta \rangle - 1}{2} \tag{6.2}$$

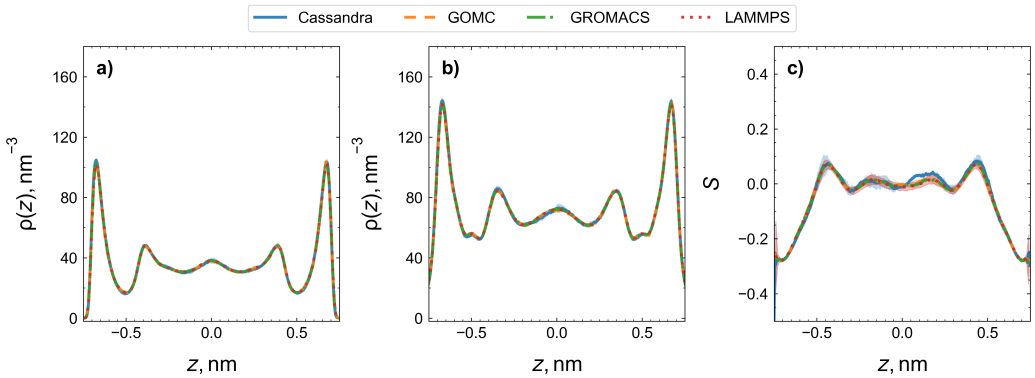

Figure 6.4: a) Oxygen-atom and b) Hydrogen-atom number density profiles, and c) S order parameter across the large-2.0 nm slit pore with 485 water molecules ($P/P^{\text{sat}} = 1.6$). z denotes the direction normal to pore walls, where $z = 0$ is set to the center of the pore. Uncertainties in the number density are on less than or equal to the line width.

where θ is the angle between the vector normal to the graphene walls and the vector drawn from the midpoint of the hydrogen atoms through center of the the oxygen atom (i.e. along the dipole). The S order parameter was calculated for the large-2.0 nm slit pore and is presented in Fig. 6.4c. Near the pore wall, the dipoles of the water molecules have a tendency to orient in a parallel fashion as indicated by the negative S order parameter. The water molecules near the middle of the pore are more bulk-like as shown by the random orientations. Overall, the results between the simulation engines are in good agreement with one other, and with Fig. 10b in Ref. 92.

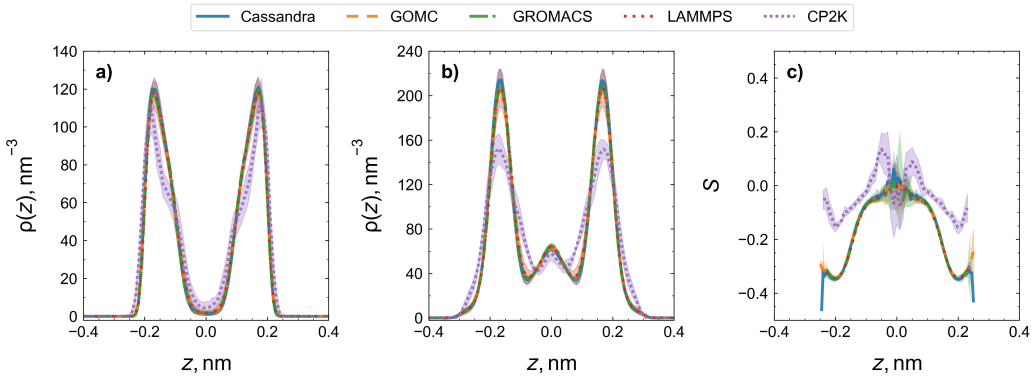

Figure 6.5: a) Oxygen-atom and b) hydrogen-atom number density profiles, and c) S order parameter across the small-1.0 nm slit pore with 24 water molecules ($P/P^{\text{sat}} = 1.6$). z denotes the direction normal to pore walls, where $z = 0$ is set to the center of the pore.

The number density profiles for the small-1.0 nm slit pore are displayed in Fig. 6.5a and Fig. 6.5b. This system contains 24 water molecules and has been constructed to be smaller than the large-2.0 nm slit pore system to allow for a direct comparison with first-principles simulations. The number density profiles computed from all four simulation codes using the SPC/E-water/LJ-graphene model (Cassandra, GOMC, GROMACS, LAMMPS) are in agreement with each other as well as with the result in Fig. 11 of Ref. 92. The oxygen atoms are arranged in a distinct layer near each pore wall. The hydrogen atoms also form a distinct layer neat each pore wall along with a small layer in the middle of the pore. The results from the FPMD performed in CP2K show some differences. The hydrogen number density peaks computed from CP2K are lower and broader when compared with the force field-based simulations. The oxygen number density profiles also display subtle differences that become more pronounced at low loading (see below).

The S order parameter for the small-1.0 nm slit pore is displayed in Fig. 6.5c. The error bars in the middle of the pore are larger as a result of the small system size and small probability of finding a water molecule in that region (see Fig. 6.5a). Similar to the large-2.0 nm pore, the water molecules near the walls are oriented parallel to the walls. Towards the middle of the pore, the water molecules are once again more randomly ordered. Simulations performed with the SPC/E-water/LJ-graphene model yield near perfect agreement for S across four simulation engines (Cassandra, GOMC, GROMACS, LAMMPS). The results reported here also show good agreement with Fig. 11b of Ref. 92.

To further investigate the differences in the density and orientational profiles observed between the SPC/E-water/LJ-graphene model and the KS-DFT description, both types of simulations were conducted for the small-1.0 nm slit pore system with just one water molecule. The symmetrized number density profile, the symmetrized S order parameter profile, and the normalized distribution of the angle θ for the one-molecule system are shown in Fig. 6.6. θ is again defined as the angle between the dipole moment vector of the water molecule and the surface normal vector (Note that for the angle distribution

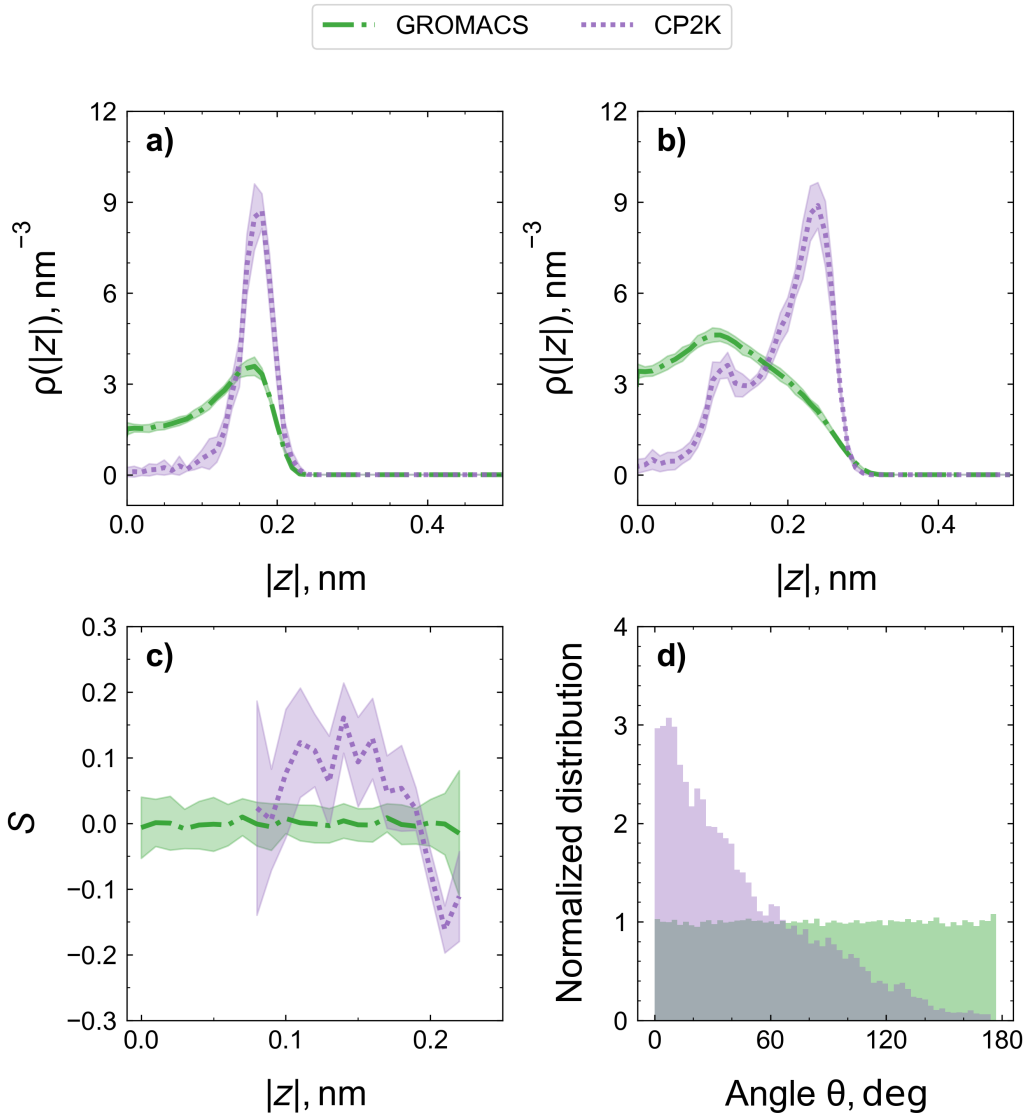

Figure 6.6: a) Oxygen-atom and b) hydrogen-atom number density profiles, c) S order parameter across the absolute value of a small-1.0 nm slit pore with a single water molecule, d) θ distribution across the pore. z denotes the direction normal to pore walls, where $z = 0$ is set to the center of the pore and θ is the angle between the dipole moment vector of the water molecule and the graphene surface normal vector.

profiles, the surface normal vector is chosen based on nearest proximity to a given water molecule). For the FPMD simulation, a peak in the hydrogen number density is observed at $|z| = 0.24$ nm, i.e., a distance of 0.26 nm from the graphene surface. The θ distribution exhibits a peak at $\theta = 0$ degrees with a relatively extended tail. These two observations suggest a favorable electrostatic interaction of the water dipole with the π-electrons of the

graphene sheet. This favorable electrostatic interaction also leads to a strong localization of the oxygen atom about 0.32 nm away from the graphene sheet with negligible density in the central region of the pore. In the force-field-based simulations, however, no peak is observed in the hydrogen number density near the graphene surface. Such a behavior of the hydrogen number density is expected as the water-graphene surface interactions only comprise of LJ interactions between the water oxygen and the graphene carbon atoms, and partial charges are not used to represent the charge distribution of the graphene sheet. As a result, the water-graphene interactions are inherently isotropic and a uniform distribution is observed for θ. Therefore, the strength of interactions between water molecules and graphene surface is different between force-field-based and first-principles simulations which causes the differences in the density and S profiles for the two types of simulations. As an aside, it should be noted that $S = 0$ can reflect either a uniform orientation or a strong preference for the magic angle of 54.74° that is roughly half of the H-O-H angle of water. However, the θ distribution does not indicate a propensity for 'hydrogen-bonded' configurations in which one of the hydrogen atoms of a water molecule is perpendicular with the graphene surface.

6.4 Development of MoSDeF Cassandra

6.4.1 Methods

`MoSDeF Cassandra` is a Python package independent of Cassandra that fully interfaces with MoSDeF. The package has been designed to make the process of system initialization for Cassandra simple and intuitive. The original initialization tools within Cassandra will continue to be developed, and `MoSDeF Cassandra` provides another interface for users to perform system setup for MC simulations.

To run a MC simulation, the following are required in initialization: an initial structure, definition of molecular interactions (Application of a force field), specified perturbations to attempt, and the desired probability distribution to sample. `MoSDeF Cassandra`

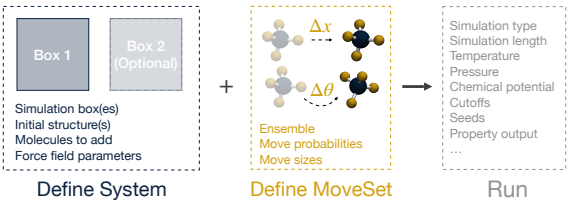

Figure 6.7: Overview of `MoSDeF Cassandra` interface. The `System` and `MoveSet` are created and passed to the `run` function, along with additional keyword arguments as necessary. Taken from Ref. 245.

handles these obligations through the `System` and `MoveSet` Python objects. The `System` object defines the chemical system (including box information and initial configurations) and energetic interactions. The `MoveSet` objected defines the perturbations, or MC moves, attempted in the simulation. This includes the type of move (e.g., translation, rotation), the probabilities of each move, and parameters that define each move (e.g., maximum translation distances, maximum number of molecules, etc.). A schematic of these two objects can be viewed in Fig. 6.7.

6.4.1.1 System

To avoid rewriting code already available in other Open-Source packages, the `System` object takes advantage of data structures from `ParmEd`[250,251] and `mBuild`[96,97] to store chemical system information in memory. A `System` object can be created with a minimum of three arguments: the initial configuration, force field information, and the number of molecules of each species. Optionally, the number of molecules for Cassandra to add can also be specified. The initial configurations are specified through a list of `mBuild.Box` classes and/or `Compound` classes. Similarly, the force field parameters are specified through a list of `ParmEd.Structure` objects. The number of molecules in the initial configuration and the number of molecules for Cassandra to insert into the system are defined by lists as well.

6.4.1.2 MoveSet

The `MoveSet` object handles MC move information in the Cassandra simulation and requires two arguments: the chemical topology information and statistical mechanical ensemble. Similar to `System`, the chemical topologies are defined by a list/s of `Structure` objects from `ParmEd`.

The `run` function is used to run the MC simulation in Cassandra once the `System` and `MoveSet` objects have been initialized. This function writes the information from these objects to disk, generates input files, and calls Cassandra to generate the fragment libraries, and run the simulation. `run` requires the following arguments: the `System` object, `MoveSet` object, the run type (”equilibration” or ”production”), the length of the simulation, and temperature. Additionally, the pressure or chemical potential must be specified if in the isothermal-isobaric or grand canonical ensembles. Additional keyword arguments may be passed as a Python dictionary.

6.4.1.3 Interoperability with other simulation software

MoSDeF provides much of the ”glue language” necessary for interoperability between Cassandra and other simulation software. In `mBuild`, `Compound` objects can be created through several methods: defining a molecular structure through SMILES language[265], loading common structure file formats (`xyz`, `pdb`, `mol2`), and converting from data structures in other open-source simulation software like `MDTraj`[120]. `ForceField` objects in `foyer` can also be applied to `Compound` objects which returns a fully parameterized `ParmEd.Structure`. This allows us to take advantage of the built-in writers available in `ParmEd` as well as in `mBuild`.

We demonstrate interoperability in the following section, where GCMC simulations of aqueous electrolytes under the confinement of graphene slit pores are first performed in Cassandra to determine the equilibrium densities. Using the same initialization routines in Python, simulations are then performed in GROMACS to determine the lateral diffusion

coefficients of the electrolyte species.

6.4.1.4 Specifying units

One unfortunate source of errors in molecular simulation is providing a value in the incorrect units. Different publications and simulation software packages use a plethora of different units for the same physical quantities. Inevitably, oversights and unit conversion mistakes occur. As a community, we should make every effort to eliminate these mistakes from molecular simulations. In `MoSDeF Cassandra`, we require that all physical quantities containing units be specified with units using the unyt library. unyt is a Python library that allows physical units to be attached to quantities. For example, specifying the pressure: `pressure = 3.0 * unyt.bar`. The pressure can then be converted to another valid unit, e.g., kPa, with: `pressure.to(unyt.kPa)`. The benefits of this approach are threefold: (1) the user no longer needs to know the default units of Cassandra since they can specify each quantity in any (dimensionally-valid) unit they wish, (2) the units associated with each quantity are abundantly clear to anyone reading a MoSDeF Cassandra script, and (3) it substantially reduces the likelihood of a unit conversion error by the user. Since the unyt package is mature and easy to use, the overhead of this requirement is minimal in comparison with its benefits.

6.4.2 Results

The importance of carbon materials to energy storage has been previously outlined. Because transport properties such as self-diffusivity and conductivity are important in the context of energy storage, MD is often used to simulate these systems. However, it is difficult to determine the correct fluid density in the pore with MD. Most experiments are performed under constant pressure, but the calculation of pressure in simulations for these systems becomes questionable as the pore walls are often kept rigid. Alternatively, GCMC can be used to determine the density of a fluid within a pore at a given chemical potential. The relationship between the pure fluid pressure and chemical potential is then used to

establish the effective pressure in the pore. However, the combined MD-MC approach is not without challenges. Running both MC and MD simulations often requires a separate set of input files for each simulation engine, increasing the likelihood of introducing errors into the simulations. MosDeF helps overcome these challenges by making it easy to generate input files for many simulation engines.

Here we demonstrate a simple MC-MD workflow with `MoSDeF Cassandra` and GROMACS wherein we compute the lateral diffusivity of water, sodium ions, and chloride ions in graphene slit pores as a function of pore width and salt concentration. Our goal is to highlight how the integration of Cassandra with the MoSDeF tools substantially lowers the barriers to performing combined MC-MD workflows, allowing users to take advantage of the benefits of both MC and MD. Once again, the workflow is comprised of a few pieces of Python code. In this example, we also take advantage of the fact that our workflow is written within a programming language to create reusable and importable functions for certain sections of the workflow. For example, we write a reusable `create_system` function that returns the starting configuration as an `mbuild.Compound`. The function arguments include the pore width, number of ions in the pore, number of water molecules in the pore, and identities of the positive and negative ions. Each simulation uses this single function to construct the initial system. We also define a reusable `run_gcmc` function that performs two serial MC simulations, a short *NVT* MC simulation to equilibrate the ions and a small number of water molecules placed within the pore, followed by a GCMC simulation to determine the equilibrium number of water molecules in the pore. As a result, performing the simulations only requires two simple function calls. The different systems are simulated by providing different arguments to the same two functions. This implementation demonstrates the construction of extensible workflows.[246] While we only report the results for 3 pore widths, 3 salt concentrations, and Na^+/Cl^- ion pairs, other researchers can easily re-use the `create_system` function to perform simulations with different pore widths,

concentrations, or types of ions. Not only are the reported simulations easy to reproduce, but a researcher interested in understanding the sensitivity of the reported results to certain choices or investigating similar systems can quickly and easily perform the necessary simulations. These considerations make the simulations TRUE[246]. Additional simulation details are outlined in the Ref. 245.

Each system initially comprises a graphene slit pore of some width, 75 water molecules, and 0, 4, or 8 NaCl ion pairs. A small amount of water is placed in the initial pore system to ensure that the pore saturates within reasonable simulation lengths; the goal of this work is not to investigate adsorption/desorption behavior in these systems. `MoSDeF Cassandra` is used to determine the equilibrium number of water molecules in each pore with GCMC following a brief *NVT* MC simulation to equilibrate the initial configuration. Insertion and deletion moves are only attempted for water molecules to maintain the number of ions in the pore and the charge neutrality of the system. The chemical potential of water is selected to correspond to the saturation condition for SPC/E water model at 298 K. Upon performing GCMC, the pores quickly fill with water, and the number of water molecules in the pore proceeds to equilibrate over several million MC moves (not shown). The average number of waters in the pore is computed for each system once the number of waters in the pore stabilizes. Representative snapshots after pore filling are shown in Fig. 6.8(a). Once the average number of water molecules in each pore has been determined with MC, pore-filled systems are constructed and simulated with *NVT* MD in GROMACS for 100 ns. The lateral diffusivity of the Na^+, Cl^-, and water atoms are calculated from the mean square displacement and reported in Fig. 6.8(b). As expected, the lateral diffusivity of all components is lower in the case of narrower pores and larger number of ion pairs.

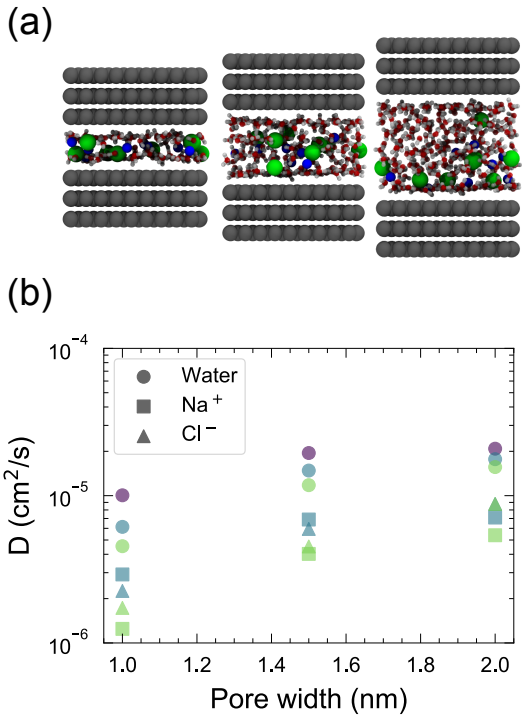

Figure 6.8: (a) Snapshots of systems simulated in this work, from left to right: 1.0 nm, 1.5, 2.0 nm pore width with 8 NaCl ion pairs. Oxygen, hydrogen, carbon, sodium, and chloride are shown in red, white, gray, blue, and green, respectively. (b) Water and ion diffusion as a function of pore width and the number of ion pairs. 0, 4, and 8 ion pairs shown with purple, blue, and green markers, respectively. Figure taken from Ref. 245.

6.5 Conclusions

In this chapter, the development and use of MoSDeF are described in order to make molecular simulation workflows more reproducible. The interoperability enabled by MoSDeF was first demonstrated by our study in which the work of Striolo *et al.* was replicated through five open-source simulation packages. The MC packages, GOMC and Cassandra were utilized to first determine the equilibrium densities of water in carbon slit pores using GCMC techniques. Then, simulations of water in the slit pores were performed in the *NVT* ensemble using GOMC, Cassandra, GROMAC, LAMMPS, and CP2K. Reasonable agreement was achieved between the original work and the various simulation packages.

Next, the motivation, design principles, and development of `MoSDeF Cassandra` were discussed in detail. `MoSDef Cassandra` has been designed to be user-friendly, interoperable with other software packages, and reproducible. We believe this is accomplished through clearly defined and robust data structures, comprehensive unit testing, and other features such as integration with `Unyt`. The functionality of `MoSDeF Cassandra` is demonstrated through a MC-MD workflow of simulating aqueous electrolytes in graphene slit pores. In particular, this example exemplifies how TRUE simulations can be performed with `MoSDeF Cassandra`.

Overall, this work demonstrates the functionality of the current tools of MoSDeF as well as adds to the growing list of MoSDeF tools. Hopefully, this work will lead to further adoption of MoSDeF in the molecular simulation community.

6.6 Future Work

To conclude, future work in regards to MoSDeF will be discussed. The current and future work around MoSDeF is mainly focused on adding and improving the functionality of the tools through the development of the General Molecular Simulation Object (GMSO).[266] One of the main current limitations of MoSDeF is that `foyer` leverages the

`ParmEd.Structure` as the core data structure for chemical topologies. `ParmEd` itself is a robust software package that supports a variety of force field functional forms and file formats from a number of software packages. It was designed primarily with the biomolecular field in mind and as a result, focuses on a specific type of atomistic CMD with two-body interactions, 12-6 LJ interactions, and point-charges defining Coulombic interactions. MoSDeF plans to support simulations that go beyond this scope, including but not limited to many-body interactions, Mie potentials, and polarizable models As a result, a new set of core data structures must be developed to support these features. MoSDeF has made significant strides at reproducibility in molecular simulation, especially in regards to CI and unit testing. These tests ensure the accuracy of input files for molecular simulation, including sanity checks for correct initial configuration, force field parameters, input files, etc. Despite these efforts, errors and discrepancies can still be introduced into a simulation. One reason is due to the small details and differences between molecular simulation packages that can have profound effects on the results. When replicating the work of Striolo *et al.*, we initially had difficulties getting agreement between the adsorption/ desorption isotherms between GOMC and Cassandra. The source of this discrepancy turned out to be different definitions of chemical potential for the two packages. Additionally, we had difficulty matching the number density profiles of water in certain pore systems between GROMACS and LAMMPS. Upon much debugging, the source was revealed to be how each package defines the relative accuracy of the Ewald summation for long-range electrostatics. Perhaps the most direct method to check for the accuracy of a simulation is to perform single-point energy calculations. In this process, a single step of a simulation is performed to calculate the total potential energy of a system. If a system is accurately implemented, the total potential energy will be consistent across multiple simulation packages. These validations were previously explored by Alex Yang through the `coMMMParE` package[267] in which energies are evaluated for various simulation packages through `ParmEd`. To further improve the reproducibility and

accuracy of molecular simulation, MoSDeF should strive to implement these checks in its suite of tools.

CHAPTER 7

Conclusions

Though a greater understanding of capacitive energy storage has led to performance improvements, much work remains to make supercapacitors commercially successful. Novel electrode materials and electrolytes are constantly being developed, and we must further strive to understand the underlying mechanisms that lead to improved device performance. In the field of molecular simulation, improved models partly due to constantly evolving hardware will lead to more accurate representations of these systems. Additionally, a greater emphasis on reproducibility will allow others to build off current work and hopefully lead to new insights at a faster rate. Improved experimental probes will similarly allow samples to be studied at greater resolutions. It was demonstrated in this work how a combination of computational and experimental methods can lead to a greater understanding of how electrolytes behave in bulk and under confinement of electrode materials. Improvement of methods as well as a continued emphasis on combined simulation and experimental approaches should yield a more comprehensive understanding of capacitive energy storage.

The previous chapters describe work to better understand systems related to capacitive energy storage at the molecular level. In Chapter 3, the effect of organic solvents on ionic liquid dynamics was rigorously examined through MD screening. It was found that solvents with greater diffusivities, and to a lesser extent, solvents that better screen ion-ion interactions result in the highest ionic liquid dynamics. Chapter 4 outlined the analysis of correlated dynamics of water and aqueous electrolytes through the VHF. Despite some quantitative differences, the various water models studied sufficiently reproduce the VHF produced from IXS. Chapter 5 examined the structural differences of ionic liquids in Ti_3C_2 MXenes with different interlayer spacings resulting from AA intercalation. In

Chapter 6, examples of reproducible workflows for molecular simulation are presented through the use of MoSDeF.

BIBLIOGRAPHY

1. Tech. Rep., EIA (2020), URL https://www.eia.gov/outlooks/ieo/pdf/ieo2020.pdf.

2. N. S. Lewis, Science **315**, 798 (2007), ISSN 00368075.

3. D. G. Nocera and M. P. Nash, Proceedings of the National Academy of Sciences of the United States of America **104** (2007).

4. H. I. Becker, *Low voltage electrolytic capacitor* (1957), uS Patent 2800616A.

5. B. K. Kim, S. Sy, A. Yu, and J. Zhang, *Electrochemical Supercapacitors for Energy Storage and Conversion* (American Cancer Society, 2015), pp. 1–25, ISBN 9781118991978, https://onlinelibrary.wiley.com/doi/pdf/10.1002/9781118991978.hces112, URL https://onlinelibrary.wiley.com/doi/abs/10.1002/9781118991978.hces112.

6. P. Simon and Y. Gogotsi, Accounts of Chemical Research **46**, 1094 (2013), ISSN 00014842.

7. F. Endres and S. Zein El Abedin, Physical Chemistry Chemical Physics **8**, 2101 (2006), ISSN 14639076.

8. P. Simon, Y. Gogotsi, and B. Dunn, Science **343**, 1210 (2014), ISSN 0036-8075, URL http://www.sciencemag.org/cgi/doi/10.1126/science.1249625.

9. F. J. de Sisternes, J. D. Jenkins, and A. Botterud, Applied Energy **175**, 368 (2016), ISSN 03062619.

10. J. P. Thomas and M. A. Qidwai, Jom **57**, 18 (2005), ISSN 10474838.

11. R. Ktz and M. Carlen, Electrochimica Acta **45**, 2483 (2000), ISSN 0013-4686, URL https://www.sciencedirect.com/science/article/pii/S0013468600003546.

12. A. C. Forse, C. Merlet, J. M. Griffin, and C. P. Grey, Journal of the American Chemical Society **138**, 5731 (2016), ISSN 15205126.

13. C. Merlet, D. T. Limmer, M. Salanne, R. van Roij, P. A. Madden, D. Chandler, and B. Rotenberg, The Journal of Physical Chemistry C p. 140527145351001 (2014), ISSN 1932-7447, 1404.0343, URL http://dx.doi.org/10.1021/jp503224w.

14. J. Libich, J. Máca, J. Vondrák, O. Čech, and M. Sedlaíková, Journal of Energy Storage **17**, 224 (2018), ISSN 2352152X.

15. Y. Wu and C. Cao, Science China Materials **61**, 1517 (2018), URL https://doi.org/10.1007/s40843-018-9290-y.

16. B. E. Conway (Springer Science and Business Media, 2013).

17. C. Zhao and W. Zheng, Frontiers in Energy Research **3**, 1 (2015), ISSN 2296598X.

18. Q. Wang, S. Chen, and D. Zhang, in *Carbon Nanotube Fibers and Yarns*, edited by M. Miao (Woodhead Publishing, 2020), The Textile Institute Book Series, pp. 243–270, ISBN 978-0-08-102722-6, URL https://www.sciencedirect.com/science/article/pii/B9780081027226000109.

19. K. L. Van Aken, J. K. McDonough, S. Li, G. Feng, S. M. Chathoth, E. Mamontov, P. F. Fulvio, P. T. Cummings, S. Dai, and Y. Gogotsi, J Phys Condens Matter **26**, 284104 (2014), ISSN 0953-8984, URL http://www.ncbi.nlm.nih.gov/pubmed/24920163.

20. L. Smith and B. Dunn, Science **350**, 918 (2015), ISSN 10959203.

21. W. Li, Journal of The Electrochemical Society **142**, 1742 (1995), ISSN 00134651, URL http://jes.ecsdl.org/cgi/doi/10.1149/1.2044187.

22. A. Lewandowski, A. Olejniczak, M. Galinski, and I. Stepniak, Journal of Power Sources **195**, 5814 (2010), ISSN 0378-7753, URL http://dx.doi.org/10.1016/j.jpowsour.2010.03.082.

23. L. Xia, L. Yu, D. Hu, and G. Z. Chen, Materials Chemistry Frontiers **1**, 584 (2017), ISSN 20521537.

24. M. Galiński, A. Lewandowski, and I. Stepniak, Electrochimica Acta **51**, 5567 (2006), ISSN 00134686.

25. T. Welton, Biophysical Reviews **10**, 691 (2018), ISSN 18672469.

26. M. G. D. Po and G. A. Voth, pp. 1744–1752 (2004).

27. R. Ratti, Advances in Chemistry **2014**, 1 (2014), ISSN 2356-6612.

28. C. Cadena, J. L. Anthony, J. K. Shah, T. I. Morrow, J. F. Brennecke, and E. J. Maginn, Journal of the American Chemical Society **126**, 5300 (2004), ISSN 00027863.

29. J. L. Anderson, J. N. K. Dixon, E. J. Maginn, and J. F. Brennecke, Journal of Physical Chemistry B **110**, 15059 (2006), ISSN 15206106.

30. C. Wang, H. Luo, X. Luo, H. Li, and S. Dai, Green Chemistry **12**, 2019 (2010), ISSN 14639270.

31. O. Y. Fajardo, F. Bresme, A. A. Kornyshev, and M. Urbakh, ACS Nano **11**, 6825 (2017), ISSN 1936086X.

32. F. Zhou, Y. Liang, and W. Liu, Chemical Society Reviews **38**, 2590 (2009), ISSN 14604744.

33. M. Watanabe, M. L. Thomas, S. Zhang, K. Ueno, T. Yasuda, and K. Dokko, Chemical Reviews **117**, 7190 (2017), ISSN 15206890.

34. H.-N. Kwon, S.-J. Jang, Y. C. Kang, and K. C. Roh, Scientific Reports **9**, 1180 (2019), ISSN 2045-2322, URL http://www.nature.com/articles/s41598-018-37322-y.

35. R. D. Rogers and K. R. Seddon, Science **302**, 792 (2003), ISSN 1095-9203.

36. M. Armand, F. Endres, D. R. MacFarlane, H. Ohno, and B. Scrosati, Nature Materials **8**, 621 (2009), ISSN 14764660, URL http://dx.doi.org/10.1038/nmat2448.

37. M. Lazzari, M. Mastragostino, and F. Soavi, Electrochemistry Communications **9**, 1567 (2007), ISSN 13882481.

38. P. Simon and Y. Gogotsi, Philosophical Transactions of the Royal Society A: Mathematical, Physical and Engineering Sciences **368**, 3457 (2010), ISSN 1364503X.

39. M. Salanne, C. Simon, P. Turq, and P. A. Madden, J. Phys. Chem. B **111**, 4678 (2007), ISSN 15206106.

40. K. R. Harris, J. Phys. Chem **114**, 9572 (2010).

41. R. Brookes, A. Davies, G. Ketwaroo, and P. A. Madden, Journal of Physical Chemistry B **109**, 6485 (2005), ISSN 15206106.

42. C. Schröder, M. Haberler, and O. Steinhauser, Journal of Chemical Physics **128** (2008), ISSN 00219606.

43. A. Lewandowski and A. Swiderska-mocek, Journal of Power Sources **194**, 601 (2009).

44. M. Díaz, A. Ortiz, and I. Ortiz, Journal of Membrane Science **469**, 379 (2014), ISSN 0376-7388, URL http://dx.doi.org/10.1016/j.memsci.2014.06.033.

45. M. Thomas, M. Brehm, O. Hollóczki, and B. Kirchner, Chemistry - A European Journal **20**, 1622 (2014), ISSN 15213765.

46. A. Chaumont, R. Schurhammer, and G. Wipff, Journal of Physical Chemistry B **109**, 18964 (2005), ISSN 15206106.

47. O. Hollóczki, F. Malberg, T. Welton, and B. Kirchner, Phys. Chem. Chem. Phys. **16**, 16880 (2014), ISSN 1463-9076, URL http://xlink.rsc.org/?DOI=C4CP01177E.

48. M. A. Gebbie, M. Valtiner, X. Banquy, E. T. Fox, W. A. Henderson, and J. N. Israelachvili, Proceedings of the National Academy of Sciences **110**, 9674 (2013), ISSN 0027-8424, URL http://www.pnas.org/cgi/doi/10.1073/pnas.1307871110.

49. M. Sha, H. Dong, F. Luo, Z. Tang, G. Zhu, and G. Wu, The Journal of Physical Chemistry Letters **6**, 3713 (2015).

50. K. Ueno, H. Tokuda, and M. Watanabe, Physical Chemistry Chemical Physics **12**, 1648 (2010), ISSN 14639076.

51. H. Tokuda, S. Tsuzuki, A. Bin, H. Susan, and K. Hayamizu, J. Phys. Chem. B **110**, 19593 (2006).

52. H. Tokuda, K. Hayamizu, K. Ishii, M. A. B. H. Susan, and M. Watanabe, J. Phys. Chem. B **108**, 16593 (2004), ISSN 15206106, 1108.3610.

53. H. Tokuda, K. Hayamizu, K. Ishii, M. A. B. H. Susan, and M. Watanabe, Journal of Physical Chemistry B **109**, 6103 (2005), ISSN 15206106, 1108.3610.

54. N. C. Osti, K. L. Van Aken, M. W. Thompson, F. Tiet, D.-e. Jiang, P. T. Cummings, Y. Gogotsi, and E. Mamontov, The Journal of Physical Chemistry Letters p. acs.jpclett.6b02587 (2016), ISSN 1948-7185, URL http://pubs.acs.org/doi/abs/10.1021/acs.jpclett.6b02587.

55. A. B. Mcewen, H. L. Ngo, K. Lecompte, and J. L. Goldman, **146**, 1687 (1999).

56. T. Sato, G. Masuda, and K. Takagi, Electrochimica Acta **49**, 3603 (2004), ISSN 00134686.

57. V. Ruiz, T. Huynh, S. R. Sivakkumar, and A. G. Pandolfo, RSC Advances **2**, 5591 (2012), ISSN 2046-2069, URL http://xlink.rsc.org/?DOI=c2ra20177a.

58. Y. Zhai, Y. Dou, D. Zhao, P. F. Fulvio, R. T. Mayes, and S. Dai, Advanced Materials **23**, 4828 (2011), ISSN 1521-4095.

59. X. Zhao, B. M. Sánchez, P. J. Dobson, and P. S. Grant, Nanoscale **3**, 839 (2011), ISSN 20403364.

60. M. Thompson, B. Dyatkin, H.-W. Wang, C. Turner, X. Sang, R. Unocic, C. Iacovella, Y. Gogotsi, A. van Duin, and P. Cummings, C (2017), ISSN 2311-5629.

61. Y. Zhang, B. Dyatkin, and P. T. Cummings, Journal of Physical Chemistry C **123**, 12583 (2019), ISSN 19327455.

62. C. Fu, Y. Kuang, Z. Huang, X. Wang, Y. Yin, J. Chen, and H. Zhou, Journal of Solid State Electrochemistry **15**, 2581 (2011), ISSN 14328488.

63. S. Jo, S.-W. Park, Y. Shim, and Y. Jung, Electrochimica Acta **247**, 634 (2017), ISSN 00134686, URL http://linkinghub.elsevier.com/retrieve/pii/S001346861731407X.

64. G. Feng and P. T. Cummings, Journal of Physical Chemistry Letters **2**, 2859 (2011), ISSN 19487185.

65. M. Naguib, M. Kurtoglu, V. Presser, J. Lu, J. Niu, M. Heon, L. Hultman, Y. Gogotsi, and M. W. Barsoum, Advanced Materials **23**, 4248 (2011), ISSN 09359648.

66. A. Shahzad, K. Rasool, W. Miran, M. Nawaz, J. Jang, K. A. Mahmoud, and D. S. Lee, ACS Sustainable Chemistry and Engineering **5**, 11481 (2017), ISSN 21680485.

67. Q. Zhang, J. Teng, G. Zou, Q. Peng, Q. Du, T. Jiao, and J. Xiang, Nanoscale **8**, 7085 (2016), ISSN 20403372.

68. J. Zhu, E. Ha, G. Zhao, Y. Zhou, D. Huang, G. Yue, L. Hu, N. Sun, Y. Wang, L. Y. S. Lee, et al., Coordination Chemistry Reviews **352**, 306 (2017), ISSN 00108545.

69. Z. W. Seh, K. D. Fredrickson, B. Anasori, J. Kibsgaard, A. L. Strickler, M. R. Lukatskaya, Y. Gogotsi, T. F. Jaramillo, and A. Vojvodic, ACS Energy Letters **1**, 589 (2016), ISSN 2380-8195, URL http: //pubs.acs.org/doi/abs/10.1021/acsenergylett.6b00247{#}.V7i-fWH4tsE.mendeley.

70. N. C. Osti, M. Naguib, A. Ostadhossein, Y. Xie, P. R. Kent, B. Dyatkin, G. Rother, W. T. Heller, A. C. Van Duin, Y. Gogotsi, et al., ACS Applied Materials and Interfaces **8**, 8859 (2016), ISSN 19448252.

71. M. Naguib, J. Come, B. Dyatkin, V. Presser, P. L. Taberna, P. Simon, M. W. Barsoum, and Y. Gogotsi, Electrochemistry Communications **16**, 61 (2012), ISSN 13882481, URL http://dx.doi.org/10.1016/j.elecom.2012.01.002.

72. E. Kayali, A. Vahidmohammadi, J. Orangi, and M. Beidaghi, ACS Applied Materials and Interfaces **10**, 25949 (2018), ISSN 19448252.

73. M. Ghidiu, M. R. Lukatskaya, M.-Q. Zhao, Y. Gogotsi, and M. W. Barsoum, Nature **516**, 78 (2014), ISSN 0028-0836, URL http://dx.doi.org/10.1038/nature13970.

74. M. R. Lukatskaya, O. Mashtalir, C. E. Ren, Y. D. Agnese, M. W. Barsoum, and Y. Gogotsi, Science **341**, 1502 (2013), ISSN 0036-8075, 1095-9203.

75. M. Naguib, V. N. Mochalin, M. W. Barsoum, and Y. Gogotsi, Advanced Materials **26**, 992 (2014), ISSN 09359648.

76. M. D. Levi, M. R. Lukatskaya, S. Sigalov, M. Beidaghi, N. Shpigel, L. Daikhin, D. Aurbach, M. W. Barsoum, and Y. Gogotsi, Advanced Energy Materials **5** (2015), ISSN 16146840.

77. M. R. Lukatskaya, S. Kota, Z. Lin, M.-Q. Zhao, N. Shpigel, M. D. Levi, J. Halim, P.-L. Taberna, M. W. Barsoum, P. Simon, et al., Nature Energy **2**, 17105 (2017), URL https://doi.org/10.1038/nenergy.2017.105http://10.0.4.14/nenergy.2017.105https: //www.nature.com/articles/nenergy2017105{#}supplementary-information.

78. E. J. Maginn and J. R. Elliott, Industrial and Engineering Chemistry Research **49**, 3059 (2010), ISSN 08885885.

79. P. Paricaud, M. Pedota, A. A. Chialvo, and P. T. Cummings, Journal of Chemical Physics **122** (2005), ISSN 00219606.

80. P. T. Kiss and A. Baranyai, Journal of Chemical Physics **138** (2013), ISSN 00219606.

81. J. J. Potoff and G. Kamath, Journal of Chemical and Engineering Data **59**, 3144 (2014), ISSN 15205134.

82. H. J. C. Berendsen, J. R. Grigera, and T. P. Straatsma, Journal of Physical Chemistry **91**, 6269 (1987).

83. W. L. Jorgensen, J. Chandrasekhar, J. D. Madura, R. W. Impey, and M. L. Klein, Journal of Chemical Physics **79**, 926 (1983), ISSN 09725938.

84. W. L. Jorgensen, D. S. Maxwell, and J. Tirado-Rives, J. Am. Chem. Soc. **118**, 11225 (1996), ISSN 0002-7863.

85. Y. Zhang and E. J. Maginn, The Journal of Physical Chemistry Letters **6**, 700 (2015), ISSN 1948-7185, URL http://pubs.acs.org/doi/abs/10.1021/acs.jpclett.5b00003.

86. Y. Zhang, A. Otani, and E. J. Maginn, Journal of Chemical Theory and Computation **11**, 3537 (2015), ISSN 1549-9618, URL http://pubs.acs.org/doi/abs/10.1021/acs.jctc.5b00351.

87. P. Mark and L. Nilsson, Journal of Physical Chemistry A **105**, 9954 (2001), ISSN 10895639.

88. J. P. Ulmschneider, M. B. Ulmschneider, and A. De Nola, Journal of Physical Chemistry B **110**, 16733 (2006), ISSN 15206106.

89. W. L. Jorgensen and J. Tirado-Rives, Journal of Physical Chemistry **100**, 14508 (1996), ISSN 00223654.

90. D. Frenkel and B. Smit, in *Understanding Molecular Simulation (Second Edition)*, edited by D. Frenkel and B. Smit (Academic Press, San Diego, 2002), pp. 23–61, second edition ed., ISBN 978-0-12-267351-1, URL https://www.sciencedirect.com/science/article/pii/B9780122673511500055.

91. D. J. Adams, Molecular Physics **29**, 307 (1975), ISSN 13623028.

92. A. Striolo, A. A. Chialvo, P. T. Cummings, and K. E. Gubbins, Langmuir **19**, 8583 (2003), ISSN 07437463.

93. E. A. Müller, L. F. Rull, L. F. Vega, and K. E. Gubbins, Journal of Physical Chemistry **100**, 1189 (1996), ISSN 00223654.

94. M. Baker, Nature **533**, 353 (2016).

95. J. C. Palmer, A. Haji-Akbari, R. S. Singh, F. Martelli, R. Car, A. Z. Panagiotopoulos, and P. G. Debenedetti, Journal of Chemical Physics **148**, 1 (2018), ISSN 00219606, URL http://dx.doi.org/10.1063/1.5029463.

96. *mBuild Website*, URL https://mbuild.mosdef.org.

97. *mBuild Github repository*, URL https://github.com/mosdef-hub/mbuild.

98. *Foyer Website*, URL https://foyer.mosdef.org.

99. *Foyer Github repository*, URL https://github.com/mosdef-hub/foyer.

100. C. Klein, A. Z. Summers, M. W. Thompson, J. B. Gilmer, C. McCabe, P. T. Cummings, J. Sallai, and C. R. Iacovella, Computational Materials Science **167**, 215 (2019), ISSN 09270256, 1812.06779.

101. C. S. Adorf, P. M. Dodd, V. Ramasubramani, and S. C. Glotzer, Comput. Mater. Sci. **146**, 220 (2018).

102. V. Ramasubramani, C. Adorf, P. Dodd, B. Dice, and S. Glotzer, Proceedings of the Python in Science Conference (Scipy) (2018).

103. A. Z. Summers, J. B. Gilmer, C. R. Iacovella, P. T. Cummings, and C. McCabe, J. Chem. Theory Comput. **16**, 1779 (2020).

104. N. C. Craven, J. B. Gilmer, C. J. Spindel, A. Z. Summers, C. R. Iacovella, and C. McCabe, Journal of Chemical Physics **154** (2021), ISSN 10897690, URL https://doi.org/10.1063/5.0032658.

105. D. Pech, M. Brunet, H. Durou, P. Huang, V. Mochalin, Y. Gogotsi, P.-L. Taberna, and P. Simon, Nature nanotechnology **5**, 651 (2010), ISSN 1748-3395, URL http://www.ncbi.nlm.nih.gov/pubmed/20711179.

106. M. Ue, M. Takeda, M. Takehara, and S. Mori, **144**, 10 (1997).

107. D. Weingarth, H. Noh, A. Foelske-Schmitz, A. Wokaun, and R. Kötz, Electrochimica Acta **103**, 119 (2013), ISSN 00134686, URL http://dx.doi.org/10.1016/j.electacta.2013.04.057.

108. M. W. Thompson, R. Matsumoto, R. L. Sacci, N. C. Sanders, and P. T. Cummings, Journal of Physical Chemistry B **123**, 1340 (2019), ISSN 15205207.

109. R. Matsumoto, M. W. Thompson, and P. T. Cummings, Journal of Physical Chemistry B **123**, 9944 (2019), ISSN 15205207.

110. N. C. Osti, R. A. Matsumoto, M. W. Thompson, P. T. Cummings, M. Tyagi, and E. Mamontov, J. Phys. Chem. C **123**, 19354 (2019), ISSN 1932-7447.

111. J. Cui, T. Kobayashi, R. L. Sacci, R. A. Matsumoto, P. T. Cummings, and M. Pruski, The Journal of Physical Chemistry B **124**, 9931 (2020).

112. H. Liu and E. Maginn, Journal of Chemical Physics **135** (2011), ISSN 00219606.

113. H. Liu, E. Maginn, A. E. Visser, N. J. Bridges, and E. B. Fox, Industrial and Engineering Chemistry Research **51**, 7242 (2012), ISSN 08885885.

114. O. Borodin, The journal of physical chemistry. B **113**, 11463 (2009), ISSN 1520-6106, URL http://www.ncbi.nlm.nih.gov/pubmed/19637900.

115. J. N. Canongia Lopes, J. Deschamps, and A. A. H. Pádua, J. Phys. Chem. B **108**, 2038 (2004), ISSN 1520-6106, URL http://pubs.acs.org/doi/abs/10.1021/jp0362133http://dx.doi.org/10.1021/jp0362133{%}5Cnhttp://pubs.acs.org/doi/pdfplus/10.1021/jp0362133.

116. J. N. Canongia Lopes and A. A. H. Pádua, The Journal of Physical Chemistry B **108**, 16893 (2004), ISSN 1520-6106, URL http://pubs.acs.org/doi/abs/10.1021/jp0476545.

117. J. N. Canongia Lopes and A. A. H. Pádua, Journal of Physical Chemistry B **110**, 19586 (2006), ISSN 15206106.

118. J. N. Canongia Lopes and A. A. H. Pádua, Theor. Chem. Acc **131**, 1129 (2012), ISSN 1432-881X, URL http://link.springer.com/10.1007/s00214-012-1129-7.

119. L. Martínez, R. Andrade, E. G. Birgin, and J. M. Martínez, J. of Comp. Chem. **30**, 2157 (2009), ISSN 01928651, NIHMS150003, URL http://doi.wiley.com/10.1002/jcc.21224.

120. R. T. McGibbon, K. A. Beauchamp, M. P. Harrigan, C. Klein, J. M. Swails, C. X. Hernández, C. R. Schwantes, L. P. Wang, T. J. Lane, and V. S. Pande, Biophys. J. **109**, 1528 (2015), ISSN 15420086.

121. M. J. Abraham, T. Murtola, R. Schulz, S. Páll, J. C. Smith, B. Hess, and E. Lindahl, SoftwareX **1-2**, 19 (2015), ISSN 23527110.

122. S. Páll, M. J. Abraham, C. Kutzner, B. Hess, and E. Lindahl, in *Solving Software Challenges for Exascale: International Conference on Exascale Applications and Software, EASC 2014, Stockholm, Sweden, April 2-3, 2014, Revised Selected Papers*, edited by S. Markidis and E. Laure (Springer International Publishing, Cham, 2015), pp. 3–27, ISBN 978-3-319-15976-8, URL https://doi.org/10.1007/978-3-319-15976-8{_}1.

123. S. Pronk, S. Páll, R. Schulz, P. Larsson, P. Bjelkmar, R. Apostolov, M. R. Shirts, J. C. Smith, P. M. Kasson, D. van der Spoel, et al., Bioinformatics **29**, 845 (2013), ISSN 1460-2059, 1011.1669, URL http://arxiv.org/abs/1011.1669http://dx.doi.org/10.1088/1751-8113/44/8/085201http://stacks.iop.org/1751-8121/44/i=8/a=085201?key=crossref.abc74c979a75846b3de48a5587bf708fhttps://academic.oup.com/bioinformatics/article-lookup/doi/10.1093/bioinformatics/.

124. E. Lindahl and B. Hess, Journal of Molecular Modeling **7**, 306 (2001).

125. B. Hess, S. Uppsala, and E. Lindahl, Journal of Chemical Theory and Computation **4**, 435 (2008).

126. U. Essmann, L. Perera, M. L. Berkowitz, T. Darden, H. Lee, and L. G. Pedersen, The Journal of Chemical Physics **103**, 8577 (1995), ISSN 00219606.

127. G. Bussi, D. Donadio, and M. Parrinello, The Journal of chemical physics **126**, 014101 (2007).

128. B. Hess, H. Bekker, H. J. C. Berendsen, and J. G. E. M. Fraaije, Journal of Computational Chemistry **1472**, 1463 (1997).

129. M. W. Thompson and R. Matsumoto, *pairing*, https://github.com/mattwthompson/pairing (2019).

130. E. M. Sevick, P. A. Monson, and J. M. Ottino, J. Chem. Phys. **88**, 1198 (1988), ISSN 00219606.

131. L. J. A. Siqueira and M. C. C. Ribeiro, J. Phys. Chem. B **113**, 1074 (2009), ISSN 15206106.

132. V. Lindahl, J. Lidmar, and B. Hess, J. Chem. Phys. **141** (2014), ISSN 00219606, 1407.7415.

133. J. D. Hunter, Comput Sci Eng **9**, 90 (2007).

134. E. Mamontov and K. W. Herwig, Review of Scientific Instruments **82**, 085109 (2011), https://doi.org/10.1063/1.3626214, URL https://doi.org/10.1063/1.3626214.

135. J. P. Embs, F. Juranyi, and R. Hempelmann, Zeitschrift fur Physikalische Chemie **224**, 5 (2010), ISSN 09429352.

136. G. Pagès, V. Gilard, R. Martino, and M. Malet-Martino, Analyst **142**, 3771 (2017), ISSN 13645528.

137. K. R. Seddon, in *The International George Papatheodorou Symposium: Proceedings, ed. S. Boghosian, V. Dracopoulos, CG Kontoyannis and GA Voyiatzis, Institute of Chemical Engineering and High Temperature Chemical Processes, Patras* (1999), pp. 131–135.

138. X. Zhang, Z. Liu, and W. Wang, AIChE Journal **54**, 2717 (2008), ISSN 00011541, 0201037v1, URL http://doi.wiley.com/10.1002/aic.11573.

139. A. Maiti, ChemSusChem **2**, 628 (2009), ISSN 18645631, URL http://doi.wiley.com/10.1002/cssc.200900086.

140. S. E. McLeese, J. C. Eslick, N. J. Hoffmann, A. M. Scurto, and K. V. Camarda, Computers and Chemical Engineering **34**, 1476 (2010), ISSN 00981354, URL http://dx.doi.org/10.1016/j.compchemeng.2010.02.017.

141. A. T. Karunanithi and A. Mehrkesh, AIChE Journal **59**, 4627 (2013), ISSN 00011541, URL http://doi.wiley.com/10.1002/aic.14228.

142. K. G. Sprenger, V. W. Jaeger, and J. Pfaendtner, Journal of Physical Chemistry B **119**, 5882 (2015), ISSN 15205207.

143. J. N. a. Canongia Lopes and A. A. H. Pádua, Journal of Physical Chemistry B **110**, 3330 (2006), ISSN 15206106.

144. G. Saielli, A. Bagno, and Y. Wang, Journal of Physical Chemistry B **119**, 3829 (2015), ISSN 15205207.

145. A. Triolo, O. Russina, H.-J. Bleif, and E. Di Cola, Journal Of Physical Chemistry B **111**, 4641 (2007), ISSN 1520-6106, URL http://pubs.acs.org/doi/abs/10.1021/jp067705t{%}5Cnpapers3://publication/doi/10.1021/jp067705t.

146. M. S. Kelkar, W. Shi, and E. J. Maginn, Ind. Eng. Chem. Res. **47**, 9115 (2008), ISSN 08885885, URL http://pubs.acs.org/doi/abs/10.1021/ie800843u.

147. E. T. Fox, E. Paillard, O. Borodin, and W. A. Henderson, J. Phys. Chem. C **117**, 78 (2013), ISSN 19327447.

148. P. B. Sánchez, B. González, J. Salgado, A. A. Pádua, and J. García, J. Mol. Liq. **265**, 114 (2018), ISSN 01677322, URL https://doi.org/10.1016/j.molliq.2018.04.064.

149. V. K. Sharma, S. Solanki, and S. Bhagour, J. Chem. Eng. Data **59**, 1140 (2014), ISSN 0021-9568, URL http://pubs.acs.org/doi/10.1021/je4004965.

150. J. G. Kirkwood, J. Chem. Phys. **7**, 911 (1939), ISSN 00219606.

151. J. G. McDaniel and C. Y. Son, J. Phys. Chem. B **122**, 7154 (2018), ISSN 15205207.

152. C. Schröder, Physical Chemistry Chemical Physics **14**, 3089 (2012), ISSN 1463-9076, URL http://xlink.rsc.org/?DOI=c2cp23329k.

153. T. Köddermann, D. Paschek, and R. Ludwig, ChemPhysChem **8**, 2464 (2007), ISSN 14394235, 1408.1149.

154. K. Goloviznina, J. Canongia Lopes, M. Costa Gomes, and A. A. H. Pádua, Journal of Chemical Theory and Computation **15**, 5858 (2019), URL https://doi.org/10.1021/acs.jctc.9b00689.

155. Y. Zhang, B. Dyatkin, and P. T. Cummings, Journal of Physical Chemistry C **123**, 12583 (2019), ISSN 19327455.

156. X. Wang, T. S. Mathis, K. Li, Z. Lin, L. Vlcek, T. Torita, N. C. Osti, C. Hatter, P. Urbankowski, A. Sarycheva, et al., Nature Energy **4**, 241 (2019).

157. A. K. Soper, Chemical Physics **258**, 121 (2000), ISSN 03010104.

158. A. K. Soper and C. J. Benmore, Physical Review Letters **101**, 1 (2008), ISSN 00319007.

159. A. K. Soper, ISRN Physical Chemistry **2013**, 1 (2013), ISSN 2090-7761, URL http://www.hindawi.com/journals/isrn/2013/279463/.

160. T. Proffen, S. J. L. Billinge, T. Egami, and D. Louca, Zeitschrift fr Kristallographie - Crystalline Materials **218**, 132 (2003), URL https://doi.org/10.1524/zkri.218.2.132.20664.

161. B. H. Toby and T. Egami, Acta Crystallographica Section A **48**, 336 (1992), URL https://doi.org/10.1107/S0108767391011327.

162. Y. Shinohara, R. Matsumoto, M. Thompson, C. Ryu, W. Dmowski, T. Iwashita, D. Ishikawa, A. Baron, P. Cummings, and T. Egami, Journal of Physical Chemistry Letters **10** (2019), ISSN 19487185.

163. R. A. Matsumoto, M. W. Thompson, V. Q. Vuong, W. Zhang, Y. Shinohara, A. C. T. van Duin, P. R. C. Kent, S. Irle, T. Egami, and P. T. Cummings (2021), in preparation.

164. L. Van Hove, Phys. Rev. **95**, 249 (1954), URL https://link.aps.org/doi/10.1103/PhysRev.95.249.

165. T. Iwashita, B. Wu, W.-R. Chen, S. Tsutsui, A. Q. R. Baron, and T. Egami (????).

166. T. Egami and Y. Shinohara, Journal of Chemical Physics **153** (2020), ISSN 10897690, URL https://doi.org/10.1063/5.0024013.

167. Y. Shinohara, W. Dmowski, T. Iwashita, B. Wu, D. Ishikawa, A. Q. Baron, and T. Egami, Physical Review E **98**, 1 (2018), ISSN 24700053.

168. Y. Shinohara, W. Dmowski, T. Iwashita, D. Ishikawa, A. Q. R. Baron, and T. Egami, Physical Review E **102**, 32604 (2020), ISSN 2470-0045, URL https://doi.org/10.1103/PhysRevE.102.032604.

169. S. M. Mahurin, E. Mamontov, M. W. Thompson, P. Zhang, C. H. Turner, P. T. Cummings, and S. Dai, Appl. Phys. Lett. **109** (2016), ISSN 00036951.

170. C. Zhan, C. Lian, Y. Zhang, M. W. Thompson, Y. Xie, J. Wu, P. R. Kent, P. T. Cummings, D. en Jiang, and D. J. Wesolowski, Adv. Sci. **1700059** (2017), ISSN 21983844.

171. Q. Gao, W. Sun, P. Ilani-Kashkouli, A. Tselev, P. R. Kent, N. Kabengi, M. Naguib, M. Alhabeb, W. Y. Tsai, A. P. Baddorf, et al., Energy and Environmental Science **13**, 2549 (2020), ISSN 17545706.

172. T. C. Moore, R. Hartkamp, C. R. Iacovella, A. L. Bunge, and C. McCabe, arXiv pp. 113–125 (2017), ISSN 23318422.

173. M. Karplus and J. A. McCammon, Nature Structural Biology **9**, 646 (2002), URL https://doi.org/10.1038/nsb0902-646.

174. J. D. Durrant and J. A. McCammon, BMC Biology **9**, 71 (2011), URL https://doi.org/10.1186/1741-7007-9-71.

175. D. L. Mobley, A. P. Graves, J. D. Chodera, A. C. McReynolds, B. K. Shoichet, and K. A. Dill, Journal of Molecular Biology **371**, 1118 (2007), ISSN 00222836.

176. V. S. Pande, I. Baker, J. Chapman, S. P. Elmer, S. Khaliq, S. M. Larson, Y. M. Rhee, M. R. Shirts, C. D. Snow, E. J. Sorin, et al., Biopolymers **68**, 91 (2003), ISSN 00063525.

177. J. A. Greathouse and M. D. Allendorf, Journal of the American Chemical Society **128**, 10678 (2006), ISSN 00027863.

178. J. Hu, X. Ruan, and Y. P. Chen, Nano Letters **9**, 2730 (2009), URL https://doi.org/10.1021/nl901231s.

179. H. Zhong and J. R. Lukes, Phys. Rev. B **74**, 125403 (2006), URL https://link.aps.org/doi/10.1103/PhysRevB.74.125403.

180. S. Izadi and A. V. Onufriev, Journal of Chemical Physics **145** (2016), ISSN 00219606, URL http://dx.doi.org/10.1063/1.4960175.

181. P. T. Kiss and A. Baranyai, Journal of Chemical Physics **138** (2013), ISSN 00219606.

182. P. T. Kiss and A. Baranyai, The Journal of Chemical Physics **141**, 114501 (2014), ISSN 0021-9606, URL http://aip.scitation.org/doi/10.1063/1.4895129.

183. A. Baranyai and P. T. Kiss, Journal of Chemical Physics **133** (2010), ISSN 00219606.

184. A. C. T. van Duin, S. Dasgupta, F. Lorant, and W. a. Goddard, The Journal of Physical Chemistry A **105**, 9396 (2001), ISSN 1089-5639, URL http://pubs.acs.org/doi/abs/10.1021/jp004368u.

185. H. Zhang, M. Li, and B. Yang, The Journal of Physical Chemistry C p. acs.jpcc.7b09315 (2018), ISSN 1932-7447, URL http://pubs.acs.org/doi/10.1021/acs.jpcc.7b09315.

186. M. Gaus, Q. Cui, and M. Elstner, Journal of Chemical Theory and Computation **7**, 931 (2011), ISSN 1549-9618, URL https://pubs.acs.org/doi/10.1021/ct100684s.

187. Q. Cui and M. Elstner, Physical Chemistry Chemical Physics **16**, 14368 (2014), ISSN 14639076.

188. M. Elstner, D. Porezag, G. Jungnickel, J. Elsner, M. Haugk, T. Frauenheim, S. Suhai, and G. Seifert, Phys. Rev. B **58**, 7260 (1998), URL https://link.aps.org/doi/10.1103/PhysRevB.58.7260.

189. Y. Yang, H. Yu, D. York, Q. Cui, and M. Elstner, Journal of Physical Chemistry A **111**, 10861 (2007), ISSN 10895639.

190. P. Goyal, H. J. Qian, S. Irle, X. Lu, D. Roston, T. Mori, M. Elstner, and Q. Cui, Journal of Physical Chemistry B **118**, 11007 (2014), ISSN 15205207.

191. R. Iftimie, P. Minary, and M. E. Tuckerman, Proceedings of the National Academy of Sciences **102**, 6654 (2005), ISSN 0027-8424, https://www.pnas.org/content/102/19/6654.full.pdf, URL https://www.pnas.org/content/102/19/6654.

192. T. D. Kühne, pp. 1–13 (2012), ISSN 17590876, 1201.5945, URL http://arxiv.org/abs/1201.5945{%}0Ahttp://dx.doi.org/10.1002/wcms.1176.

193. M. Dion, H. Rydberg, E. Schröder, D. C. Langreth, and B. I. Lundqvist, Phys. Rev. Lett. **92**, 246401 (2004), URL https://link.aps.org/doi/10.1103/PhysRevLett.92.246401.

194. J. Klimeš, D. R. Bowler, and A. Michaelides, Journal of Physics Condensed Matter **22** (2010), ISSN 09538984, 0910.0438.

195. C. Zhang, J. Wu, G. Galli, and F. Gygi, Journal of Chemical Theory and Computation **7**, 3054 (2011), ISSN 15499618.

196. Y. Shinohara, W. Dmowski, T. Iwashita, D. Ishikawa, A. Q. Baron, and T. Egami, Physical Review Materials **3**, 5 (2019), ISSN 24759953.

197. G. Camisasca, N. Galamba, K. T. Wikfeldt, and L. G. Pettersson, Journal of Chemical Physics **150** (2019), ISSN 00219606.

198. *MoSDeF web site*, URL http://www.mosdef.org.

199. *MoSDeF-Anaconda Cloud*, URL https://anaconda.org/mosdef/.

200. *BK3-water-model Github repository*, URL https://github.com/Marcello-Sega/BK3-water-model.

201. S. Nosé, The Journal of Chemical Physics **81**, 511 (1984), ISSN 00219606.

202. W. G. Hoover, Physical Review A **9**, 253 (1985), ISSN 01728083.

203. T. Kiss and M. Sega (2014).

204. T. P. Senftle, S. Hong, M. M. Islam, S. B. Kylasa, Y. Zheng, Y. K. Shin, C. Junkermeier, R. Engel-Herbert, M. J. Janik, H. M. Aktulga, et al., npj Computational Materials **2**, 15011 (2016), ISSN 2057-3960, URL http://www.nature.com/articles/npjcompumats201511.

205. W. Zhang, X. Chen, and A. C. Van Duin, Journal of Physical Chemistry Letters **9**, 5445 (2018), ISSN 19487185.

206. G. te Velde, F. M. Bickelhaupt, E. J. Baerends, C. Fonseca Guerra, S. J. van Gisbergen, J. G. Snijders, and T. Ziegler, Journal of Computational Chemistry **22**, 931 (2001), ISSN 01928651.

207. W. M. C. Foulkes and R. Haydock, Physical Review B **39**, 12520 (1989), ISSN 0163-1829, URL http://link.aps.org/doi/10.1103/PhysRevB.39.12520https://link.aps.org/doi/10.1103/PhysRevB.39.12520https://link.aps.org/doi/10.1103/RevModPhys.61.689.

208. M. Gaus, A. Goez, and M. Elstner, Journal of Chemical Theory and Computation **9**, 338 (2013), ISSN 1549-9618, URL https://pubs.acs.org/doi/10.1021/ct300849w.

209. A. Q. R. Baron, SPring-8 Information Newsletter **15**, 14 (2010).

210. Y. Shinohara, W. Dmowski, T. Iwashita, D. Ishikawa, A. Q. R. Baron, and T. Egami, Physical Review Materials **3**, 065604 (2019), ISSN 2475-9953, URL https://link.aps.org/doi/10.1103/PhysRevMaterials.3.065604.

211. I. S. Joung and T. E. Cheatham, Journal of Physical Chemistry B **112**, 9020 (2008), ISSN 15206106.

212. L. Van Hove, Physical Review **95**, 249 (1954), ISSN 0031899X.

213. *scattering Github repository*, URL https://github.com/mattwthompson/scattering.

214. B. Berne, Annual Review of Physical Chemistry **37**, 401 (1986), ISSN 0066426X.

215. K. E. Schmidt and D. M. Ceperley, in *The Monte Carlo Method in Condensed Matter Physics: Topics in Applied Physics, Vol 71*, edited by K. Binder (Springer-Verlag, 1992), pp. 205–248.

216. M. E. Tuckerman, in *Quantum Simulations of Complex Many-Body Systems: From Theory to Algorithms: NIC vol. 10*, edited by J. Grotendorst, D. Marx, and A. Muramatsu (John von Neumann Institute for Computing, 2002), pp. 269–298.

217. J. A. Morrone and R. Car, Physical Review Letters **101**, 1 (2008), ISSN 00319007, 0803.3635.

218. T. Egami, Frontiers in Physics **8**, 50 (2020), ISSN 2296-424X, URL https://www.frontiersin.org/article/10.3389/fphy.2020.00050.

219. H. W. Wang, M. Naguib, K. Page, D. J. Wesolowski, and Y. Gogotsi, Chemistry of Materials **28**, 349 (2016), ISSN 15205002.

220. S. Fleischmann, J. B. Mitchell, R. Wang, C. Zhan, D. E. Jiang, V. Presser, and V. Augustyn, Chemical Reviews **120**, 6738 (2020), ISSN 15206890.

221. S. Murali, N. Quarles, L. L. Zhang, J. R. Potts, Z. Tan, Y. Lu, Y. Zhu, and R. S. Ruoff, Nano Energy **2**, 764 (2013), ISSN 2211-2855, URL https://www.sciencedirect.com/science/article/pii/S2211285513000116.

222. X. Yang, C. Cheng, Y. Wang, L. Qiu, and D. Li, Science **341**, 534 (2013), ISSN 0036-8075, https://science.sciencemag.org/content/341/6145/534.full.pdf, URL https://science.sciencemag.org/content/341/6145/534.

223. M. Hu, Z. Li, T. Hu, S. Zhu, C. Zhang, and X. Wang, ACS Nano **10**, 11344 (2016), ISSN 1936086X.

224. Y. Gogotsi and B. Anasori, ACS Nano **13**, 8491 (2019), ISSN 1936086X.

225. J. Halim, J. Palisaitis, J. Lu, J. Thörnberg, E. J. Moon, M. Precner, P. Eklund, P. O. Persson, M. W. Barsoum, and J. Rosen, ACS Applied Nano Materials **1**, 2455 (2018), ISSN 25740970.

226. C. Zhan, M. Naguib, M. Lukatskaya, P. R. Kent, Y. Gogotsi, and D. E. Jiang, Journal of Physical Chemistry Letters **9**, 1223 (2018), ISSN 19487185.

227. Q. Gao, W. Sun, P. Ilani-Kashkouli, A. Tselev, P. R. C. Kent, N. Kabengi, M. Naguib, M. Alhabeb, W.-Y. Tsai, A. P. Baddorf, et al., Energy Environ. Sci. **13**, 2549 (2020), URL http://dx.doi.org/10.1039/D0EE01580F.

228. V. N. Borysiuk, V. N. Mochalin, and Y. Gogotsi, Nanotechnology **26**, 265705 (2015), ISSN 0957-4484, URL http://stacks.iop.org/0957-4484/26/i=26/a=265705?key=crossref.10f2f118df6bb55fbe1b81a49eb83815.

229. M. Ghidiu, S. Kota, J. Halim, A. W. Sherwood, N. Nedfors, J. Rosen, V. N. Mochalin, and M. W. Barsoum, Chemistry of Materials **29**, 1099 (2017), ISSN 15205002.

230. M. W. Thompson, *Molecular simulation of ionic liquids: Effects of solvation, humidification, and confinement* (2019-09-20).

231. Y. Dall'Agnese, P. Rozier, P. L. Taberna, Y. Gogotsi, and P. Simon, Journal of Power Sources **306**, 510 (2016), ISSN 03787753.

232. Z. Lin, P. Rozier, B. Duployer, P. L. Taberna, B. Anasori, Y. Gogotsi, and P. Simon, Electrochemistry Communications **72**, 50 (2016), ISSN 13882481.

233. Z. Lin, D. Barbara, P. L. Taberna, K. L. Van Aken, B. Anasori, Y. Gogotsi, and P. Simon, Journal of Power Sources **326**, 575 (2016), ISSN 03787753.

234. K. Liang, R. A. Matsumoto, O. N. C. Zhao, Wei, I. Popov, B. P. Thapaliya, S. Fleischmann, S. Misra, K. Prenger, M. Tyagi, E. Mamontov, et al. (2021), submitted.

235. S. Tsuzuki, W. Shinoda, H. Saito, M. Mikami, H. Tokuda, and M. Watanabe, The Journal of Physical Chemistry B **113**, 10641 (2009), ISSN 1520-6106, URL http://pubs.acs.org/doi/abs/10.1021/jp811128b.

236. *mxene_polymer_emim Github repository*, URL https://github.com/rmatsum836/mxene_polymer_emim.

237. R. Gowers, M. Linke, J. Barnoud, T. Reddy, M. Melo, S. Seyler, J. Domański, D. Dotson, S. Buchoux, I. Kenney, et al., Proceedings of the 15th Python in Science Conference pp. 98–105 (2016).

238. Z. Wang, Y. Yang, D. L. Olmsted, M. Asta, and B. B. Laird, Journal of Chemical Physics **184102** (2014), URL http://dx.doi.org/10.1063/1.4899176.

239. G. Feng, S. Li, J. S. Atchison, V. Presser, and P. T. Cummings (2013).

240. S. K. Reed, O. J. Lanning, and P. A. Madden, The Journal of Chemical Physics **126**, 084704 (2007), https://doi.org/10.1063/1.2464084, URL https://doi.org/10.1063/1.2464084.

241. M. Chen, J. Wu, T. Ye, J. Ye, C. Zhao, S. Bi, J. Yan, B. Mao, and G. Feng, Nature Communications **11**, 5809 (2020), URL https://doi.org/10.1038/s41467-020-19469-3.

242. C. Merlet, C. Péan, B. Rotenberg, P. A. Madden, P. Simon, and M. Salanne, Journal of Physical Chemistry Letters **4**, 264 (2013), ISSN 19487185.

243. *lammps-conp Github repository*, URL https://github.com/zhenxingwang/lammps-conp.

244. P. T. Cummings, C. McCabe, C. R. Iacovella, A. Ledeczi, E. Jankowski, A. Jayaraman, J. C. Palmer, E. J. Maginn, S. C. Glotzer, J. A. Anderson, et al., AIChE Journal (2021), ISSN 0001-1541.

245. R. S. DeFever, R. A. Matsumoto, A. W. Dowling, P. T. Cummings, and E. J. Maginn, Journal of Computational Chemistry (2021).

246. M. W. Thompson, J. B. Gilmer, R. A. Matsumoto, C. D. Quach, P. Shamaprasad, A. H. Yang, C. R. Iacovella, C. McCabe, and P. T. Cummings, Mol. Phys. p. e1742938 (2020).

247. J. K. Shah, E. Marin-Rimoldi, R. G. Mullen, B. P. Keene, S. Khan, A. S. Paluch, N. Rai, L. L. Romanielo, T. W. Rosch, B. Yoo, et al., Journal of Computational Chemistry pp. 1727–1739 (2017), ISSN 1096987X.

248. *Graphene-Pore Github repository*, URL https://github.com/rmatsum836/Pore-Builder.

249. P. Eastman, J. Swails, J. D. Chodera, R. T. McGibbon, Y. Zhao, K. A. Beauchamp, L.-P. Wang, A. C. Simmonett, M. P. Harrigan, C. D. Stern, et al., PLOS Computational Biology **13**, e1005659 (2017), ISSN 1553-7358, URL https://dx.plos.org/10.1371/journal.pcbi.1005659.

250. M. R. Shirts, C. Klein, J. M. Swails, J. Yin, M. K. Gilson, D. L. Mobley, D. A. Case, and E. D. Zhong, Journal of Computer-Aided Molecular Design **31**, 147 (2017), ISSN 15734951.

251. *ParmEd — ParmEd documentation* (2018), URL http://parmed.github.io/ParmEd/html/index.html.

252. S. Plimpton, *Fast parallel algorithms for short-range molecular dynamics* (1995), nag.2347.

253. J. K. Shah, E. Marin-Rimoldi, R. G. Mullen, B. P. Keene, S. Khan, A. S. Paluch, N. Rai, L. L. Romanielo, T. W. Rosch, B. Yoo, et al., Journal of Computational Chemistry pp. 1727–1739 (2017), ISSN 1096987X.

254. *MoSDeF-Cassandra Github repository*, URL https://github.com/MaginnGroup/mosdef_cassandra.

255. E. J. Maginn, J. K. Shah, E. Marinrimoldi, S. Khan, N. Rai, T. Rosch, and A. Paluch, Cassandra Manual (2014).

256. Y. Nejahi, M. Soroush Barhaghi, J. Mick, B. Jackman, K. Rushaidat, Y. Li, L. Schwiebert, and J. Potoff, SoftwareX **9**, 20 (2019), ISSN 23527110.

257. T. D. Kühne, M. Iannuzzi, M. Del Ben, V. V. Rybkin, P. Seewald, F. Stein, T. Laino, R. Z. Khaliullin, O. Schütt, F. Schiffmann, et al., The Journal of Chemical Physics **152**, 194103 (2020).

258. H. A. Lorentz, annalen der physik **248**, 127 (1981), ISSN 0021-4884.

259. D. Berthelot, in *COMPTES RENDUS DES SÉANCES DE L'ACADÉMIE DES SCIÉNCES* (1898), pp. 1703–1855.

260. W. Shinoda, M. Shiga, and M. Mikami, Physical Review B - Condensed Matter and Materials Physics **69**, 16 (2004), ISSN 01631829.

261. J. P. Ryckaert, G. Ciccotti, and H. J. Berendsen, Journal of Computational Physics **23**, 327 (1977), ISSN 10902716.

262. R. W. Hockney and J. W. Eastwood, *Computer simulation using particles* (Bristol: Hilger, 1988, 1988).

263. E. A. Müller, L. F. Rull, L. F. Vega, and K. E. Gubbins, The Journal of Physical Chemistry **100**, 1189 (1996).

264. A. Striolo, A. Chialvo, K. Gubbins, and P. Cummings, The Journal of chemical physics **122**, 234712 (2005).

265. *Daylight SMILES Documentation*, URL https://www.daylight.com/dayhtml/doc/theory/theory.smiles.html.

266. *GMSO Website*, URL https://gmso.mosdef.org.

267. *coMMMParE Github repository*, URL https://github.com/PTC-CMC/coMMParE.

Appendix A

Appendix to Chapter 3

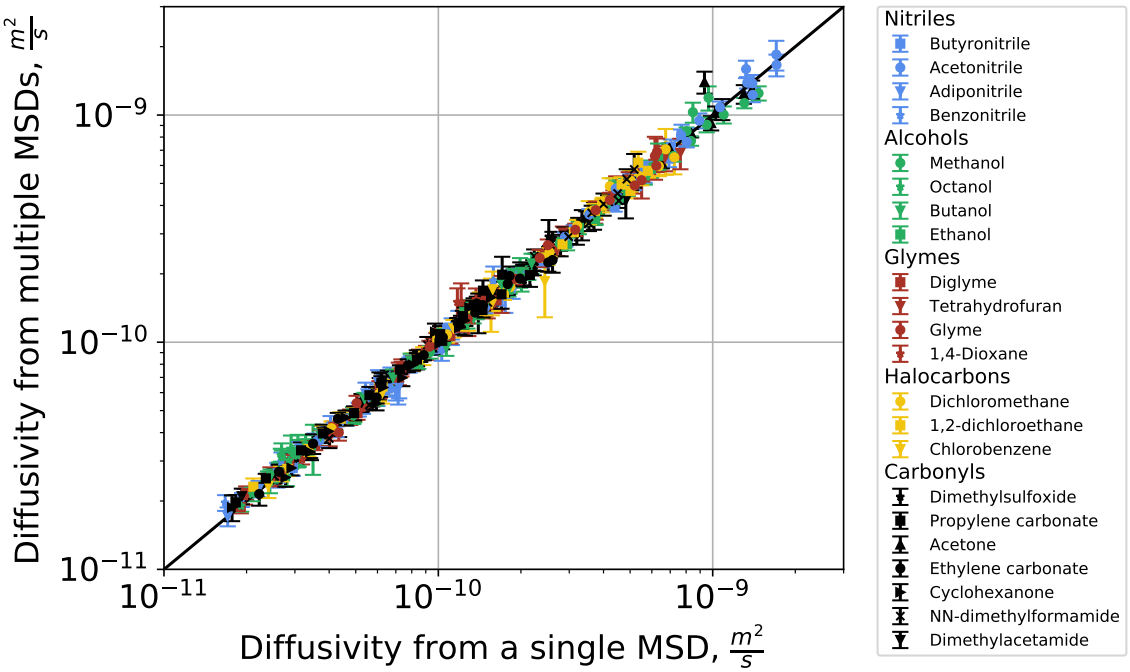

Figure A.1: Comparison of ion self-diffusivities obtained from a single MSD and values obtained from averaging over MSDs obtained from smaller sub-trajectories of the same trajectory. The diagonal line at $y = x$ is to guide the eye.

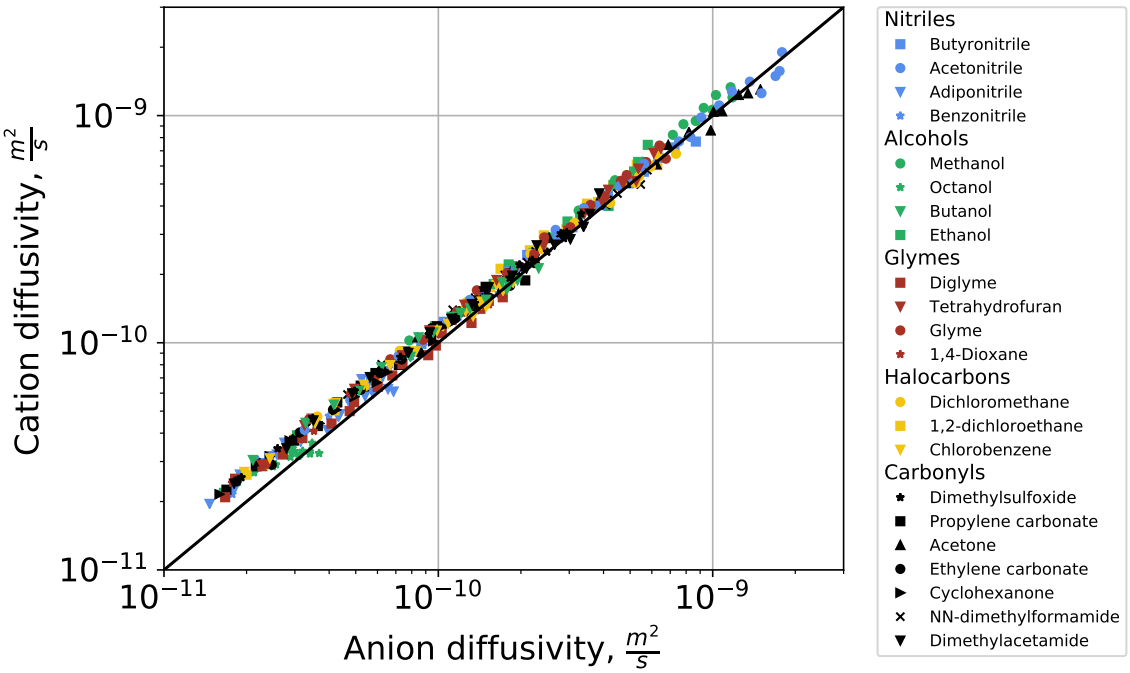

Figure A.2: Comparison of $BMIM^+$ and Tf_2N^- self-diffusivities in all mixtures of ionic liquids and organic solvents.

wtpct	14dio	ace	adpn	benzonitrile	bucn	butanol	ch3cn	ch3oh	clbenzene	cy6one	dce	thf
0.05	1027.7	810.9	951	960.8	777.9	820.3	758.1	787.3	1114.9	959.2	1236.3	874
0.1	1045.8	832.3	969.5	1006.2	799.4	840.8	780.1	807.7	1134.6	977.9	1249.8	895.3
0.15	1063.8	854.7	988.3	1017.6	821.6	862	802.5	829.2	1150.9	997.2	1262.1	916.9
0.2	1083	878.2	1008	1045.2	845	884.4	826.4	851.8	1166.4	1016.8	1274.8	939.5
0.25	1102.5	902.8	1028.5	1070.1	869.6	907.7	851.7	875.5	1186.9	1037.5	1287.3	963.3
0.3	1122.7	928.3	1049.8	1097.7	895.5	932.4	877.7	900.5	1197.1	1058.8	1299.7	987.6
0.35	1143.6	955.2	1072	1119.8	922.6	958.1	905.3	926.7	1216.2	1081.1	1312.5	1013
0.4	1165.2	983.5	1094.8	1141.3	951.5	985.1	934.8	954.5	1232.7	1104.1	1324.6	1038.7
0.45	1187.3	1013.1	1118.9	1163.4	981.9	1013.9	965.9	984	1250.1	1128.2	1336.8	1067.2
0.5	1209.9	1044.2	1143.9	1186.8	1014	1043.8	998.8	1015.2	1268.3	1152.9	1349.7	1096.4
0.55	1233.1	1077	1170.1	1211.5	1048	1075.6	1033.9	1048.1	1287.4	1179.1	1361.9	1126.5
0.6	1256.9	1111.6	1197.8	1236.6	1084.3	1109.7	1071.2	1083.4	1306.8	1205.8	1374.4	1157.6
0.65	1280.8	1148.2	1226.4	1262.9	1122.5	1145.2	1110.7	1120.9	1326.9	1234.5	1386.7	1190.9
0.7	1306	1186.8	1256.9	1290	1162.9	1182.9	1152.6	1160.9	1347.2	1264.1	1399	1225.3
0.75	1331.4	1228.1	1288.3	1318.1	1206.6	1223.6	1198	1203.3	1367.5	1294.7	1411.5	1261.3
0.8	1357.7	1270.9	1321.5	1347.3	1252.8	1266.5	1245.7	1249.5	1388.2	1327.3	1423.5	1299.5
0.85	1384.9	1316.8	1356.4	1377.1	1302.3	1312.7	1296.9	1298.8	1408.7	1361.1	1435.4	1339.7
0.9	1412.6	1366.3	1393	1408.1	1355.2	1362.1	1352	1351.6	1430.1	1396.2	1448	1381.6
0.95	1442.5	1417.7	1431.9	1439.7	1411.7	1414.5	1410.1	1409.2	1451.2	1433.6	1460.3	1426

wtpct	dcm	diglyme	dma	dmf	dmso	ec	etoh	gly	glyme	octanol	pc	
0.05	1237.5	964.9	937.1	928.7	1105.6	1317.3	809.1		882.5	845.8	1227.5	
0.1	1256.1	984.3	956	947.9	1120.2	1324.9	829.9	1260	903.7	865.1	1238.3	
0.15	1268.4	1004.8	975.6	967.6	1135.2	1332	851.3	1267.4	925.7	885.5	1249.4	
0.2	1284.2	1025.4	995.8	988.1	1150.5	1339.7	874	1277.5	948.5	906.5	1260.7	
0.25	1299.1	1046.6	1017	1009.3	1166.3	1347.4	897.6	1287.7	972	928.8	1272.1	
0.3	1313.9	1068.9	1038.9	1031.7	1182.9	1354.9	922.5	1296.4	996.4	952.4	1283.8	
0.35	1327.1	1091.3	1061.8	1054.9	1199.5	1362.6	948.4	1306.9	1021.6	976.9	1295.5	
0.4	1340.3	1114.7	1085.4	1078.9	1216.9	1370.4	975.9	1317.2	1047.9	1002.9	1307.5	
0.45	1354.3	1139	1110	1104	1234.6	1378.6	1004.6	1328.4	1075.2	1030	1320.1	
0.5	1367.9	1164	1135.8	1130.1	1253	1386.4	1035.2	1339	1103.6	1058.9	1332.4	
0.55	1380.4	1189.8	1162.6	1157.3	1271.8	1394.4	1067.3	1350	1133.3	1089.6	1345.3	
0.6	1392.4	1216.7	1190.7	1186	1291.4	1402.7	1101.3	1361.9	1164.4	1122	1358.5	
0.65	1404.5	1244	1220.4	1216.1	1311.6	1411.2	1137.2	1374	1196.5	1156.3	1371.8	
0.7	1415.8	1273	1251	1247.5	1332.3	1419.8	1175.8	1386.5	1230.1	1193.1	1385	
0.75	1426.4	1303.2	1283.3	1280.4	1353.9	1428.5	1216.9	1399.7	1265.9	1231.6	1399	
0.8	1436.8	1334.1	1317.3	1315	1376.3	1436.8	1260.6	1412.5	1302.6	1273.7	1413.2	
0.85	1446.2	1366.6	1353.4	1351.3	1399.2	1446	1307.7	1426.1	1342.3	1318.2	1427.4	
0.9	1455.5	1400.4	1391	1389.7	1422.9	1454.6	1358.2	1440.9	1383.5	1365.4	1442.3	
0.95	1464.1	1435.6	1430.9	1430.4	1447.6	1463.5	1412.4	1455.9	1426.5	1417	1457.8	

Table A.1: Liquid densities ($kg\,m^{-3}$) for all mixtures over the range of concentrations in units of mass fraction.

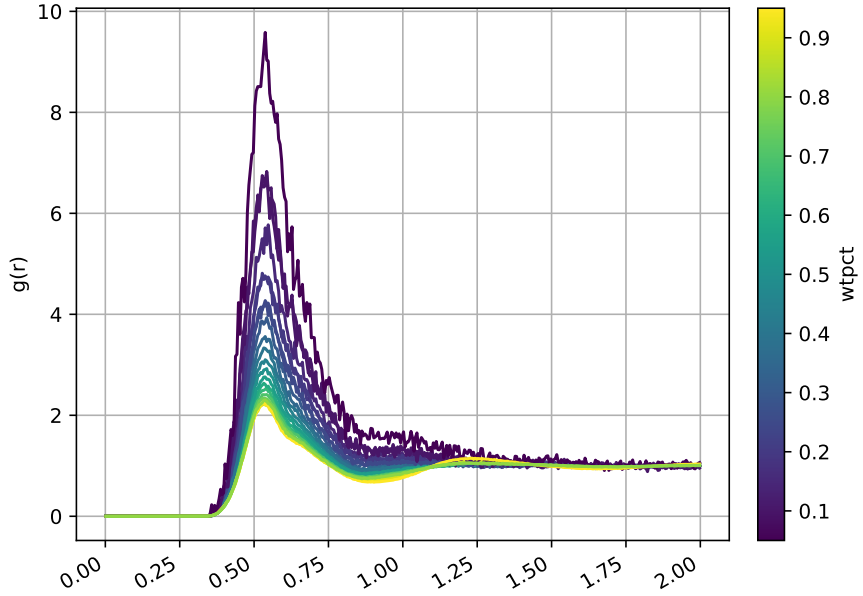

Figure A.3: Radial distribution function between $BMIM^+$ and Tf_2N^- in octanol at various concentrations.

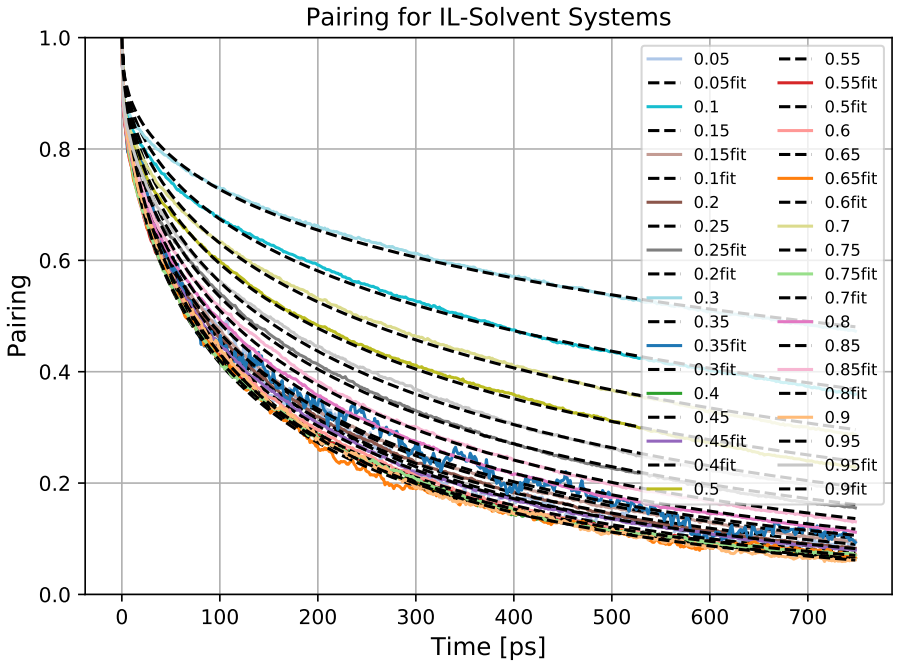

Figure A.4: Ratio of paired ions fitted with a stretched exponential function for all CH_3OH mixtures

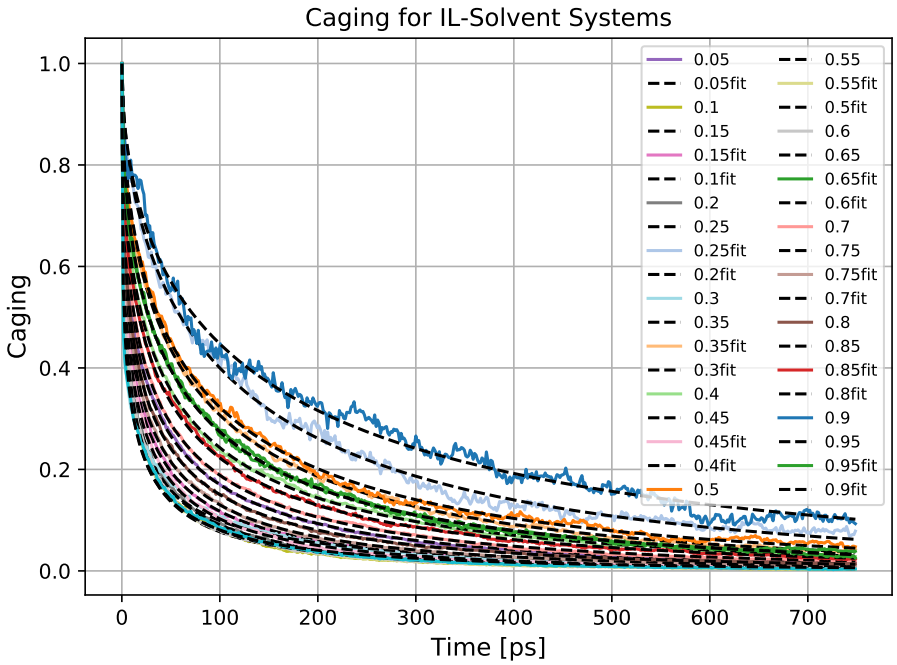

Figure A.5: Ratio of caged ions fitted with a stretched exponential function

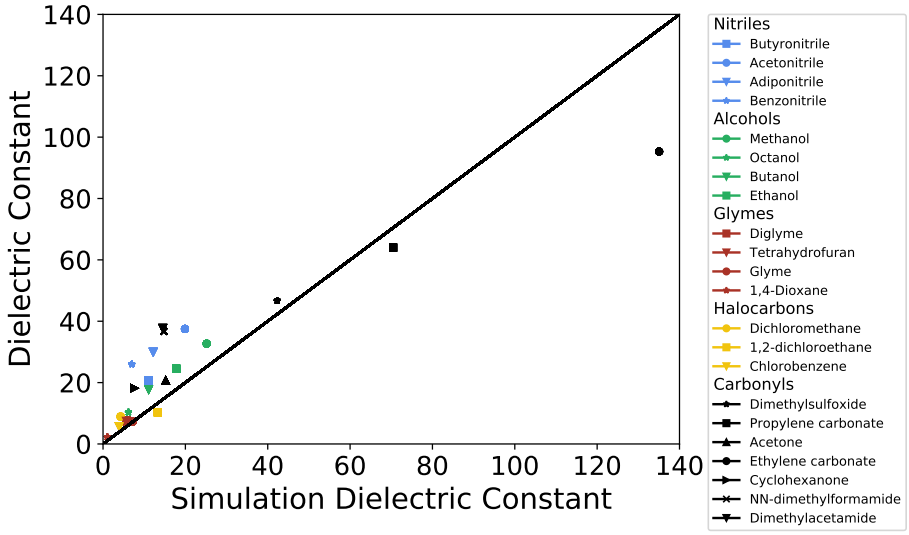

Figure A.6: Comparison of dielectric constants computed by simulation and from experimental values. Black line with slope of 1 displayed for comparison purposes.

Appendix B

Appendix to Chapter 4

Model	A_1	τ_1	γ_1	A_2	τ_2	γ_2
IXS	0.338	0.153	2.097	0.120	0.500	1.452
SPC/E (CMD)	0.337	0.129	1.866	0.144	0.345	1.384
TIP3P_EW (CMD)	0.292	0.127	1.971	0.172	0.257	1.545
BK3 (Polarizable CMD)	0.369	0.132	1.984	0.122	0.327	1.423
CHON-2017_weak (ReaxFF)	0.335	0.136	1.987	0.143	0.309	1.499
3obw (DFTB)	0.436	0.153	1.646	0.067	0.415	1.399
optB88 (AIMD)	0.424	0.124	1.935	0.063	4.158	1.169
optB88 at 330 K (AIMD)	0.379	0.122	2.020	0.063	0.445	1.320

Table B.1: Fitting results of the first peak area for the first-step decay, $A(t)$, of the Van Hove function. Fits calculated up to 0.7 ps for all methods

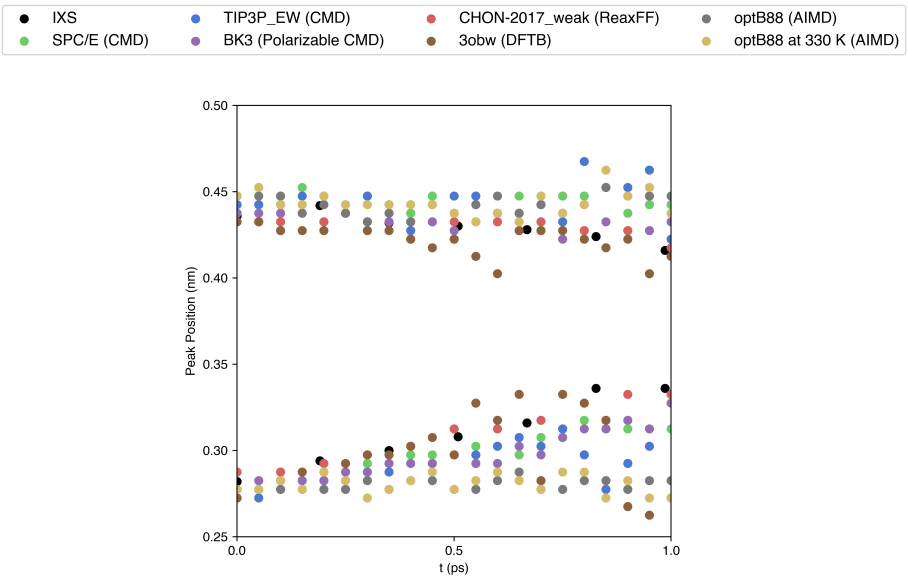

Figure B.1: Position, r (nm) of $g_1(t)$ and $g_2(t)$ for IXS and simulation data.

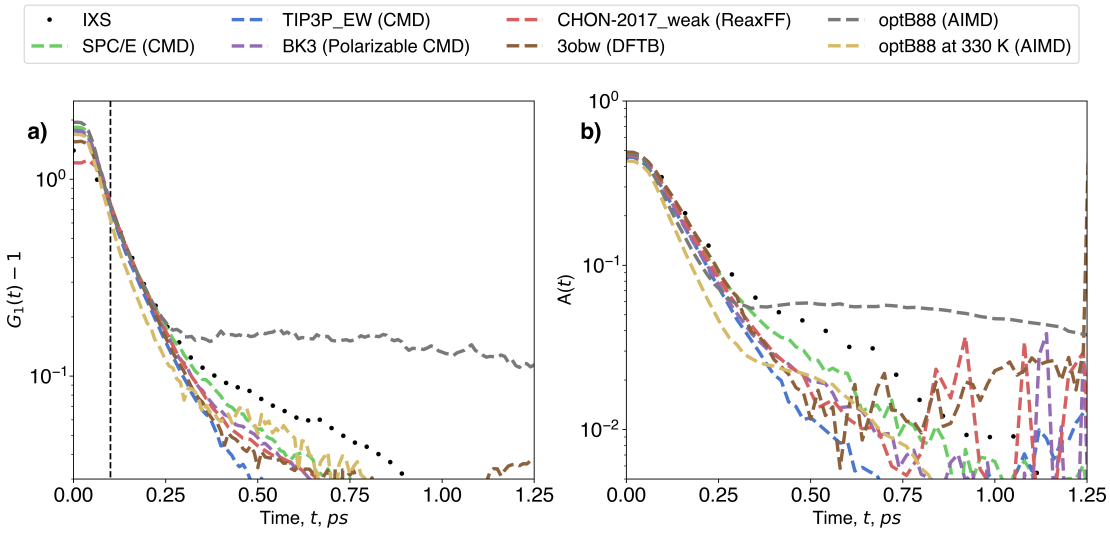

Figure B.2: a) Height of first peak, $g_1(t)$ and b) $A(t)$ as a function of time calculated from x-ray scattering and simulation methods. Time, t, is shown up to 1.25 ps.

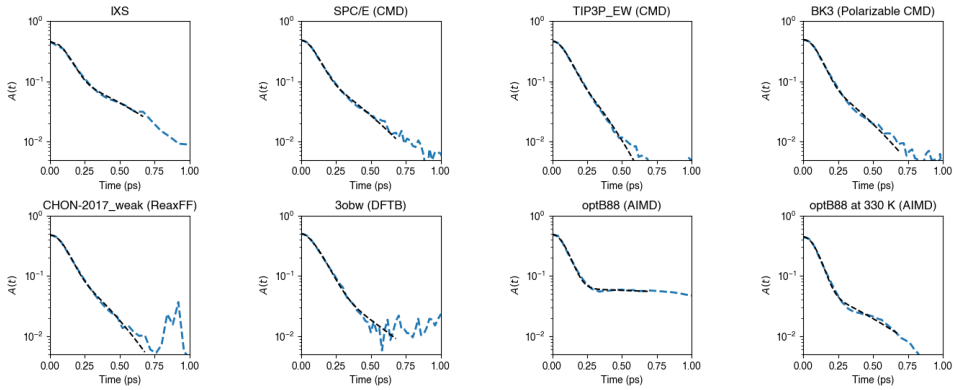

Figure B.3: $A(t)$ and fit to compressed exponential function for IXS and simulation data. Fits calculated up to 0.7 ps for all methods.

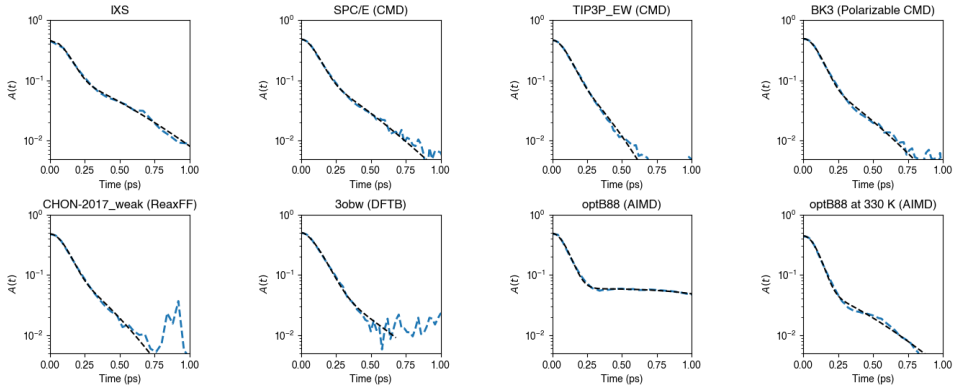

Figure B.4: $A(t)$ and fit to compressed exponential function for IXS and simulation data.

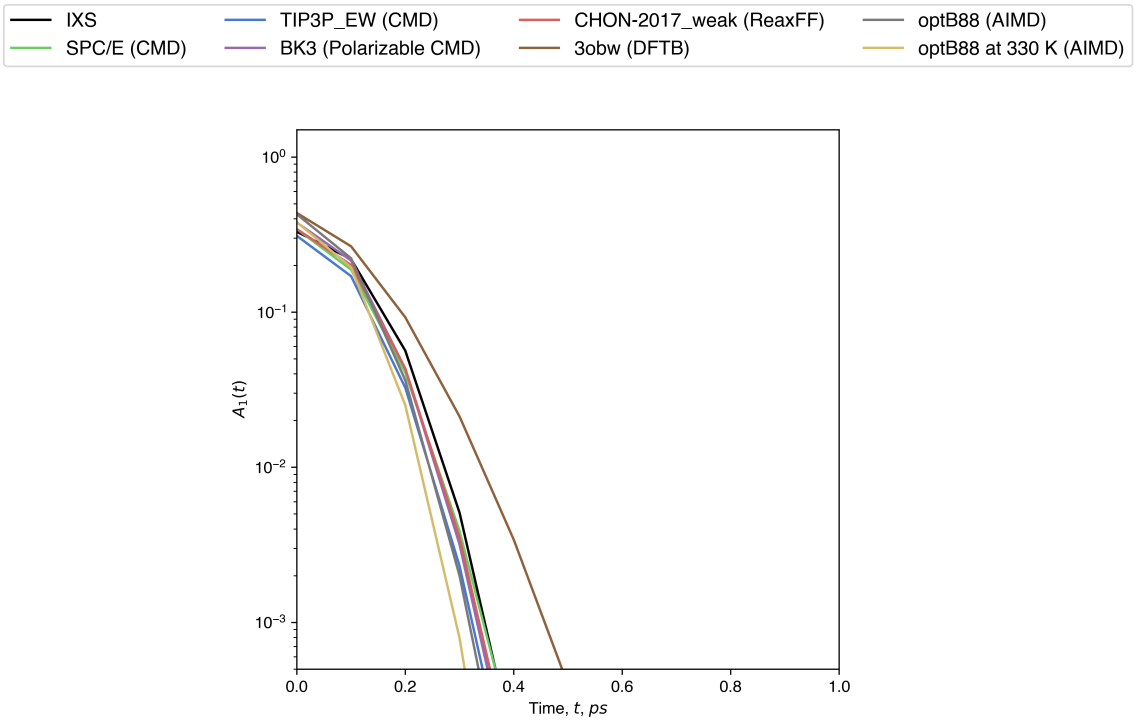

Figure B.5: Fitting results of first-step of $A_1(t)$ calculated from x-ray scattering and simulation methods.

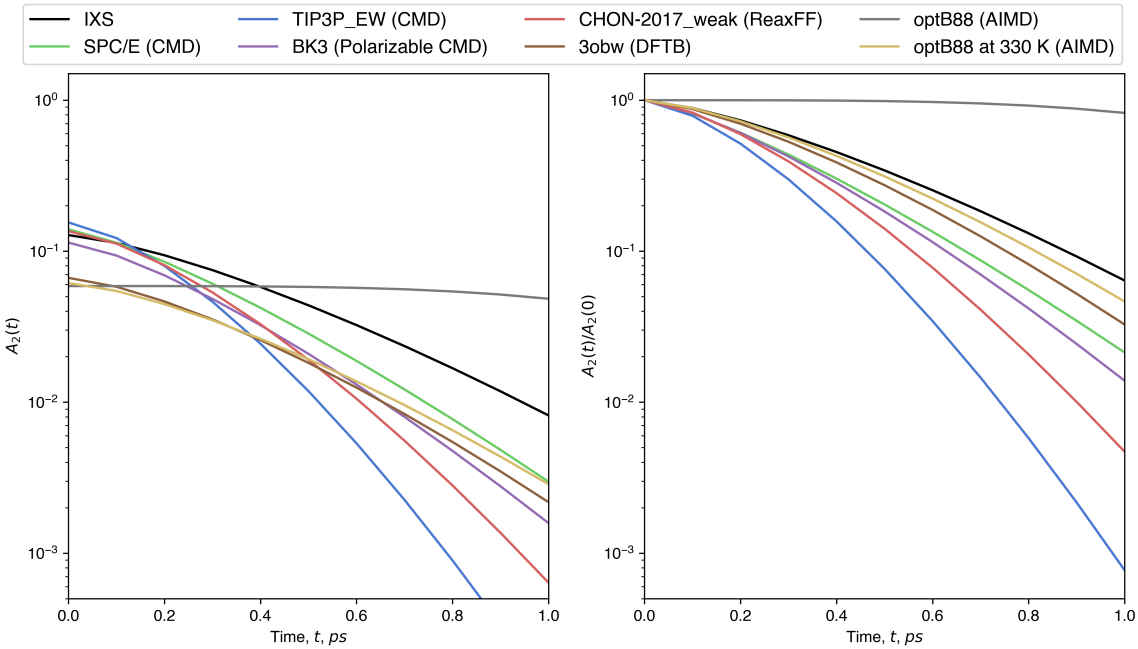

Figure B.6: Fitting results of second-step of a) $A_1(t)$ and b) $A_1(t)/A_1(0)$ calculated from x-ray scattering and simulation methods.

Appendix C

Appendix to Chapter 5

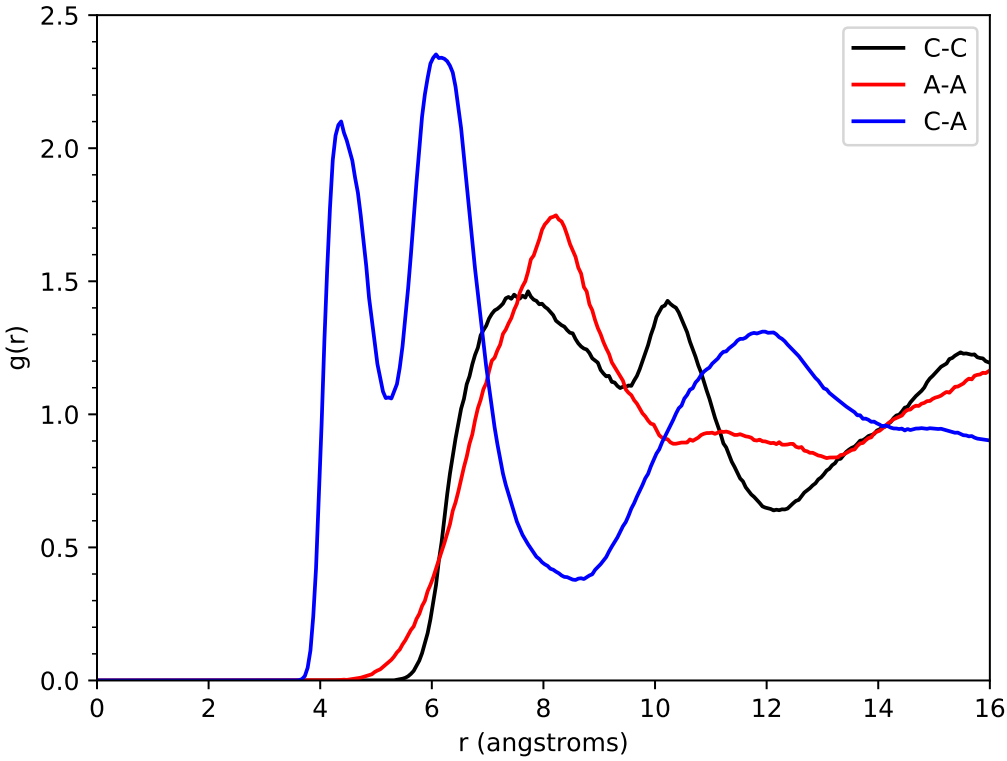

Figure C.1: COM RDF of butyltrimethylammonium (C4) AA and Tf_2N^- ions. Used to validate implementation of ionic liquid force field of Tsuzuki *et al.*[235].

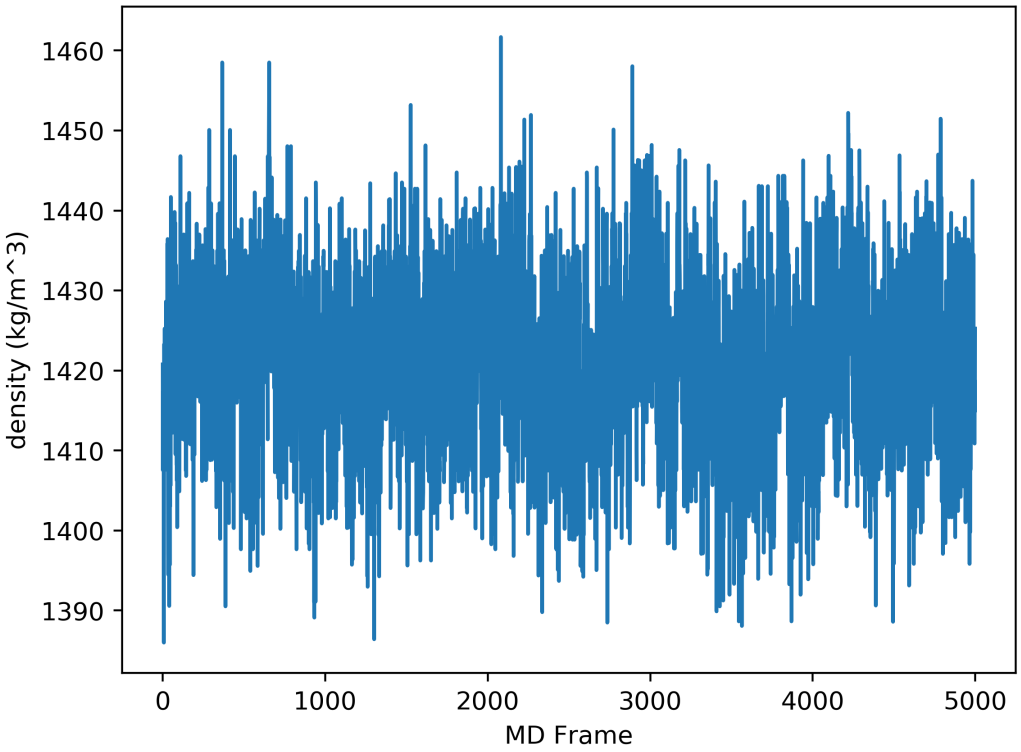

Figure C.2: Bulk density of ions in C12-MXene system.

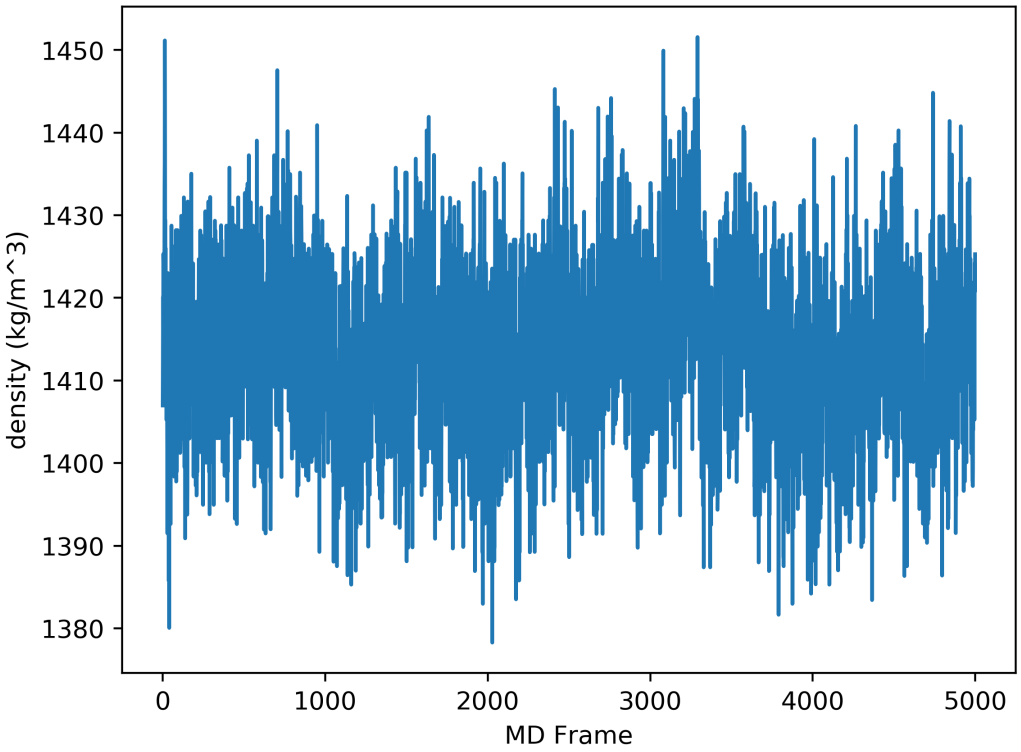

Figure C.3: Bulk density of ions in C16-MXene system.

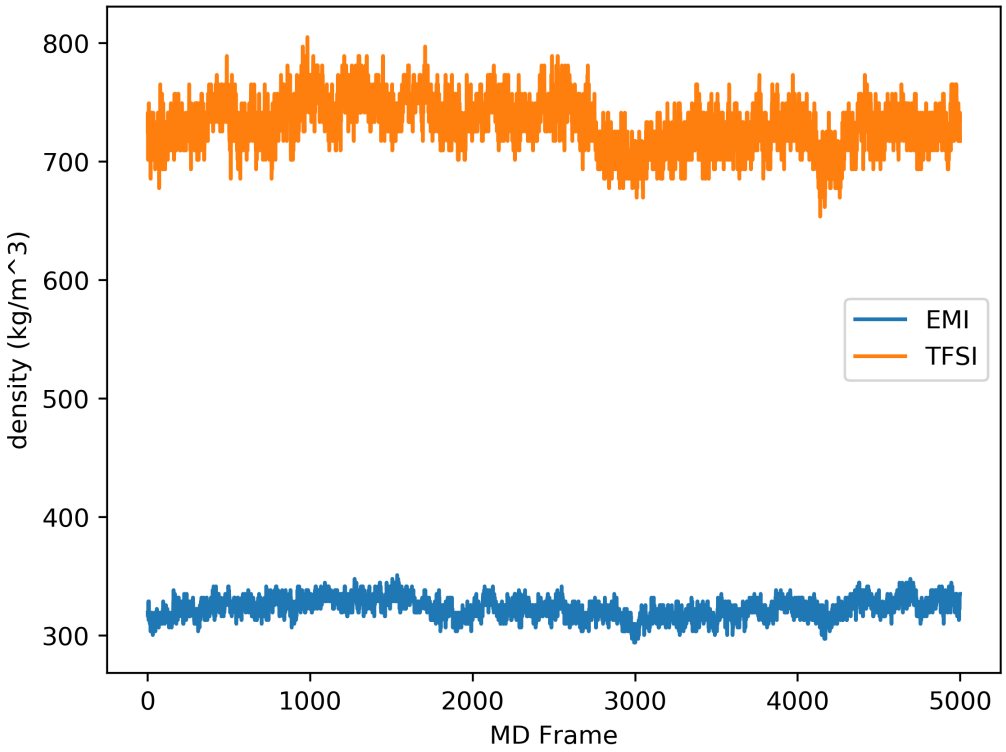

Figure C.4: Pore densities of ions in C12-MXene system.

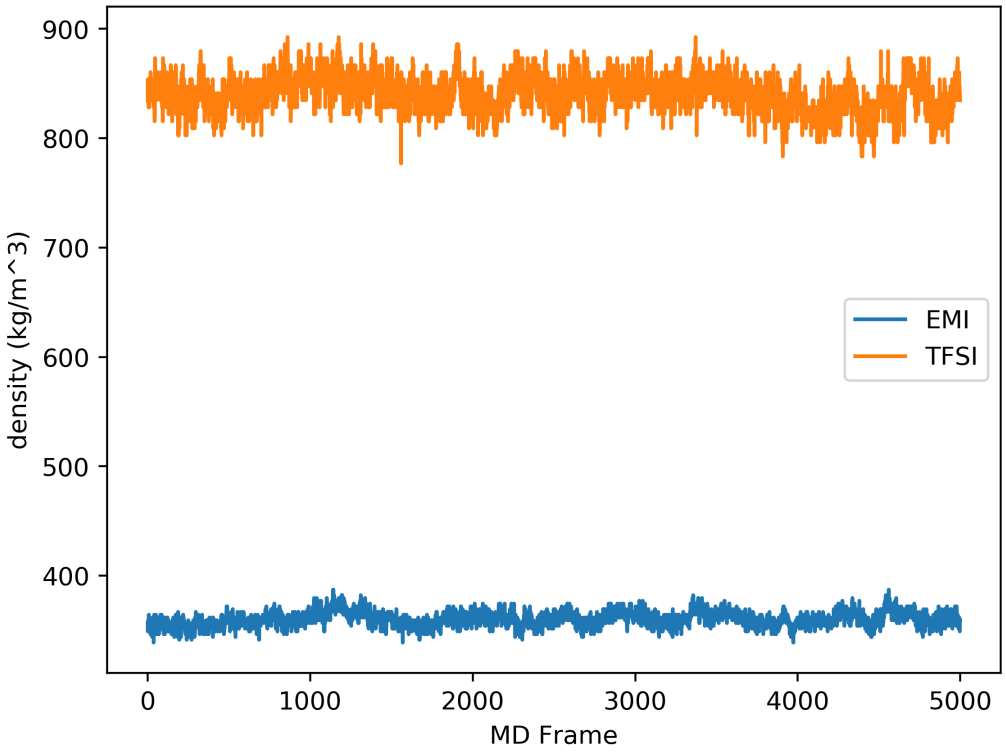

Figure C.5: Pore densities of ions in C16-MXene system.